DISTURBED STATE CONCEPT BASED CONSTITUTIVE MODELING FOR RELIABILITY ANALYSIS OF LEAD FREE SOLDERS IN ELECTRONIC PACKAGING AND FOR PREDICTION OF GLACIAL MOTION

by

SHANTANU MADHAVRAO SANE

_____

A Dissertation Submitted to the Faculty of the

DEPARTMENT OF CIVIL ENGINEERING AND ENGINEERING MECHANICS

In Partial Fulfillment of the Requirements

For the Degree of

DOCTOR OF PHILOSOPHY

WITH A MAJOR IN ENGINEERING MECHANICS

In the Graduate College

THE UNIVERSITY OF ARIZONA

2007

THE UNIVERSITY OF ARIZONA
GRADUATE COLLEGE

As members of the Dissertation Committee, we certify that we have read the dissertation prepared by Shantanu Madhavrao Sane

entitled Disturbed State Concept Based Constitutive Modeling For Reliability Analysis Of Lead Free Solders In Electronic Packaging And For Prediction Of Glacial Motion

and recommend that it be accepted as fulfilling the dissertation requirement for the Degree of Doctor of Philosophy

_____ Date: 11/05/07
Chandrakant Desai

_____ Date: 11/05/07
Dinshaw Contractor

_____ Date: 11/05/07
Achintya Haldar

_____ Date: 11/05/07
Olgierd Palusinski

Final approval and acceptance of this dissertation is contingent upon the candidate's submission of the final copies of the dissertation to the Graduate College.

I hereby certify that I have read this dissertation prepared under my direction and recommend that it be accepted as fulfilling the dissertation requirement.

_____ Date: 11/05/07
Dissertation Director: Chandrakant Desai

STATEMENT BY AUTHOR

This dissertation has been submitted in partial fulfillment of requirements for an advanced degree at the University of Arizona and is deposited in the University Library to be made available to borrowers under rules of the Library.

Brief quotations from this dissertation are allowable without special permission, provided that accurate acknowledgment of source is made. Requests for permission for extended quotation from or reproduction of this manuscript in whole or in part may be granted by the head of the major department or the Dean of the Graduate College when in his or her judgment the proposed use of the material is in the interests of scholarship. In all other instances, however, permission must be obtained from the author.

SIGNED: _____

Shantanu Madhavrao Sane

ACKNOWLEDGEMENTS

I would like to thank Dr. Chandrakant S. Desai for the opportunity, assistance and advice during this research. Over the years I have learnt much more than just academics from him and thank him for being a mentor.

I would also like to thank my committee members, Dr. Achintya Haldar, Dr. Dinshaw Contractor and Dr. Olgierd Palusinski. A special thanks to Dr. Haldar for his continuous encouragement. I would also like to thank Dr. Tribikram Kundu for his support. His modesty, sincerity and diligence have deeply influenced me.

The administrative staff at the CEEM department has been extremely supportive during my Ph.D program. A special thanks to Karen, for being my most reliable supply of candies and Therese, for her help in financial and immigration issues.

I have benefited greatly from Late. Dr. Russell Whitenack who always provided the right motivation and direction to this research.

Parts of this research are performed under research grant No. EAR – 0229889 from National Science Fundation (Washington, DC). Analysis of BGA electronic package has been performed in technical collaboration (Grant No. 175908) with Boeing Phantom Works, Seatte, WA. I am grateful to Dr. M. Rassaian and Dr. Simon Lee for their support in this project.

I am blessed with the most wonderful friends I met at the University. I would like to thank, Rahul, Manish, Sidd, Megha, Kedar, Anu, Parijat, Piya , Vinay, Pooja, Phoolendra, Shuchita, Aarthi, Sanket and Diljith for their kind words and encouragement. I couldn't have done it without them.

My wife, Amruta has brought me a lot of good fortune. She has been supportive, loving and most importantly patient during my Ph.D. research. I would like to thank her for being who she is and keeping me sane.

I am grateful to my parents, Mr. Madhav Sane and Mrs. Madhuri Sane for being extremely supportive and patient. My sister Mrunal and niece Rujuta have been my inspiration during this work. I am grateful to god for blessing me with a wonderful family.

Dedicated to
my parents
Mr. Madhav Sane and
Mrs. Madhuri Sane.

TABLE OF CONTENTS

TABLE OF CONTENTS - Continued

TABLE OF CONTENTS - Continued

LIST OF ILLUSTRATIONS

LIST OF ILLUSTRATIONS - Continued

LIST OF ILLUSTRATIONS - Continued

LIST OF ILLUSTRATIONS - Continued

LIST OF ILLUSTRATIONS - Continued

LIST OF ILLUSTRATIONS - Continued

LIST OF TABLES

LIST OF TABLES - Continued

ABSTRACT

The disturbed state concept (DSC) based constitutive model is the focus of this research. It is applied for characterizing two problems; thermomechanical reliability analysis of electronic packages, and prediction of glacial motion. A new procedure for construction of static yield surface for materials is proposed. Further, a modified DSC model to include effect of rate of loading on material behavior is proposed.

The DSC is applied to characterize the behavior of Sn-3.9Ag-0.6Cu (SAC) lead free solder alloy used in electronic packages. Proposed procedure of construction of static curve and rate dependent DSC model is applied for prediction of creep and rate dependent behavior of the SAC alloy. Laboratory test data is adopted from the literature and material parameters are determined. The DSC model is validated using the derived material parameters. A finite element analysis of the BGA 225 package is performed under cyclic thermomechanical loading. Analysis results are compared with available test data. A failure criterion for prediction of number of cycles to failure for BGA 225 is then derived.

The second application of DSC discussed in this work is prediction of glacial motion. Mechanical behavior of glacial till and its contribution to overall ice movement is characterized using DSC. Two regionally significant tills are chosen and samples are collected from field. A series of laboratory tests are conducted on samples. Tests results are used for model calibration and validation. A numerical simulation of an idealized ice – till system under gravity loading is performed. Two such analyses are performed with DSC and Mohr Coulomb models and the results are compared.

The DSC predicts failure when a significant portion of the material reaches a critical disturbance whereas the Mohr Coulomb model predicts failure based on peak stress. DSC predicts a gradual progression to failure whereas the Mohr Coulomb model predicts early catastrophic failure. According to DSC, the material undergoes considerable plastic strains before it reaches failure whereas the Mohr Coulomb predicts failure at very low elastic strains. In general the DSC is considered to provide a more realistic and general constitutive model for glacial tills.

CHAPTER 1

INTRODUCTION

1.1 Background

To simulate the behavior of a complex physical system it is often required to model the material response of key components using advanced material models. Such models when implemented in numerical tools can play a vital role in accurate simulations leading to design. The disturbed state concept (DSC) is a material modeling approach which is developed by Desai (2001) and is the focus of this dissertation. DSC is implemented in a numerical procedure based on the finite element method and has been successfully applied to a wide range of engineering problems.

In this work the DSC has been applied to two engineering problems,

1. Constitutive modeling of lead free solders in electronic packaging for reliability analysis under cyclic thermomechanical loading, and
2. Constitutive modeling of glacial till(s) in order to predict the motion of ice sheets and glaciers.

The following sections briefly describe both these problems and identify the research objectives for each of them.

1.2 Problem Statement

1.2.1 Electronic Packaging problem

Solder balls inside an electronic package perform three main functions, to carry the electric current, provide structural support to the chip and carry away the heat produced by chip (microprocessor). The chip, solder and substrate assembly undergoes

temperature variations during fabrication and operation. Thermal mismatch at the joint and resulting thermal stresses produce cracks resulting in joint failure. The behavior of solder material plays an important role in deciding the life of the package.

Lead based alloys such as Sn-Pb have been widely used as solder joint materials for many years. However, due to toxic properties of lead, the electronic industry is switching to lead free solders. In the present work a lead free solder alloy composed of Tin (Sn), Silver (Ag) and Copper (Cu) in the proportion Sn-3.9Ag-0.6Cu is considered as an alternative for the Sn-Pb alloy. The disturbed state concept based constitutive model is used to characterize the response of this alloy under cyclic thermomechanical loading. Primary research objectives for this problem are identified in the following section.

1.2.1.1 Research objectives

1. Conduct literature review for available test data on the Sn-3.9Ag-0.6Cu alloy.
2. Determine material parameters to calibrate the DSC/HISS and creep models.
3. Carry out validations of the DSC/HISS and creep models based on the laboratory test data.
4. Perform a thermomechanical fatigue analysis for an electronic package using finite element procedure and the material parameters derived for lead free alloy.
5. Propose modification in the current DSC/HISS model to include the effect of strain rate on material behavior.
6. Develop a procedure to test and validate the modified model.
7. Perform validations of the proposed rate dependent model.

1.2.2 Simulation of motion of ice sheets and glaciers.

Study of motion of ice sheets and glaciers is vital to understanding of its effect on the global sea levels and climate changes. Generally the total ice motion is considered to be made up of three components; (A) ice melting, (B) sliding at the interface of ice and the underlying sediment (till) and (C) sediment deformation. In this research the mechanical behavior of the till is investigated to find the contribution of sediment deformation towards the total ice motion. For this problem following research objectives are identified.

1.2.2.1 Research objectives

1. Collect glacial till samples from the field and conduct laboratory tests (stress-strain and creep tests) on the remolded samples.
2. Calibrate the DSC/HISS model based on the laboratory tests.
3. Validate the DSC/HISS model based on tests used for calibration and also based on tests not used for calibration.
4. Numerically simulate the glacial motion problem for two cases, (A) Using the DSC/HISS model and (B) Using the Mohr – Coulomb model.
5. Compare the results from both analyses.
6. Formulate a failure and motion criterion based on the results of the analyses.

1.3 Organization of dissertation

A brief review of constitutive modeling is given in chapter 2. This chapter introduces the disturbed state concept (DSC) based constitutive modeling approach. Brief discussion on other elasticity and plasticity models is also provided.

Creep modeling approach using DSC is described in chapter 3. This chapter also discusses the proposed modification in the current HISS model to include the effect of strain rate on material behavior.

In chapter 4 various material parameters in HISS, DSC and creep models are identified and procedure for their determination using laboratory test data is presented.

Chapter 5 concentrates on the application of DSC model for the electronic packaging problem. It discusses the available test data for lead free solder alloys followed by DSC model calibration and validation. This chapter also presents the results of thermomechanical analysis of '313 pin BGA' package which is performed using the finite element method. Application of proposed rate dependent DSC model discussed in chapter 3 and its validation is then presented for lead free solder alloys.

Chapter 6 presents application of DSC model for modeling two glacial tills. Detailed test plan for various laboratory tests conducted on the tills is presented followed by the test results. DSC/HISS model calibration and validation at specimen level is then presented. Results from simulation of the idealized glacial motion problem using DSC and Mohr – Coulomb models are discussed.

Finally chapter 7 discusses significant contributions from this research followed by conclusion.

CHAPTER 2

REVIEW OF CONSTITUTIVE MODELING

2.1 Constitutive models

A constitutive model defines the response of a material under applied loading. Loading conditions may include mechanical loads such as point loads, distributed loads, applied displacements and so on. Thermal and environmental loads and other effects causing change in current material state may also be considered as applied loading. Under the application of such loads the material undergoes number of microstructural changes and transformations. These transformations are manifested by various effects such as elastic strains, plastic strains, creep, degradation or softening and fracture or failure. In this chapter various constitutive models are discussed that include one or more of these effects.

2.2 Elastic models

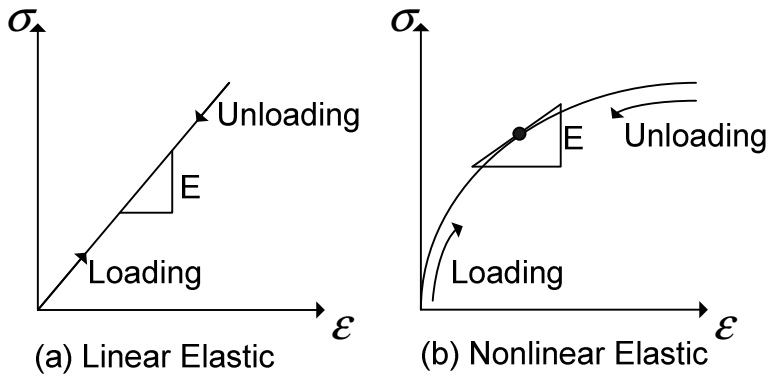

Figure 2.1 Elastic models

2.2.1 Linear elastic model.

In this model the material is assumed to behave in a fully elastic manner. Thus all the deformation under an applied load is assumed to be reversible. The relation between applied stress and strain is given by Hooke's law. For one dimensional case the Hooke's law is given as

$$\sigma = E.\varepsilon \tag{2.1a}$$

$$\nu = \frac{\varepsilon_{lateal}}{\varepsilon_{longitudinal}} \tag{2.1b}$$

where E is the Young's modulus as shown in Figure 2.1 (a), ν is Poisson's ratio which is the ratio of lateral and longitudinal strains. For 3D cases the generalized Hooke's law is written as

$$\sigma_{ij} = C^{e}_{ijkl}.\varepsilon_{ij} \tag{2.2}$$

where σ_{ij} is the stress tensor, C^{e}_{ijkl} is the elastic constitutive tensor and ε_{ij} is the strain tensor. For linear and isotropic materials, C^{e}_{ijkl} is made up of material elastic constants such as Young's modulus and Poisson's ratio. The linear elastic model is the simplest available constitutive model, however; it can not handle some of the important aspects of material behavior such as plastic and creep strains thus making it unsuitable for most materials. It is often used to define the elastic part in the elastoplastic constitutive models.

2.2.2 Nonlinear elastic model

The nonlinear elastic model also assumes that the material behaves in a fully elastic manner however the stress - strain behavior is nonlinear as shown in Figure 2.1 (b). Elastic modulus in this case is not a constant and it changes along the stress strain curve (Figure 2.1 (b)). Nonlinear elastic models are more realistic as compared to linear elastic models since the material response is almost always nonlinear. In this case, the nonlinear response is approximated as piecewise linear by dividing the nonlinear behavior in a number of linear increments. The incremental form of the generalized Hooke's law is then used to define the stress strain relation.

$$d\sigma_{ij} = (C^{e}_{ijkl})_{t}.d\varepsilon_{ij} \tag{2.3}$$

where $(C^{e}_{ijkl})_{t}$ is composed of the tangent modulii.

Elastic models are relatively simple but they may not be applicable to many natural materials such as geologic and metal alloys. Plasticity models can then be used to handle the plastic nonlinear behavior. Following section describes some of the typical plasticity models.

2.3 Plasticity models.

Under an applied load the material undergoes both reversible and irreversible strains. Irreversible strains are called as plastic. Most materials exhibit elastic response until certain load is reached. If loaded beyond the yield load, materials start yielding or undergoing plastic deformations. The limiting load is called as the yield point of the material Figure 2.2.

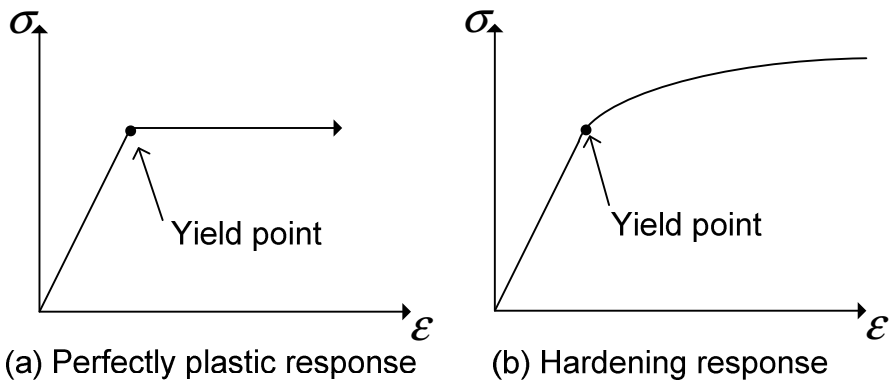

Figure 2.2 Types of material plastic response.

Some models assume that materials behave in a perfectly plastic manner (Figure 2.2 (a)) in which they can carry no further load after the yield. The conditions of stress at which yield occurs are called yield criterion. Typical examples of yield criteria are Von Mises, Tresca, Mohr Coulomb and Drucker Prager. Some of these are described in section 2.3.1.

Unlike perfectly plastic behavior, some models assume that the material hardens (Figure 2.2 (b)) or gains strength when loaded beyond the yield point (elastic limit). Such models are termed as hardening models. More advanced models based on the hardening assume that every point on the stress strain curve to be a yield point. Such models are called as continuous yielding models. Some examples of such models are critical state and hierarchical single surface (HISS) plasticity. These are described in section 2.3.2.

2.3.1 Yield criteria.

A yield criterion is a rule that defines the elastic limit of the material. Usually yield criteria are expressed in terms of stress invariants. A mathematical expression defining the yield criterion is known as yield function and is usually denoted by F.

2.3.1.1 Von Mises yield criterion.

Von Mises yield criterion assumes that the material enters into plastic region when the shear strength exceeds a certain limit determined from experiments. This is expressed by yield function given by

$$F = J_{2D} - k^2 \tag{2.4}$$

where J_{2D} is the second invariant of deviatoric stress tensor which represents the shear strength of the material and , $k = \frac{\sigma_y}{3}$ is a material parameter determined from laboratory tests.

This criterion essentially assumes that the strength of the material is same in all directions. Thus it plots as a circle in $\sigma_1 - \sigma_2 - \sigma_3$ stress space as shown in Figure 2.3.

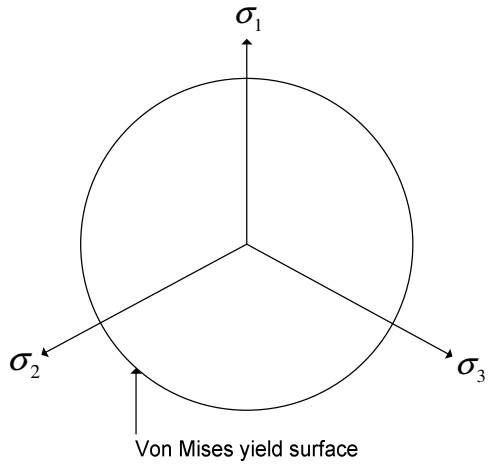

Figure 2.3. Von Mises yield surface in $\sigma_1 - \sigma_2 - \sigma_3$ space.

This yield criterion may be used in case of metals that exhibit predominantly isotropic response, however; it can not be used for anisotropic materials. Another limitation of this criterion is that the yielding behavior is assumed to be independent of confining stress on the material. This may not be valid for soft materials (such as soils) whose behavior is affected by confining stress. For geologic materials Mohr Coulomb criterion is widely used which overcomes some of the above limitations.

2.3.1.2 Mohr Coulomb Criterion.

Yield function in Mohr Coulomb criterion is given by (Desai, 2001) equation 2.5.

$$F = J_1 \sin(\phi) + \sqrt{J_{2D}} \cos(\theta) - \frac{\sqrt{J_{2D}}}{3} \sin(\phi) \sin(\theta) - c \cos(\phi) = 0 \tag{2.5}$$

where c is the cohesion, ϕ is the friction angle, and θ (the Lode angle) is in the range $-\frac{\pi}{6} \le \theta \le \frac{\pi}{6}$ and is computed as

$$\theta = \frac{1}{3} \arcsin\left(-\frac{3\sqrt{3}}{2} \frac{J_{3D}}{J_{2D}^{3/2}} \right) \tag{2.6}$$

It can be seen that the Mohr Coulomb criterion considers J_1 dependence of the material behavior. Thus it may be used to model geologic materials. Figure 2.4 shows the yield function for Mohr Coulomb model plotted in the $\sigma_1 - \sigma_2 - \sigma_3$ plane. It can be seen that the

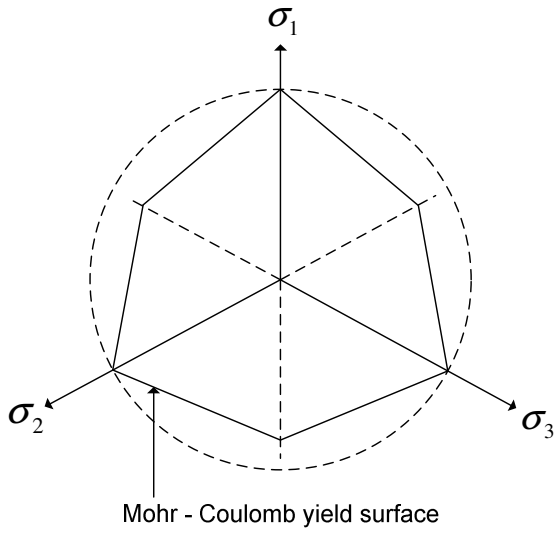

Figure 2.4. Mohr Coulomb yield surface in $\sigma_1 - \sigma_2 - \sigma_3$ stress space.

Mohr Coulomb yield surface plots as an irregular hexagon indicating that the material strength in compression and tension need not be the same. Thus this can be considered to be a more advanced criterion as compared to Von Mises.

2.3.2 Continuous yielding models.

Figure 2.5 shows a schematic of stress strain behavior of a material. Consider point A on the stress strain curve, it can be considered to be the initial yield point for the material. If the loading continues from point A to B and unloading occurs at point B then the elastic strain is recovered and material moves to point C. Further, if the material is reloaded then the reloading occurs without any additional plastic strains until point B is reached. After point B the plastic strains start accumulating once again. Thus B defines the beginning of yielding in this case and can thus be also called a yield point. Yield

strength at point A is σ_{y1} and that at B is σ_{y2}. It can be seen that $\sigma_{y2} > \sigma_{y1}$, thus indicating that the yield stress has increased or the material has undergone hardening.

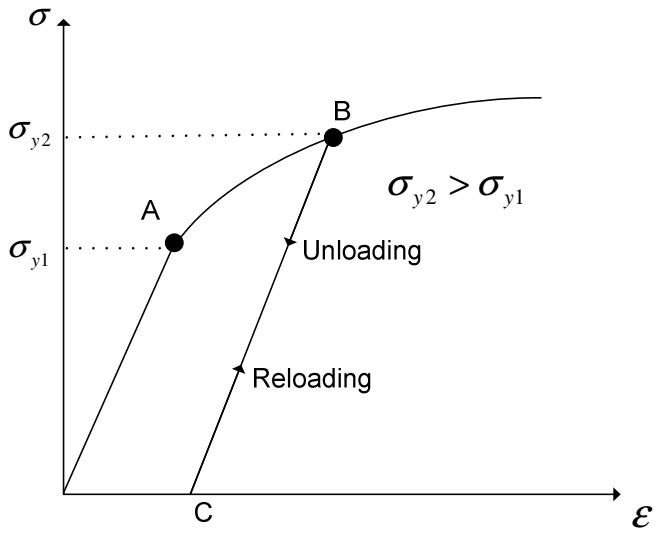

Figure 2.5. Hardening behavior

In cases when the initial yield point such as point A can not be clearly located it may be necessary to assume that every point on the stress strain curve is a yield point. This is called as continuous yielding approach in which yielding begins from the start of the loading and plastic strains accumulate. Every subsequent loading increment then moves the yield point to higher yield stress compared to the previous one thus indicating continuous yielding or hardening. Both elastic and plastic deformations are assumed to occur from the first load increment. Constitutive models based on this approach are called continuous yielding models. Two of such models are described here in sections 2.3.2.1 and 2.3.2.2.

2.3.2.1 Critical state model

Critical state is defined as a state of the material which may be reached after the material has been loaded to such an extent that it can be considered to be very close to failure. This is illustrated with an example of a geologic material in Figure 2.6. It shows schematics of stress – strain responses of initially loose and dense geologic materials such as sand. Initially loose material compresses when loaded and eventually reaches a state where it can be considered to be shearing under a constant volume. On the other hand, when initially dense material is loaded in compression it compresses initially and then undergoes microstructural changes resulting in loss of strength or degradation. It eventually approaches the same critical state as that of the loose material.

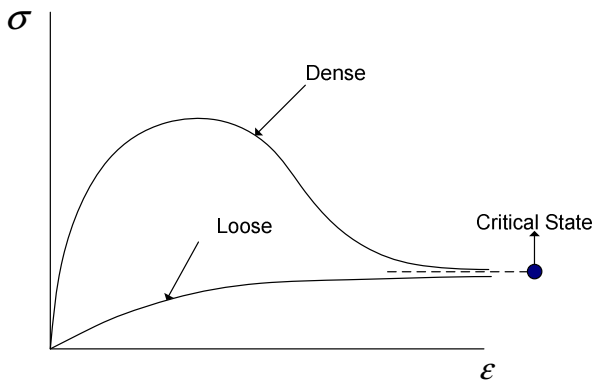

Figure 2.6 Critical state for initially loose and dense geologic materials.

Thus irrespective of the initial density of the material the material approaches the same ultimate state given that the initial mean pressure for both cases is the same. The ultimate state is called as critical state and it can be plotted as shown in Figure 2.7.

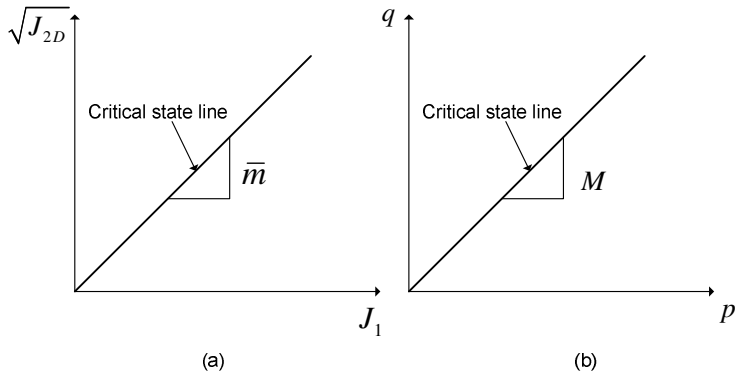

Figure 2.7 Critical state line plotted in two different stress spaces.

The yield function in the critical state model is given by

$$F = M^2 p^2 - M^2 p_0 p + q^2 = 0 \tag{2.7a}$$

where M is the slope of critical state line in q-p space (Figure 2.7 (b)), p is the mean pressure given by $p = \frac{J_1}{3}$ and $q = \sqrt{3}.\sqrt{J_{2D}}$, p_0 is the value of mean pressure where the yield surface intersects the p-axis as shown in Figure 2.8. Model parameters $\bar{m}$ (Figure 2.7a) , λ and e_0 are given by (Roscoe et al, 1958; Desai, 2001)

$$\begin{aligned} \sqrt{J_{2D}^c} &= \bar{m} J_1^c \\ e^c &= e_0^c - \lambda \ln\left(\tfrac{1}{3} J_1^c / p_a\right) \end{aligned} \tag{2.7b}$$

where superscript ‘c’ denotes the critical state. The hardening function in critical state model is defined in terms of the volumetric plastic strains.

The critical state model has certain limitations which are discussed along with salient features of the hierarchical single surface (HISS) model in section 2.3.2.2.

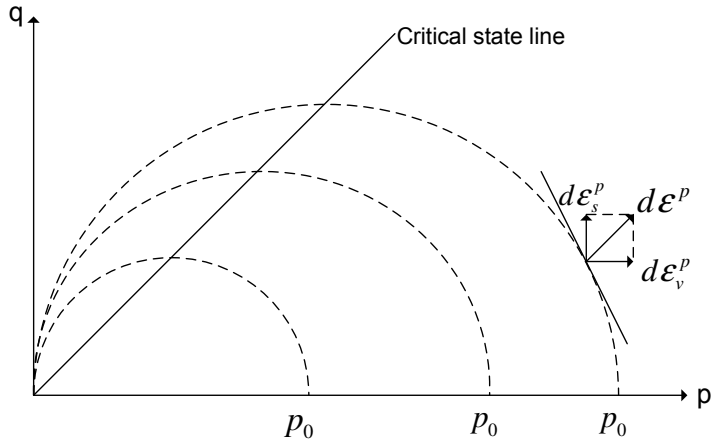

Figure 2.8 Yield surfaces in critical state model plotted in q-p plane.

2.3.2.2 Hierarchical Single Surface (HISS) plasticity model (Desai et al, 1986).

The plastic yield function in the HISS plasticity model is given by,

$$F = \overline{J_{2D}} - (-\alpha \overline{J}_1^{\,n} + \gamma \overline{J}_1^{\,2})(1-\beta S_r)^{-0.5} = 0 \tag{2.8a}$$

where $\overline{J_{2D}} = J_{2D} / p_a^2$, J_{2D} is the second invariant of is deviatoric stress tensor and p_a is the atmospheric pressure; $\overline{J_1} = (J_1 + 3R) / p_a$ where J_1 is the first invariant of the total stress tensor, R is the intercept along J_1 axis to define the cohesive strength $\overline{c}$ (Figure 2.9) given as

$$3R = \frac{\bar{c}}{\sqrt{\gamma}} \tag{2.8b}$$

n is the phase change parameter representing the volume change behavior from compaction to either dilation or no volume change; γ is the parameter related to ultimate yield surface; β is related to shape of F in the $\sigma_1 - \sigma_2 - \sigma_3$ space and S_r = stress ratio = $\sqrt{27/2}.(J_{3D}/J_{2D}^{3/2})$, J_{3D} is third invariant of the deviatoric stress tensor, α is the growth or hardening function; a simple form of α is given as

$$\alpha = \frac{a_1}{\xi^{\eta_1}} \tag{2.9}$$

where a_1 and η_1 are hardening parameters and

$$\xi = \sqrt{d\varepsilon_{ij}^p d\varepsilon_{ij}^p} \tag{2.10}$$

where ξ is trajectory of plastic strains , ε_{ij}^p , and d denotes the increment.

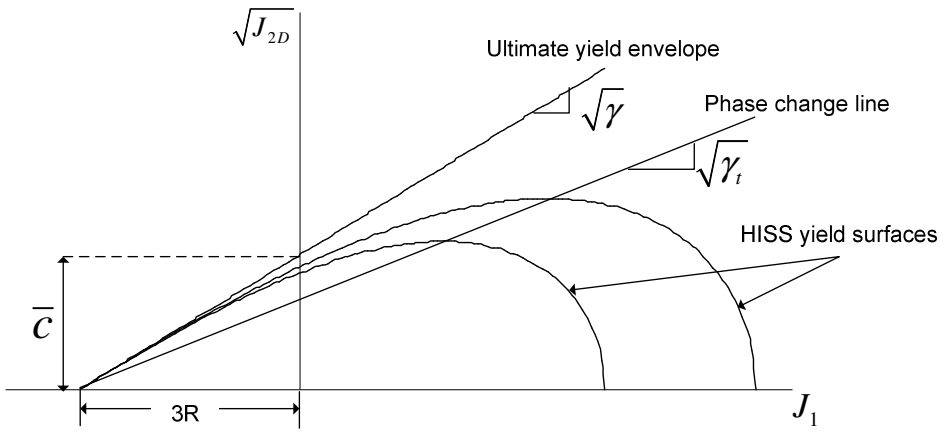

Figure 2.9 HISS yield surfaces in $\sqrt{J_{2D}} - J_1$ invariant space.

The HISS yield function given by equation 2.8 can be reduced to represent other classical plasticity models such as Von Mises, Tresca, Drucker Prager, Mohr Coulomb and critical state by using specialized values of the material parameters. Details of various specializations of the HISS model are given in Desai (2001). The HISS model has several advantages over other continuous yielding models such as critical state and Cap model (DeMaggo and Sandler, 1971). These are listed below,

1. Both critical state and Cap models assume the yielding to depend only on the volumetric plastic strains. This assumption in general may not be valid. The HISS model considers both volumetric and deviatoric parts of the plastic strains as contributing factors for yielding behavior.
2. The yield surfaces in both Critical state and Cap models plot as circular in the $\sigma_1 - \sigma_2 - \sigma_3$ stress space. It indicates that the strength of the material is independent of stress path. This may not be true for some materials. Geologic materials in particular are strongly affected by stress path. The HISS model is stress path dependent (Desai, 2001) and thus overcomes this limitation.

3. Critical state and Cap models can not model the phase change from compression to dilation before peak. Such behavior is observed in some geologic materials which can be handled by the HISS model.
4. Critical state and Cap models can not model the non associative material response. HISS-δ_1 model can handle this by defining the angle between normals to yield surface and plastic potential surface (Desai, 2001).

Thus in general HISS plasticity model provides most realistic definition of material behavior compared to other models. The disturbed state concept is a material modeling approach which can account for discontinuous nature of the deforming material and include models based on continuous assumption as special cases. Following section provides a brief discussion on DSC.

2.4 The Disturbed State Concept (DSC)

In the DSC, a deforming material element is assumed to be composed of two (or more) reference states, the relatively intact (RI) part and the fully adjusted (FA) part, Figure 2.10 (a). The material is assumed to transform continuously from the RI state to the FA state at randomly distributed locations under external excitation such as mechanical and/or thermal forces. The transformation involves microstructural changes that cause particle reorientation and relative motions. The observed behavior is expressed as a combination of individual contributions from RI and FA parts by using disturbance (D) as a coupling mechanism. As a result, when used in computational solutions DSC does not involve spurious mesh dependence (Desai, 2001).

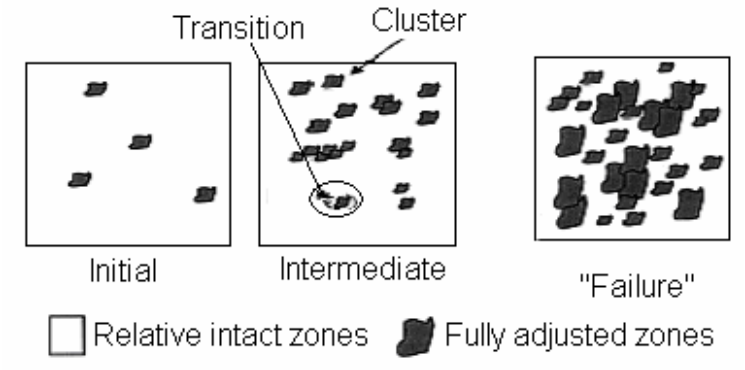

(a)

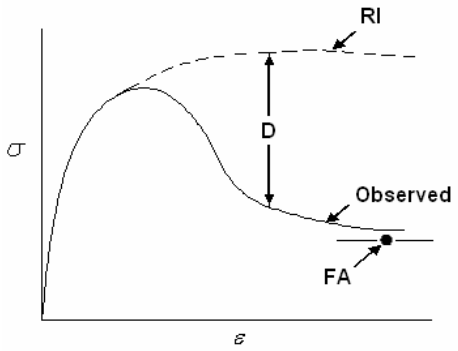

(b)

Figure 2.10 (a) RI and FA states in DSC (b) Disturbance as coupling between RI and FA states (Desai, 2001)

2.4.1 The Relative Intact (RI) state

The RI part of the material is assumed to be continuous. Thus it can be characterized by using an appropriate continuum elasticity or plasticity model. Generalized Hooke's law can be used when the RI is modelled as linear elastic. Various yield criteria such as Drucker-Prager and Mohr-Coulomb can also be used. Continuous yielding models such as critical state and hierarchical single surface plasticity (HISS) (Desai, 2001) can also be used to characterize the RI behaviour. In the present work the HISS plasticity model described section 2.3.2.2 is used.

2.4.2 The Fully Adjusted (FA) state

The material in the FA state can be defined in a number of ways, e.g.

a. It can be assumed to carry no load as in the classical damage model (Kachanov, 1986).
b. It may be considered to carry only hydrostatic stresses like in classical plasticity, or
c. It can be assumed to be in the critical state (Roscoe et al, 1958; Desai, 2001) so that it carries constant shear stress without change in volume.

2.4.3 Disturbance function (D)

The disturbance function, D, denotes the deviation of the observed state from the RI (or FA) state (Figure 2.10 (b)), and is related to microcracking and softening. It can be expressed in terms of various measured quantities such as stress, void ratio, pore water pressure for unsaturated materials, nondestructive properties such as P or S wave velocities and entropy (Desai, 2001), in terms of stress it is given by

$$D = \frac{\sigma_i - \sigma_a}{\sigma_i - \sigma_c} \tag{2.12}$$

where σ is stress and subscripts i,a and c denote RI, observed and FA states respectively. In the phenomenological sense disturbance can be defined by using the growth or decay function as

$$D = D_u[1 - \exp(-A\xi_D^Z)] \tag{2.12}$$

where ξ_D is the deviatoric plastic strain trajectory, D_u is the ultimate disturbance and A and Z are material parameters. With disturbance, D, as a coupling mechanism, the increment of observed stress can be derived as

$$d\sigma_{ij}^{\ a} = (1-D)d\sigma_{ij}^{\ i} + Dd\sigma_{ij}^{\ c} + dD(\sigma^c - \sigma^i) \tag{2.13}$$

where σ_{ij} is the stress tensor and d denotes the increment.

CHAPTER 3

CREEP MODELING AND RATE DEPENDENT BEHAVIOR

3.1 Introduction to material creep behavior

Creep is defined as growth of strains in the material over time. This section describes basic concepts in material creep behavior. A schematic of material creep response if shown in Figure 3.1.

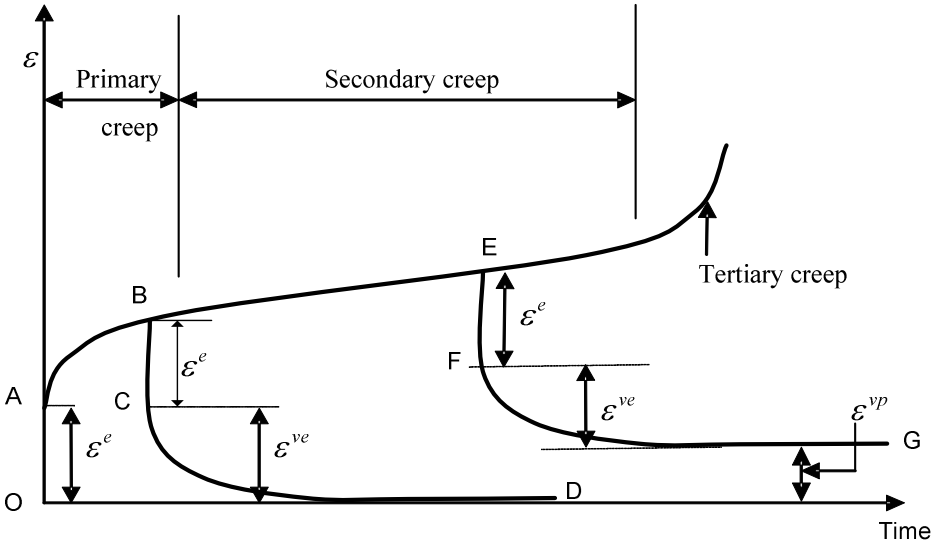

Figure 3.1 Schematic of material creep response

Upon application of the constant stress, instantaneous (elastic) strain (O-A) is observed followed by primary or elastic creep (A–B) during which, if unloading occurs, elastic recovery (B-C) results, delayed viscoelastic recovery (C-D) is observed following the elastic recovery. If the loading continues after B, secondary creep begins, accompanied by permanent deformations (strains). Unloading at any time (during B-E), say at E, will involve elastic recovery (E-F), followed by viscoelastic recovery (F–G), and then some

permanent (viscoplastic) strain is retained. Tertiary creep leading to eventual failure occurs after secondary part. The primary and secondary creep regions are important for design purposes since engineering materials usually operate in this region. Following section describes the multicomponent DSC approach for modeling primary and secondary creep.

3.2 Multicomponent DSC model (MDSC)

The MDSC assumes that the material is composed of several different components and the overall response is expressed as the cumulative effect of the behaviors of individual components. Overlay model (Pande et al, 1977; Desai, 2001) which is based on the same concept is a special case of the MDSC (Desai, 2001).

Figure 3.2(a) shows a schematic of the overlay models. Each unit is called as an overlay. Each component of the overlay represents different aspect of the material behavior. Spring, slider and dashpot represent the elastic, plastic and viscous parts, respectively. The viscoelastic (*ve*), elasto-viscoplastic (*evp*) and viscoelastic-viscoplastic (*vevp*) specializations of the overlay model can be represented as shown in Figures 3.2 (b),(c) and (d), respectively.

In some materials the viscoelastic recovery is negligible and the response can be considered to be made up of only elastic and viscoplastic parts. This is called as *evp* and is depicted in Figure 3.3. Perzyna's model which is commonly used to characterize the elasto-viscoplastic behavior is essentially the same as *evp*. Following section describes the Perzyna's elasto-viscoplastic model.

3.2.1 Perzyna's elasto-viscoplastic model

According to Perzyna's (*evp*) model the viscoplastic strain rate is given by,

$$\begin{aligned} \dot{\varepsilon}_{ij}^{vp} &= \Gamma\left(\frac{F}{F_0}\right)^N \frac{\partial F}{\partial \sigma_{ij}} \qquad if \;\; F > 0 \\ &= 0 \qquad\qquad\qquad if \;\; F \le 0 \end{aligned} \tag{3.1}$$

where $\dot{\varepsilon}_{ij}^{vp}$ is the viscoplastic strain rate tensor, Γ and N are material parameters, σ_{ij} is the stress tensor, F is the plastic yield function and F_0 is a non dimensionalizing factor.

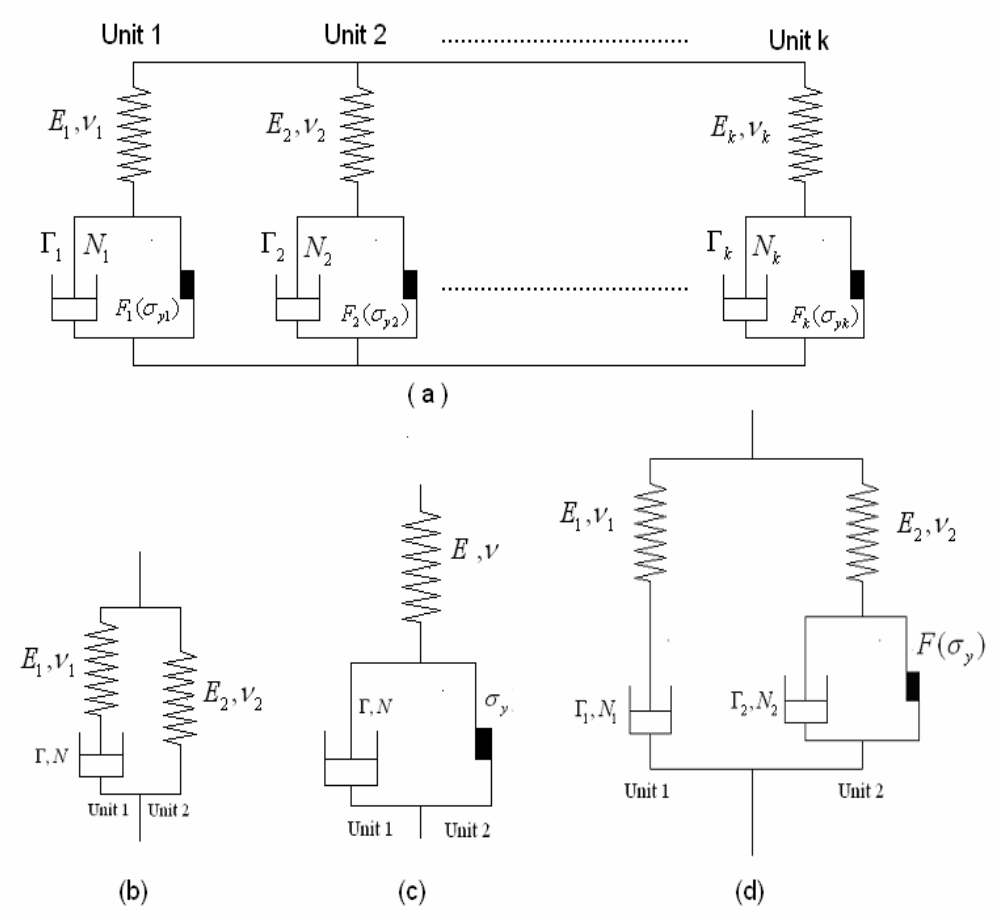

Figure 3.2 (a) Overlay model and its specializations to (b) viscoelastic (ve) model

(c) elastoviscoplastic (evp) or Perzyna model (d) viscoelastic viscoplastic (vevp) model

It can be seen that the viscoplastic strain rate in the *evp* model is dependent on the plastic yield function F. Next section describes the variation of F and strain rate with time.

3.2.1.1 Mechanics of viscoplastic response (Samtani et al, 1996).

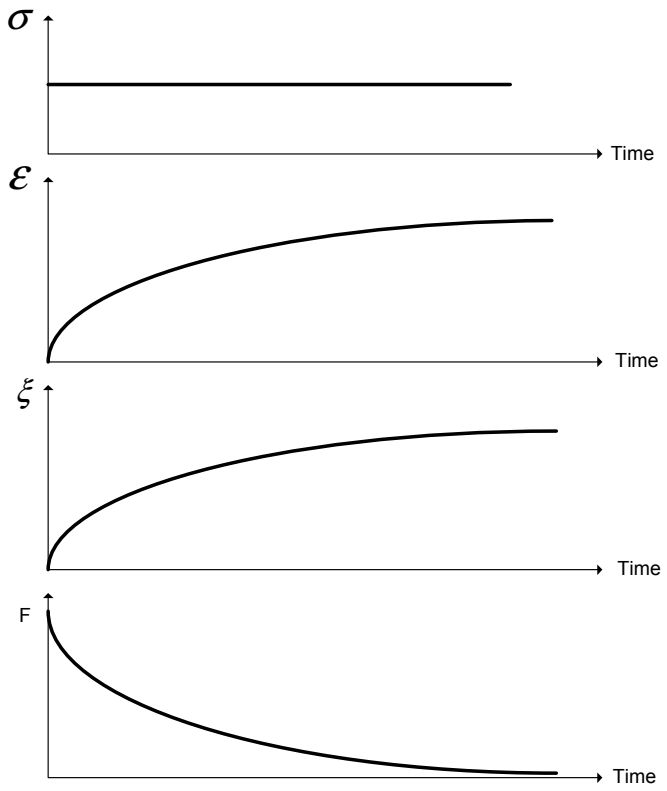

Figure 3.3 Mechanics of viscoplastic solution

Figure 3.3 Schematics of time variation of stress (σ), strain (ε), plastic strain trajectory (ξ) and yield function (F) during a creep test

Figure 3.3 shows schematics of time variation of stress (σ), strain (ε), plastic strain trajectory (ξ) and yield function (F) during a creep test. It can be seen that F has a

non zero positive value at t = 0 indicating that the material has potential to deform under applied stress. As time progresses, viscoplastic strains accumulate and F reduces gradually and approaches zero. Viscoplastic strain rate given by Equation 3.1 also reduces with F. At F = 0, viscoplastic strain rate becomes zero implying a steady state strain under an applied increment of stress. ***This defines a necessary condition that, when Perzyna's model is used, the yield function F must be defined in such a way that F = 0 corresponds to steady state strains for an applied stress increment***. In other words, the stress strain test used to define F must be such that every point on it contains a combination of stress and the corresponding steady state strain. This can be ensured by conducting the stress strain test at a very slow or 'static' strain rate. This is illustrated schematically in the following section.

3.2.1.2 Necessity for using the static yield function

Figure 3.4 (a) shows stress strain-curves at strain rates $\dot{\varepsilon}_S, \dot{\varepsilon}_1, \dot{\varepsilon}_2$ *and* $\dot{\varepsilon}_3$ where subscript 's' denotes very slow or 'static' rate and 1,2 and 3 denote increasing strain rates. Any of these four curves can be used to define yield functions F_S, F_{d1}, F_{d2} and F_{d3} which in turn can be used to predict the creep behavior. Objective of this discussion is to decide which yield function should be used in order to predict the complete creep response using the *evp* model.

At a given stress increment ($\Delta\sigma$) four different strain values, $\varepsilon_s, \varepsilon_{d1}, \varepsilon_{d2,}$ *and* ε_{d3}, are possible at strain rates $\dot{\varepsilon}_S, \dot{\varepsilon}_1, \dot{\varepsilon}_2$ *and* $\dot{\varepsilon}_3$, respectively. The corresponding plastic strains (not shown on the figure) can be assumed to be $\varepsilon_{ps}, \varepsilon_{p1}, \varepsilon_{p2}$ *and* ε_{p3} , respectively. Thus,

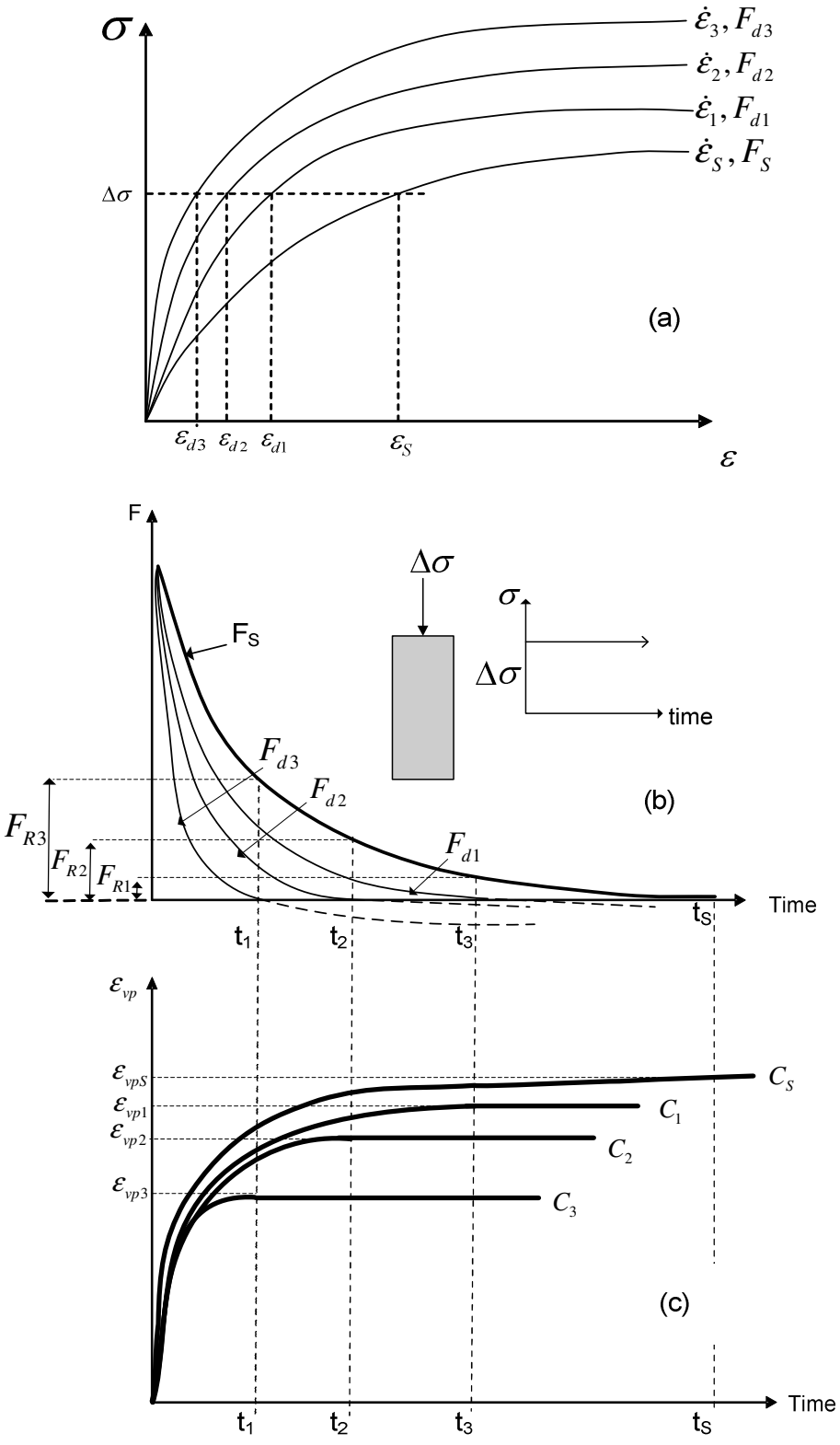

Figure 3.4 Necessity for using the static yield function.

$F_{d1} = 0$ at $\sigma = \Delta\sigma$ and ε_{p1}

$F_{d2} = 0$ at $\sigma = \Delta\sigma$ and ε_{p2}

$F_{d3} = 0$ at $\sigma = \Delta\sigma$ and ε_{p3}

$F_s = 0$ at $\sigma = \Delta\sigma$ and ε_{ps}

Figure 3.4 (b) shows time variation of these yield functions under the constant stress, $\Delta\sigma$. For example, It can be seen that F_{d3} being the one defined at fastest rate ($\dot{\varepsilon}_3$) reaches zero in shortest time (t_1). Viscoplastic strain rate predicted by using F_{d3} also becomes zero at $t = t_1$ (Equation 3.1). Thus, by using F_{d3}, viscoplastic strains greater than ε_{vp3} may not be predicted. Schematic of the predicted creep behavior by using F_{d3} is shown by curve C_3 in Figure 3.4 (c). Similarly F_{d2}, F_{d1} and F_s may predict curves C_2, C_1 and C_s, respectively. Note that, by using F_s, maximum viscoplastic strain can be predicted compared to other yield functions. This is primarily because it is defined based on the static curve which represents the steady state strains for corresponding applied stresses.

As shown in Figure 3.3 the time at which the yield function approaches zero must coincide with the time at which the strain reaches steady state and strain rate becomes zero. In other words, the yield function should represent the deformation potential of the material under a given load. Yield function defined using the static curve accurately represents the deformation potential. Hence at $F \neq 0$ the material continues to deform and reaches equilibrium state at $F = 0$. On the other hand, If other curves (at higher rates) are used, F does not represent the deformation potential accurately i.e., F reaches zero even though the material has not reached an equilibrium or steady state.

During determination of viscous parameters (Section 4.3.1.8) it is necessary to compute the value of yield function at number of points on the creep test curve. If the yield functions are defined based on the higher rate tests, they become negative as shown by the dotted parts of the curves in Figure 3.4 (b). Thus the viscous parameters may not be determined using the tests at higher rates and static curve must be used.

The static stress strain curve is usually not available from the laboratory tests and needs to be constructed. A procedure to construct the static curve from available creep tests is described in the following section.

3.2.2.2 Procedure to construct the static curve

Figure 3.5 (a) shows results of creep tests (Xiao, 2004) for SAC alloy at 45^0C performed at various constant axial stresses. A creep test spans over a longer period of time that allows sufficient time for deformation. Thus asymptotic strain from creep test for a given constant stress increment may be considered to represent steady state. Thus points 1,2,3,4 and 5 (Figure 3.5 (a)) represent such steady state strains at applied constant stresses of 10.54, 12.30, 14.25, 15.92 and 17.05 MPa, respectively. Each such point represents a combination of a stress and corresponding strain at the steady state. These points can be used to construct the static stress–strain curve (Figure 3.5b). A smooth curve passing through these points plotted on the stress- strain diagram can be considered as the static curve (Figure 3.5b). It represents the material response when the stress-strain test is conducted at a very slow strain rate. Term ‘very slow’ means that further reduction in strain rate does not produce significant difference in the stress-strain behavior of the material. Figures 3.5 (c) and (d) show construction of static curve for Sky Pilot till at 100

kPa confining pressure. The creep tests for Sky Pilot till at various axial loads are conducted in the laboratory which are discussed later in Section 6.4.

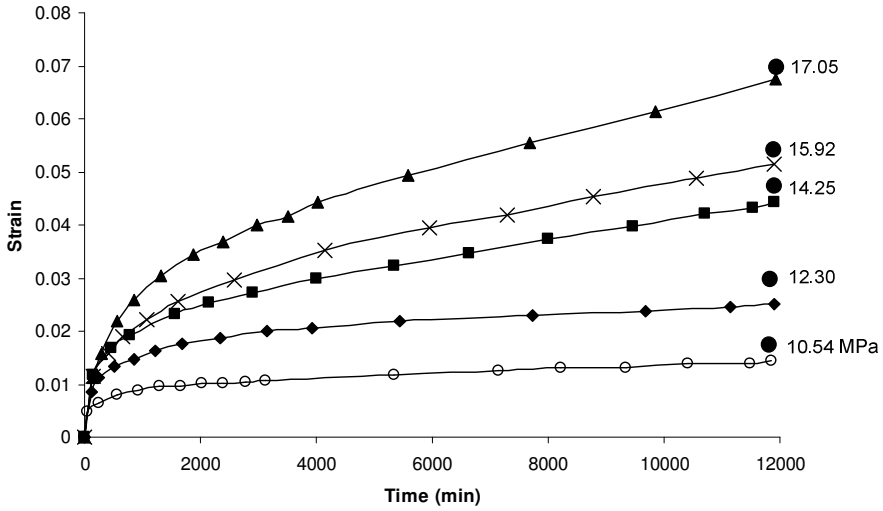

(a) Creep test data at various axial loads (Xiao and Armstrong, 2004)

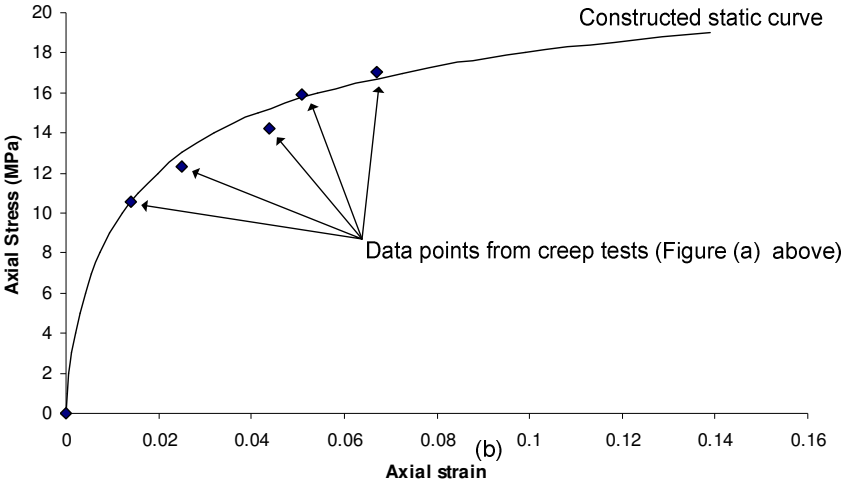

(b) Construction of estimated static curve

Figure 3.5 (a) and (b) Construction of static stress strain curve for SAC alloy based on creep test results at 45^{o}C (Xiao and Armstrong, 2004). (c) and (d) Construction of static curve for Sky Pilot till at 100 kPa.

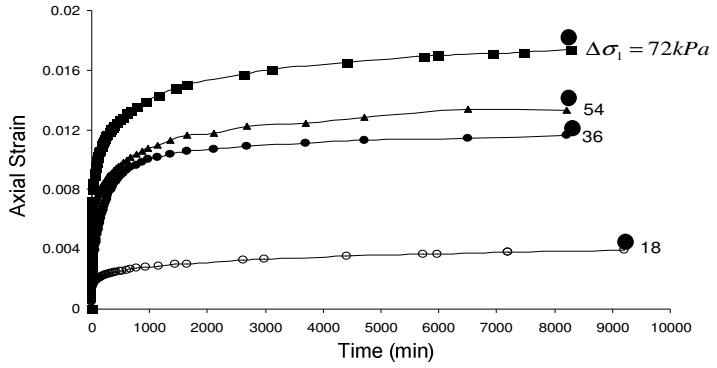

(c) Creep test data at various axial loads for Sky Pilot till at 100 kPa confining pressure

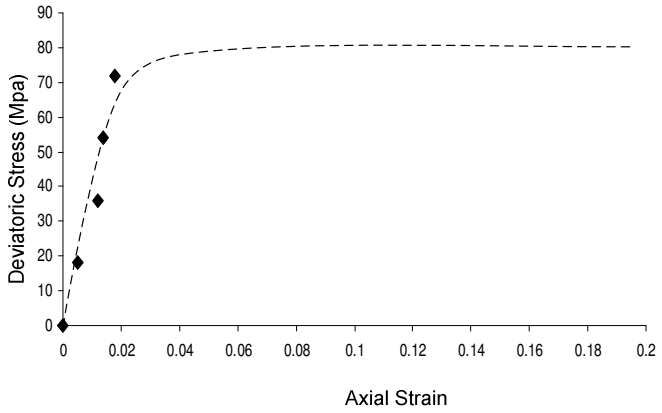

(d) Constructed Static curve for Sky Pilot till at 100 kPa confining pressure

Figure 3.5 (continued).

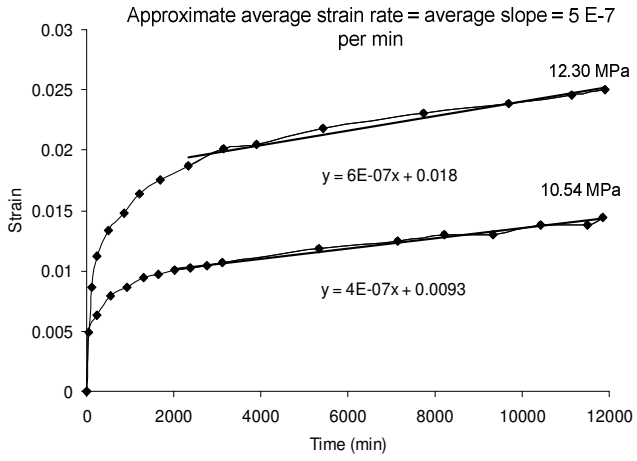

Figure 3.6: Calculation of approximate average strain rate during creep tests on Sn/3.9Ag/0.6Cu at 45^{o}C.

Strain rate associated with the static curve may be determined approximately from the creep tests (Figure 3.6) as discussed here. It is considered as the average slope of the creep curves at various axial loads computed in the secondary creep region (as shown in the figure) where the curves are reasonably flat. Secondary creep (Desai, 2001) being the predominant creep mode for many materials, this assumption can be considered to be realistic. For SAC lead free solder the static rate is computed as 5×10^{-7} per min (Figure 3.6). It may be considered that the static curve represents the stress-strain response of the material when the test is conducted at a very slow rate.

The constructed static curve is used to define the yield function F in the *evp* model (Equation 3.1) to predict the time dependent material response. Typical creep predictions for SAC solder alloy at various temperatures are presented in Chapter 5.

3.3 Rate Dependent Material Behavior

Figure 3.7 shows a schematic of rate dependent material behavior. The response at static condition is given by the static curve denoted by subscript '$_s$'. Curves at higher rates are termed as 'dynamic' and they are denoted by subscript '$_d$'. In general, material response becomes stiffer as the applied strain rate increases. The HISS model in its current form (Equation 2.8a) does not include the effect of strain rate. Thus different set of material parameters are needed to characterize material response at different strain rates. This requires different sets of stress-strain test data (as shown in Figure 3.7) which may not always be available. To overcome this limitation, the HISS yield function may be modified to include the rate effect (Baladi and Rohani, 1984). Following Equation

gives the modified form of the HISS yield function that includes the rate dependent function (F_R).

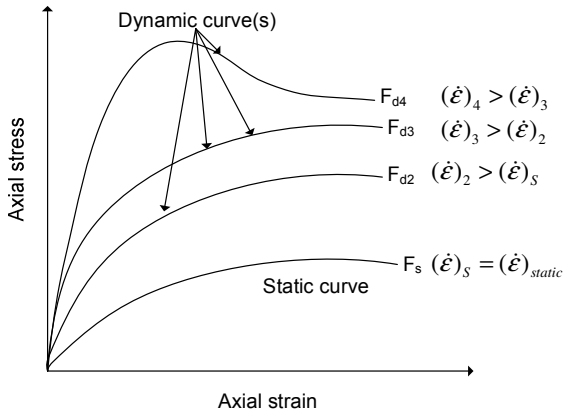

Figure 3.7 Schematic of rate dependent material behavior

$$F_d(\sigma, \alpha, \dot{\varepsilon}) = \frac{F_S(\sigma, \alpha) - F_R(\dot{\varepsilon})}{F_0} = 0 \tag{3.2}$$

here F_d represents the plastic yield function defined at non static or 'dynamic' rate and F_0 is the factor used to render the term non dimensional. The rate dependent function F_R can be derived as discussed in the following section.

3.3.1 Derivation of Rate Dependent Function (F_R)

Squaring both sides and taking square root of Equation 3.1 yields,

$$\Gamma(\frac{F_s}{F_0})^N = \sqrt{\frac{(\frac{d\varepsilon_{ij}^{vp}}{dt})^T.(\frac{d\varepsilon_{ij}^{vp}}{dt})}{(\frac{\partial F_S}{\partial \sigma_{ij}})^T.(\frac{\partial F_S}{\partial \sigma_{ij}})}} \tag{3.3}$$

$$\frac{F_s}{F_0} = \{(\frac{1}{\Gamma}).\sqrt{\frac{(\frac{d\varepsilon_{ij}^{vp}}{dt})^T.(\frac{d\varepsilon_{ij}^{vp}}{dt})}{(\frac{\partial F_S}{\partial \sigma_{ij}})^T.(\frac{\partial F_S}{\partial \sigma_{ij}})}}\}^{\frac{1}{N}} \tag{3.4}$$

Thus

$$\frac{F_s}{F_0} - \{(\frac{1}{\Gamma}).\sqrt{\frac{(\frac{d\varepsilon_{ij}^{vp}}{dt})^T.(\frac{d\varepsilon_{ij}^{vp}}{dt})}{(\frac{\partial F_S}{\partial \sigma_{ij}})^T.(\frac{\partial F_S}{\partial \sigma_{ij}})}}\}^{\frac{1}{N}} = 0 \tag{3.5}$$

Comparing (3.5) with (3.2) gives,

$$\frac{F_R}{F_0} = \{(\frac{1}{\Gamma}).\sqrt{\frac{(\frac{d\varepsilon_{ij}^{vp}}{dt})^T.(\frac{d\varepsilon_{ij}^{vp}}{dt})}{(\frac{\partial F_S}{\partial \sigma_{ij}})^T.(\frac{\partial F_S}{\partial \sigma_{ij}})}}\}^{\frac{1}{N}} \tag{3.6}$$

Equation 3.6 gives the rate dependence factor F_R as a function of strain rate. Figure 3.8 shows variation of F_R with strain rate. This calculation was performed based on material parameters and test results for SAC lead free solder alloy at 45 degrees.

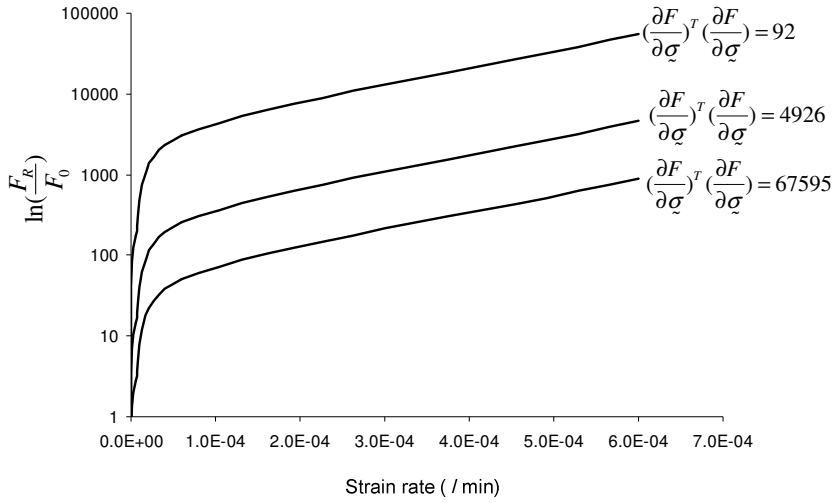

Figure 3.8 Variation of Rate dependent function F_R with strain rate for SAC alloy.

It can be seen that F_R reduces with the strain rate and approaches zero as strain rate tends to zero. Concept of zero-strain-rate is theoretical and it can be considered as a very slow or static rate in practice. Thus it can be said that F_d (Equation 3.2) reduces to $\frac{F_s}{F_0}$ (Equation 2.8) at static rate. Hence F_s may be considered as a special case of F_d at static rate.

CHAPTER 4

PARAMETER DETERMINATION

4.1 Introduction

This chapter describes the procedure of parameter determination for the DSC model. In general the DSC model parameters can be divided into following parts

1. Elastic
2. Plastic – HISS
3. Disturbance
4. Viscous
5. FA (critical) state parameters

In this research the DSC is applied for characterizing lead free solders (Chapter 5) and glacial tills (Chapter 6). Parameter determination procedure in general is the same for both materials; however, some minor differences exist. Thus parameter determination procedure for each of the two materials is given separately with examples.

Following section identifies specific parameters in the DSC model. Procedure to determine these parameters is discussed in sections 4.3 onwards.

4.2 Material parameters in DSC

Table 4.1 lists different parameters in five categories of parameters in the DSC model.

Table 4.1 Different parameters in the DSC model

Category	**Parameter**	**Symbol**	**Equation #**
Elastic	Elastic Modulus	E	2.1a
	Poisson's ratio	ν	2.1b
Plastic - HISS	Ultimate parameter	γ	2.8a
	Ultimate parameter	β	2.8a
	Phase change parameter	n	2.8a
	Cohesive strength	$\bar{c}$	2.8b
	Hardening parameter	a_1	2.9
	Hardening parameter	η_1	2.9
Disturbance	Disturbance parameter	A	2.11
	Disturbance parameter	Z	2.11
Viscous	Fluidity parameter	Γ	3.1
	Flow exponent	N	3.1
FA (critical) state	Slope of critical state line	$\bar{m}$	2.7b
	Slope of consolidation line	λ	2.7b
	Reference void ratio	e_0	2.7b

4.3 Procedure for Parameter determination (Desai, 2001)

Behavior of solder alloys is not affected significantly by the confining pressure unlike geologic materials; however, it is strongly affected by temperature. Thus the tests on glacial tills are conducted at various confining pressures whereas tests on solder alloys are conducted at various temperatures. This is consistent with the predominant loading modes for these materials. In other words, the glacial tills usually operate at a fairly constant temperature unlike solder alloys and solder alloys which operate at constant confining pressure unlike glacial tills. Thus the parameters for solder alloys are temperature dependent and those for glacial tills are dependent on confining pressure. Following sections describe the parameter determination procedures for each.

Parameter determination of glacial tills or geologic materials in general is more involved due to the added complexity in material behavior compared to solder alloys. Thus a procedure (general) for determination of parameters of the glacial tills is first presented followed by specialized procedure for solder alloys.

Determination of material parameters described in following sections is based on the test data presented in chapters 5 and 6. Glacial till parameters are based on CTC and creep tests presented in section 6.7 and those for solder alloys are based on test results presented in section 5.3.

4.3.1 Parameters for Glacial Tills

4.3.1.1 Elastic parameters, E and ν

The Elastic modulus, E, is computed from the average slope of the unloading portion of the stress-strain response as shown in Figure 4.1. The Poisson's ratio, υ, is taken to be

0.45 (less than 0.50) since the sample is fully saturated and is tested under undrained conditions. For Tiskilwa till the value of E at $\sigma_3^{'} = 100kPa$ is obtained as 38000 kPa.

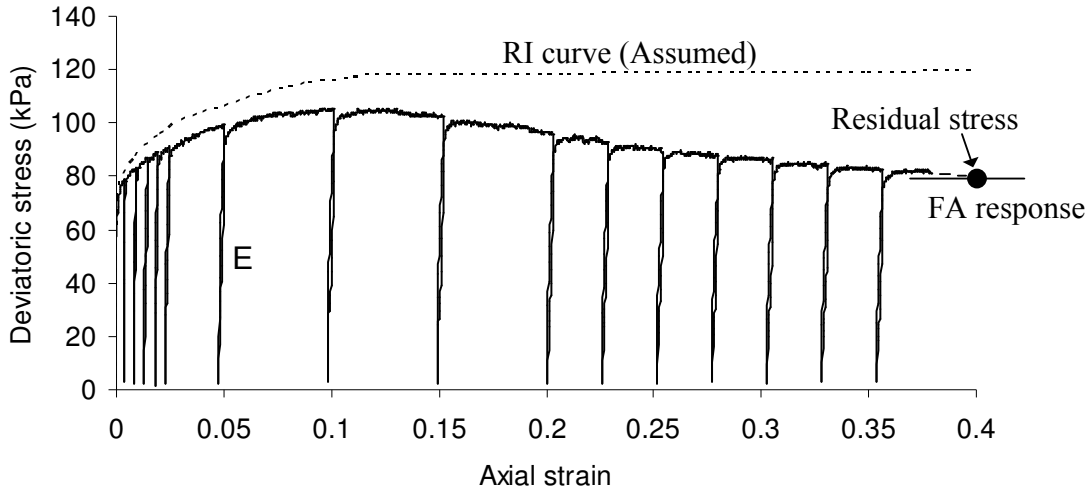

Figure 4.1 CTC test curve and unloading slopes used in Calculation of the Elastic Modulus, *E.*

Sample calculation shown here is for conventional triaxial test (CTC) for the Tiskilwa till at 100 kPa confining pressure (Section 6.7).

Elastic modulus of the glacial till is observed to vary considerably with confining pressure. Figure 4.2 shows this variation for Tiskilwa and Sky-pilot tills.

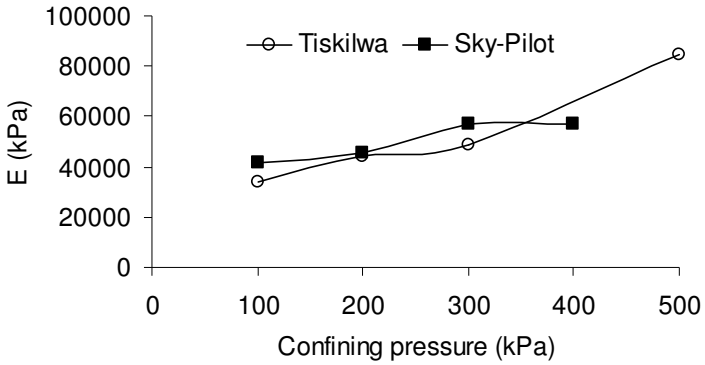

Figure 4.2 Variation of elastic modulus with confining pressure

4.3.1.2 Ultimate parameters, γ and β

The parameter γ represents the slope of the ultimate yield envelope. The ultimate envelope is assumed to be a straight line for this work. Equation for the ultimate yield function is obtained by substituting $\alpha = 0$ in Equation 2.8a. It is given by Equation 4.1

$$F_u = \overline{J_{2D}} - (\gamma \overline{J_1}^2)(1 - \beta S_r)^{-0.5} = 0 \tag{4.1}$$

To obtain the value of γ, the ultimate envelope is plotted (Figure 4.3). The ultimate envelope is plotted by using the peak RI stresses at various confining pressures. The RI behavior is assumed to be that if the material remained a continuum. It is obtained by assigning the ultimate RI stress as about 10% greater than the observed peak stress value and then constructing a smooth curve from the initial curve to the ultimate stress (Figure 4.1). After obtaining the peak RI stresses at different confining pressures

the invariants of the stress tensor, J_1 and $\sqrt{J_{2D}}$, are computed and the ultimate envelope is plotted (Figure 4.3). γ is computed from the slope of the ultimate envelope. For the Tiskilwa Till, γ is computed to be 0.0177.

β denotes the shape of the yield function in the σ_1-σ_2-σ_3 space. It is computed by solving Equation 4.1 for the condition $F_u = 0$. Previously computed value of γ is used in the process. For Tiskilwa till β is computed as 0.36.

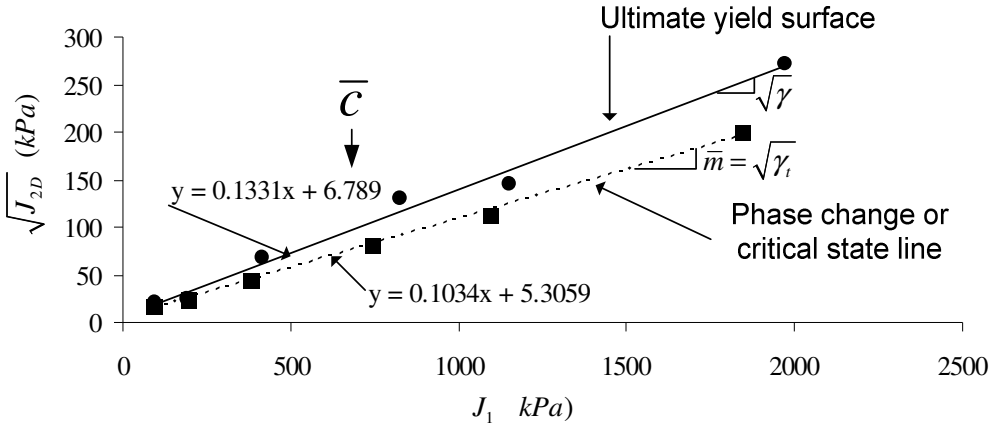

Figure 4.3 Calculation of the ultimate parameter, γ, and critical state parameter, $\overline{m}$.

4.3.1.3 Cohesive Strength, $\overline{c}$

The cohesive strength $\overline{c}$ is the intercept of the ultimate envelope (Figure 4.3) on the $\sqrt{J_{2D}}$ axis when $J_1 = 0$. For Tiskilwa till it is obtained as 6.789.

4.3.1.4 Phase change parameter

The phase change parameter signifies the phase transformation of the material from the compaction to the dilation state. From the CTC test data, the critical state

stresses are obtained at each confining pressure; they are assumed to be equal to the residual stresses (Figure 4.1). Stress invariants J_1 and $\sqrt{J_{2D}}$ are then calculated at each confining pressure to plot the critical state line (Figure 4.3). The value of n is computed from the following equation (Desai, 2001):

$$n = \frac{2}{1 - \left(\gamma_t / \gamma\right)^2} \tag{4.2}$$

where γ_t is the square of the slope of critical state or phase change line, Figure 4.3. Based on CTC test results for the Tiskilwa Till, n is computed to be 3.6.

4.3. 1.5 Hardening Parameters a_1 and η_1

Based on Equation 2.10, the plastic strain trajectory is computed at various points on the CTC test curves. Knowing values of γ, β, n, and $\bar{c}$ from previous steps, α is computed from Equation 2.8a at the same points that are used to compute the plastic strain trajectory. Equation 2.9 can be expressed as

$$\ln \alpha + \eta_1 \ln \xi = \ln a_1 \tag{4.3}$$

A plot according to equation of 4.3 (ln(α) vs. ln(ξ)) is plotted (Figure 4.4). The slope of the approximate straight line gives the value of η_1. The intercept of the line along the ln(α) axis at $\xi = 1$ gives the value of a_1. Figure 4.4 shows a typical plot for the Tiskilwa

till CTC test, at σ_3' = 100 kPa. From this plot, values of a_1 and η_1 (at σ_3' = 100 kPa) are 0.0002 and 0.175, respectively.

Figures 4.5 (a) and (b) show variation of a_1 with confining pressure for Tiskilwa and Sky-pilot tills, respectively. Figures 4.5 (c) and (d) show variation of and η_1 with confining pressure for Tiskilwa and Sky-pilot tills, respectively.

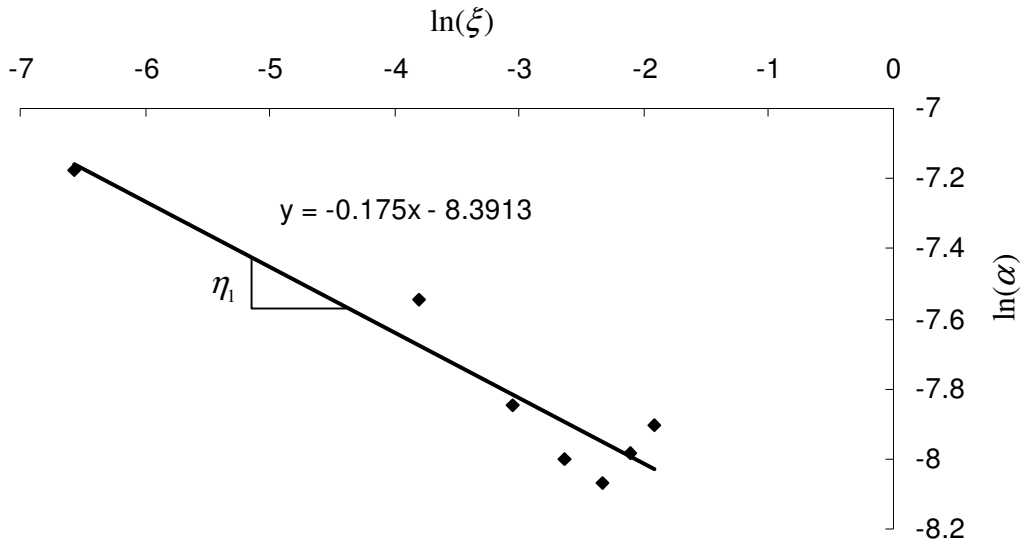

Figure 4.4 Calculation of hardening parameters at σ_3' = 100 kPa.

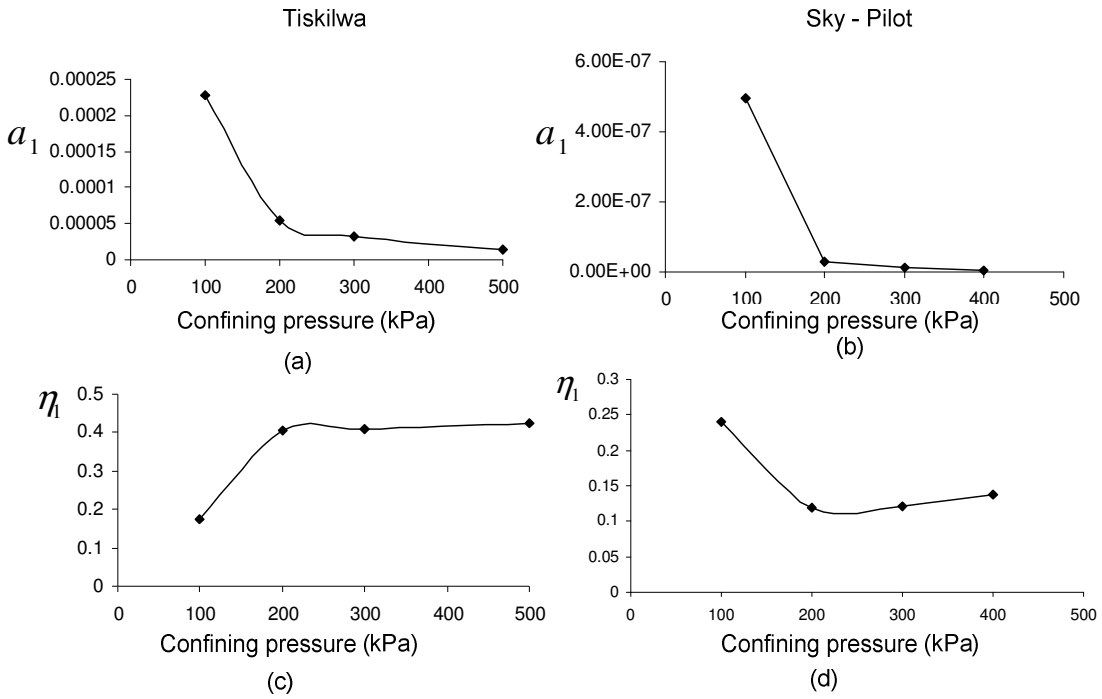

Figure 4.5 Variation of hardening parameters with confining pressure

4.3. 1.6 FA (critical state) parameters, $\overline{m}$ and λ

Based on Equation 2.7b, $\overline{m}$ is computed as the slope of the critical state or phase change line (Figure 4.3). For the Tiskilwa till $\overline{m}$ is computed to be 0.1034.

The parameter λ is obtained as the slope of the consolidation line. To plot the consolidation line, void ratio and mean pressure values before and after consolidation are required. For the CTC tests, water content is recorded before consolidation starts, and initial void ratio e_0 is computed from

$$S \cdot e_0 = w \cdot G_s \tag{4.4}$$

where S is degree of saturation (S = 1 for fully saturated case), e is void ratio, w is water content, and G_s is specific gravity of the soil (assumed to be 2.65). Change in void ratio during consolidation is computed using the following equation

$$\Delta H = \frac{H_0}{1+e_0}(\Delta e) \tag{4.5}$$

where ΔH is the change in sample height during consolidation, H_0 is the original sample height, e_0 is void ratio at the beginning of consolidation, and Δe is the change in void ratio due to consolidation. For the Tiskilwa Till, the initial void ratio, e_0, is found to be 0.477. Void ratio after consolidation can be computed by subtracting Δe from the original void ratio. Pressure at the start of consolidation is the atmospheric pressure p_0, and the consolidation pressure is the confining pressure, σ_3'. After obtaining the initial and final void ratios and pressure values, the consolidation line can be plotted. A typical plot of void ratio vs. ln (p), for the Tiskilwa Till at σ_3' = 100 kPa is shown in Figure 4.6, from which λ is computed to be 0.23.

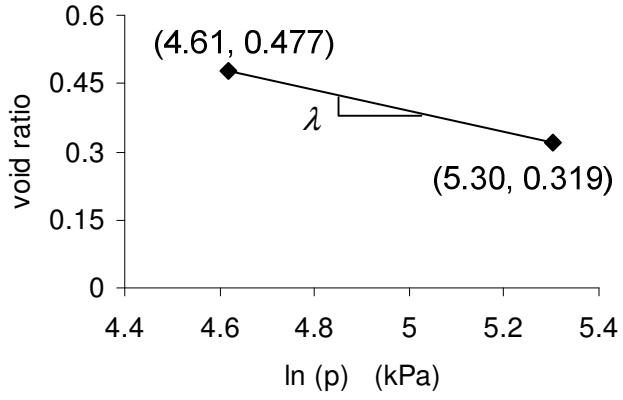

Figure 4.6 Determination of λ for σ_3' = 100 kPa

4.3.1.7 Disturbance Parameters, *A* and *Z*

Disturbance, *D*, in CTC test specimen is computed based on Equation 2.11 at various points on the stress strain curve. For this purpose, the RI curve is constructed as described above, and FA strength is assumed to be the asymptotic residual strength (Figure 4.1).

To obtain the parameters *A* and *Z* for the disturbance function, Equation 2.12 is transformed as

$$Z\ln(\xi_D) + \ln(A) = \ln\left[-\ln\left(\frac{D_u - D}{D_u}\right)\right] \tag{4.6}$$

The values of ξ_D and *D* are computed from various points on the observed stress strain curve. Assuming $D_u = 1$, the plot of ln(-ln(1-*D*)) vs. ln(ξ_D) (Figure 4.7) gives *Z* as the slope of the average straight line, and *A* as the intercept along the ln(ξ_D) axis at ξ_D=1. Based on the number of CTC tests, average disturbance parameters are computed. For the Tiskilwa Till, average *A* and *Z* are computed to be 20.2 and 2.68, respectively.

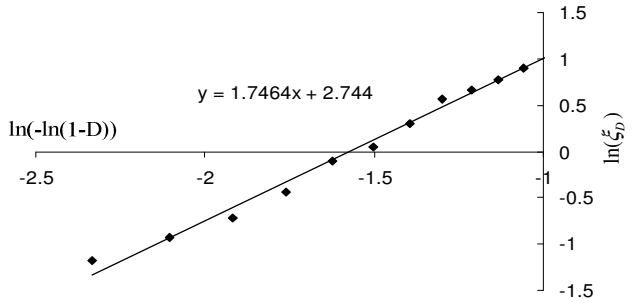

Figure 4.7 Determination of disturbance parameters, *A* and *Z*.

4.3.1.8 Determination of viscous parameters

As discussed in chapter 3, the MDSC model is used to model the creep behavior of the materials. Both *evp* and *vevp* (Section 3.2) specializations of the MDSC are used for the glacial till. As discussed in section 3.2.1.1 the yield function needs to be defined by using the static curve for characterizing the full creep behavior. Procedure for constructing the static curve is presented in 3.2.1.2. The procedure to determine the *evp* parameters based on the static yield function is discussed in the following sections.

4.3.1.8.1 Parameters for evp model (Γ, N)

Equation 3.1 gives the viscoplastic strain rate for *evp* model. It can be rearranged as follows

$$\ln \Gamma + N.\ln(\frac{F}{F_0}) = \ln a \tag{4.7}$$

where,

$$a = \sqrt{\frac{2\dot{I}_2^{vp}}{(\frac{\partial F}{\partial \underset{\sim}{\sigma}})^T.(\frac{\partial F}{\partial \underset{\sim}{\sigma}})}} \tag{4.8}$$

where $\dot{I}_2^{vp} = \frac{1}{2}\dot{\varepsilon}_{ij}^{vp}.\dot{\varepsilon}_{ij}^{vp}$, which is the second invariant of the viscoplastic strain rate tensor.

Parameter N can then be obtained as the slope of the $\ln a$ vs $\ln(\frac{F}{F_0})$ plot and Γ is obtained from the intercept on the $\ln a$ axis at $\frac{F}{F_0}=1$. One such typical plot is shown in Figure 4.8. From the plot shown, Γ = 6 x 10^{-6} and N = 1.03. One such set of Γ and N is obtained from each creep curve at a given confining pressure and the average of such sets is used for validation. For Sky-pilot till the average creep parameters at 100 kPa are determined as Γ = 5.5 x 10^{-6} and N = 1.625.

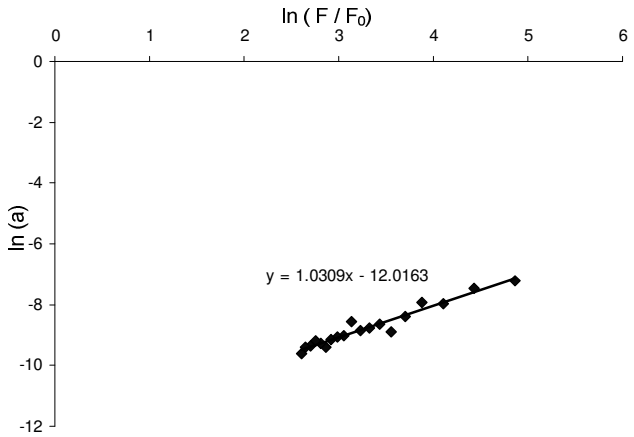

Figure 4.8 Calculation of creep parameters for Sky-Pilot till at $\sigma_3^{'}=100kPa$ and $\Delta\sigma_1=72kPa$ (80% of the peak stress)

4.3.1.8.2 Parameters for *vevp* model $(E_1, E_2, \Gamma_1, \Gamma_2, N_1, N_2)$

The *vevp* specialization of the overlay model considers viscoelastic strains in addition to the elastic and viscoplastic strains considered in *evp* model. The *vevp* model can be represented as shown in Figure 3.2 (d). Some of the material parameters in the *vevp* model are same as those in the *evp* model and some are determined from the creep

test data. An approximate procedure for parameter determination is given here (Desai, 2001).

Assuming that the load, σ_0, is applied to the system at time $t = 0$, the equilibrium equation can be written as

$$\sigma_1 t_1 + \sigma_2 t_2 = \sigma_0 (t_1 + t_2) \tag{4.9}$$

where t_1 and t_2 are the thicknesses of overlays (assumed to be 0.5) and the subscripts 1 and 2 indicate the first and second overlay units, respectively (Desai, 2001). Instantaneous strain ε_0 (Figure 4.7) due to σ_0 is given by

$$\varepsilon_0 = \frac{\sigma_0}{E_1 t_1 + E_2 t_2} \tag{4.10}$$

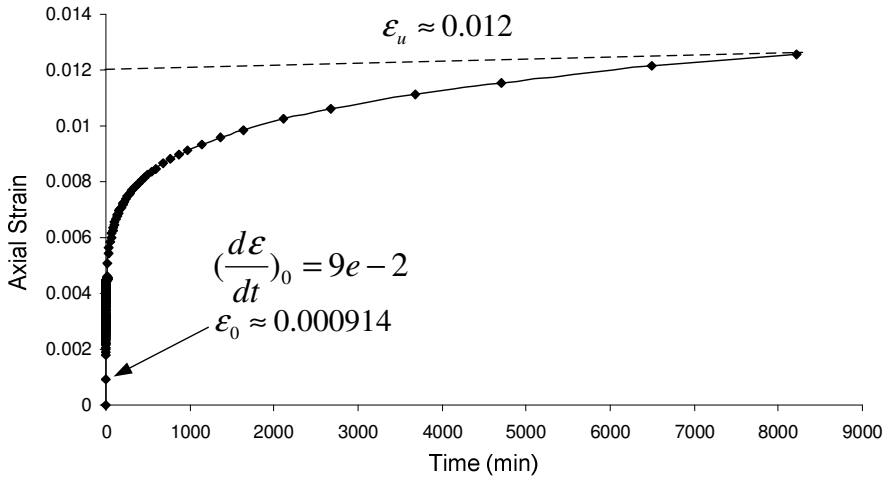

Figure 4.9 Initial and ultimate strains in a typical creep test. $\sigma_3' = 100$ kPa and $\sigma_1' = 136$ kPa (40% of peak stress).

As time $t \rightarrow \infty$ the ultimate strain, ε_u, can be written as

$$\varepsilon_u = \frac{\sigma_0}{E_2 t_2} \tag{4.11}$$

The values of ε_0 and ε_u can be obtained from the measured response, Figure. 4.9. Solution of Equations (4.10) and (4.11) simultaneously gives the values of E_1 and E_2. From Figure 4.9 the values of E_1 and E_2 are computed to be 6666 kPa and 76817 kPa, respectively. Poisson's ratio for each overlay unit is assumed to be 0.45.

To calculate the viscous parameter Γ, the gradient of strain, $\frac{d\varepsilon}{dt}(0)$, at $t = 0$ can be measured approximately from the strain-time curve as

$$\frac{d\varepsilon}{dt}(0) \approx \left(\frac{\varepsilon_{t+1} - \varepsilon_t}{\Delta t} \right)_0 \tag{4.12}$$

where, ε_{t+1} and ε_t are the values of strains at $t = 0$, and Δt is a small time step. The value of Γ can be obtained from

$$\frac{d\varepsilon}{dt}(0) = \frac{\Gamma E_1^2 t_1 \sigma_0}{(E_1 t_1 + E_2 t_2)^2} \tag{4.13}$$

Derivation of Equation (4.13) is given in Desai, (2001). Substituting E_1 and E_2 computed above gives the value of Γ_1. For creep test shown in Figure 4.9, the value of Γ_1 is computed as 0.001446. Repeating this calculation for ultimate strain rate gives the value of Γ_2. Parameter N_2 is assumed to be same as N in the *evp* model (Desai, 2001). It may be necessary to modify the value of elastic moduli with respect to curve shown in Figure 4.9 for improved predictions.

Table 4.2 below lists parameters for Tiskilwa and Sky-pilot tills obtained by following above procedures.

Tables 4.3 and 4.4 list the viscous parameters for *evp* and *vevp* models, respectively.

Table 4.2 Elastoplastic parameters for Tiskilwa and Sky-pilot tills

Category	**Symbol**	**Tiskilwa Till**	**Sky-Pilot Till**
Elastic	E	52732	50470
	ν	0.45	0.45
Plastic - HISS	γ	0.0178	0.0092
	β	0.36	0.52
	n	3.6	6.85
	$\bar{c}$	6.789	16.67
Plastic - hardening	a_1	2e-4	1.35e-7
	η_1	0.27	0.14
Disturbance	A	20.2	5.5
	Z	2.68	1
FA (critical) state	$\bar{m}$	0.1	0.09
	λ	0.21	0.16
	e_0	0.48	0.52

Table 4.3 *evp* model parameters (Static) for Sky-Pilot till

Category	**Symbol**	**100 kPa**	**200 kPa**	**400 kPa**
Elastic	E	41000	45000	58000
	ν	0.45	0.45	0.45
HISS	γ	0.0092	0.0092	0.0092
	β	0.52	0.52	0.52
	n	6.85	6.85	6.85
	$\overline{c}$	16.67	16.67	16.67
	a_1	5×10^{-7}	2.43×10^{-9}	2.45×10^{-9}
	η_1	1.33	1.23	1.24
Creep(*evp*)				
	Γ	5.5E-06	2.17E-07	3.4E-08
	N	1.625	2.2	2

Table 4.4 *vevp* model parameters for Sky-Pilot till

***vevp* creep**	**Confining pressure ($\sigma_2 = \sigma_3$)**		
	100 kPa	**200 kPa**	**400 kPa**
E_1 **(kPa)**	6666	24244	30000
E_2 **(kPa)**	42500	83333.33	63333.33
ν_1	0.45	0.45	0.45
ν_2	0.45	0.45	0.45
Γ_1 **(kPa^{-1}min^{-1})**	0.001446	0.001841	4.24E-06
Γ_2 **(kPa^{-1}min^{-1})**	0.006	0.006	0.006
N_1	2.275	4	1.4
N_2	1.625	2.2	2

4.3.2 Parameters for solder alloys

The DSC model parameters are temperature dependent for solder alloys and the temperature dependence is represented as

$$P = P_r \left(\frac{T}{T_r}\right)^C \tag{4.14}$$

where P is any parameter, subscript r denotes the value of the parameter at reference temperature, T is temperature in Kelvin and C is the exponent to be determined for each parameter. Reference temperature used for this work is 25° C or 298 K. The following sections describe the procedure for determination of parameters and the corresponding temperatures exponents.

4.3.2.1 Elastic parameters, *E* and *v*

The elastic modulus, *E*, for solder alloys can be determined by various methods. It can be taken as the slope of the initial part of the loading curve or unloading slope if available. Other non-destructive techniques may also be used as described by Vianco, (2003). Elastic modulus for SAC alloy at room temperature is adopted as average value of those reported by Wiese et al, (2001) and Zeng, (2005) to be 40 GPa. Similarly, Poisons ratio is also adopted to be 0.3474. Table 4.5 shows values of elastic moduli at various temperatures as given by Wiese et al(2001).

To obtain the temperature exponent for elastic modulus, equation 4.14 is written as

$$\ln(\frac{P}{P_r}) = C.\ln(\frac{T}{T_r}) \tag{4.15}$$

Table 4.5 Variation of elastic modulus with temperature (Wiese, 2001)

E (GPa)	Temperature (K)
45	298
43	323
40	348
35	373

C can be determined from the slope of $\ln(\frac{P}{P_r})$ vs $\ln(\frac{T}{T_r})$ plot. Such plot for elastic modulus is shown in Figure 4.10. The temperature exponent C is obtained as -1.09.

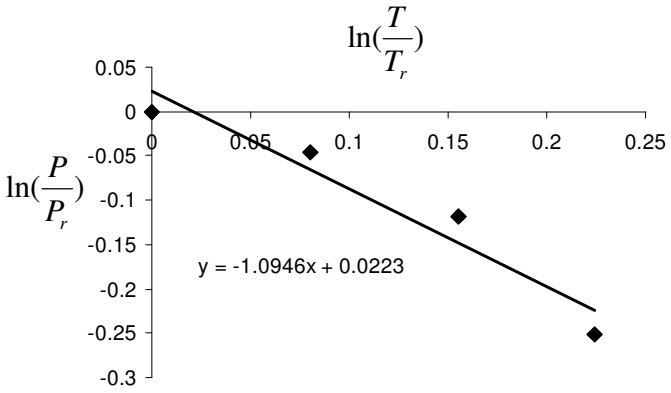

Figure 4.10 Determination of temperature exponent for E.

Variation of Poisson's ratio with temperature considered negligible and corresponding temperature exponent is taken to be zero.

4.3.2.2 Ultimate parameters, γ and β

As defined before the parameter γ represents the slope of the ultimate yield envelope. Since the behavior of solder alloys is not affected significantly by confining pressure the ultimate yield envelope can not be plotted as that for soils. Hence it is assumed that the shear strength of the solder alloys is 5% less at zero confining pressure. Thus the ultimate yield envelope can be plotted as shown in Figure 4.11. Values of stress invariants are computed by using the test data presented in Section 5.3.

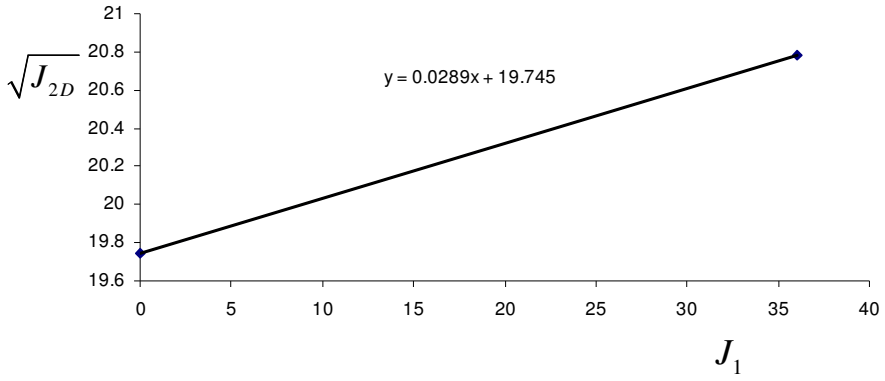

Figure 4.11 Ultimate yield envelope for SAC solder alloy

Parameter β denotes the shape of the yield function in the σ_1-σ_2-σ_3 space. Here it is assumed that the strength of solder alloys is same in all directions and thus the shape of yield function in σ_1-σ_2-σ_3 space can be assumed to be a circle. For this special condition, β is taken as zero.

Temperature variation of both ultimate parameters is assumed to be negligible.

4.3.2.3 Cohesive Strength Intercept, $\bar{c}$

As described before, the cohesive strength $\bar{c}$ is the intercept of the ultimate envelope (Figure 4.3) on the $\sqrt{J_{2D}}$ axis when J_1 = 0. For SAC alloy it is obtained as 19.75. The temperature exponent C for cohesive strength is obtained as -3.2 by following a similar procedure described in 4.3.2.1.

4.3.2.4 Phase change parameter

The phase change parameter for SAC solder alloy is adopted to be 2.1 similar to the SnPb alloy (Whitenack, 2004).

4.3.2.5 Hardening Parameters a_1 and η_1

Procedure for determination of hardening parameters of solder alloys is also same as discussed in section 4.3.1.5. For SAC alloy the hardening parameters a_1 and η_1 at 25^0C are computed as 3.34 x 10^{-7} and 1.6, respectively (Figure 4.12). Temperature exponents for hardening parameters a_1 and η_1 are found to be -2.82 and 0.22, respectively.

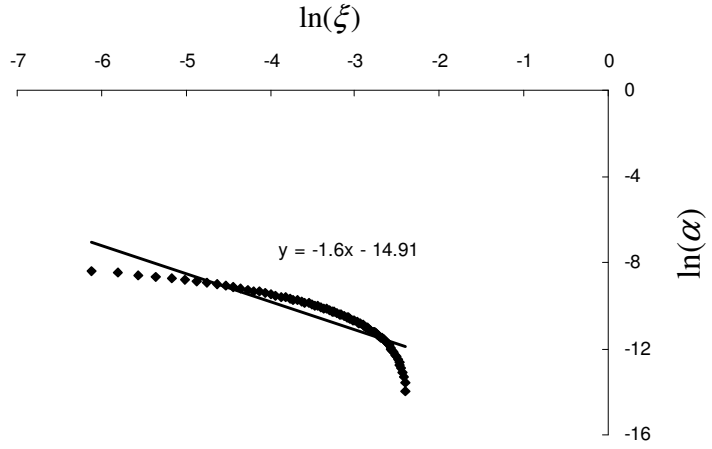

Figure 4.12 Determination of hardening parameters for SAC alloy

4.3.2.6 FA (critical state) parameters.

For the solder alloys the FA state is assumed to carry only hydrostatic stresses. Also the hydrostatic stresses carried by FA parts are assumed to be equal to the RI part (Desai, 2001). Thus there are no additional parameters to be determined for characterizing the FA part.

4.3.2.7 Disturbance Parameters, *A* and *Z*

Disturbance parameter determination procedure for solder alloys is same as described in section 4.3.1.7. For SAC alloy, the average disturbance parameters *A* and *Z* are computed to be 11 and 1, respectively (Figure 4.13).

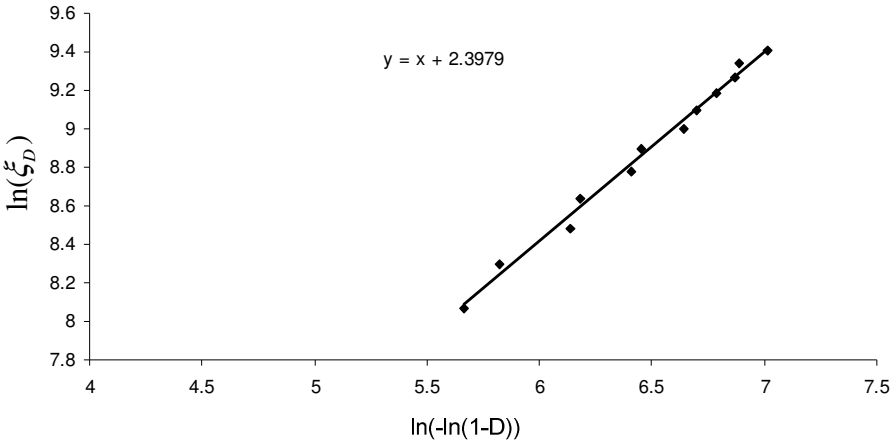

Figure 4.13 Determination of disturbance parameters.

4.3.2.8 Determination of viscous parameters

Solder alloys exhibit a predominant viscoplastic behavior. Thus the viscoelastic part of creep may be neglected. Such an assumption is made for this research and the *evp*

version of the Overlay model is used to characterize the creep response. As discussed in section 3.2.1.1 the yield function needs to be defined by using the static curve. Procedure for constructing the static curve is presented in 3.2.1.2. The procedure to determine the *evp* parameters based on the static yield function is discussed in section 4.3.1.8.1. For SAC alloy the creep parameters Γ and N at 45^0C are computed to be 1.16 x 10^{-9} and 0.4, respectively. Temperature exponents for Γ and N are found to be -12.3 and 4.07, respectively.

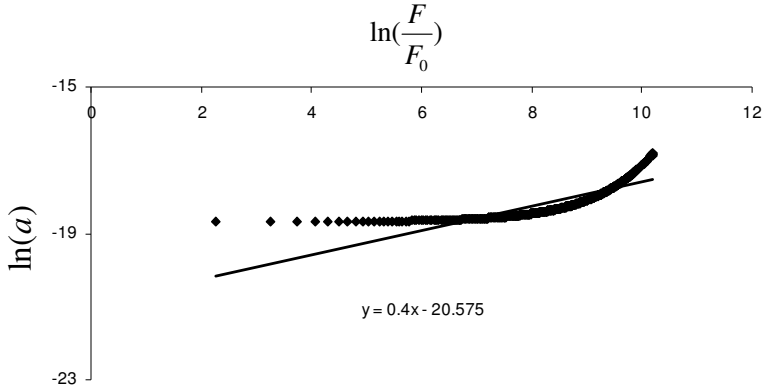

Figure 4.14 Determination of viscous parameters for SAC alloy

Table 4.6 lists the elastoplastic parameters for SAC alloy determined by the using the above procedures. Table 4.7 shows elasto-viscoplastic parameters for the SAC and Sn/Pb alloy determined from the static curves as discussed before.

Table 4.6 Elastoplastic parameters for SAC alloy

Parameter	SAC alloy	Temperature
Elastic		
E (MPa)	40000	-1.09
ν	0.3474	0
Plastic –		
γ	0.000835	0
β	0	0
n	2.1	0
$\overline{c}$	19.75	-3.2
Hardening		
a_1	3.34×10^{-7}	-2.82
η_1	1.6	0.22
Disturbance		
D_u	1	0
A	0.6	0
Z	0.1	0

Table 4.7 Elasto-viscoplastic (static) parameters for SAC and Sn/Pb alloys

	SAC alloy		Sn/Pb alloy (63Sn37Pb)	
	Parameter	**Temperature**	**Parameter**	**Temperature**
Elastic				
E (MPa)	2343	-1.12	1874	-0.87
ν	0.3474	0	0.4	0
Plastic				
γ	0.000835	0	0.00082	0
β	0	0	0	0
n	2.1	0	2.1	0
$\overline{c}$	5.28	-3.2	5.87	-2.2
Hardening				
a_1	6×10^{-8}	-3.1	3.73×10^{-6}	-2.6
η_1	2.5	0.2	0.78	0.3
Disturbance				
D_u	1	0	1	0
A	11	0	1	0
Z	1	0	0.6531	0
Creep				
Γ	1.16×10^{-9}	-12.3	3×10^{-8}	-10.4
N	0.4	4.7	0.8	5.1

CHAPTER 5

APPLICATION of DSC to LEAD FREE SOLDERS

5.1 Background

Use of lead is considered to be potentially harmful to environment owing to its toxic properties (Tummala and Rymaszewski, 1989). Environmental agencies such as Restriction of Hazardous Substances (RoHS) and European Union (EU) have posed a ban on use of lead in electronic packages in effect from august 2006 (Dongkai, 2006). The electronic industry in the recent years is thus undergoing a transition from leaded materials to lead free ones. Different substitutes for the Sn/Pb (63Sn-37Pb) alloy, which has been widely used as a solder joint material, are being considered. Some examples of such tin based substitutes are Sn/Ag, Sn/Cu Sn/Ag/Cu. Among these alloys Sn/3.9Ag/0.6Cu (SAC) is considered to be the closest substitute based on various factors (Dongkai, 2006).

The elastoplastic DSC/HISS model has been successfully applied to characterize the behavior of Sn/Pb eutectic solder alloy by Whitenack (2004). Current work focuses on such characterization of the SAC alloy and extends it to model the creep effects in Sn/Pb and SAC alloys using the elasto-viscoplastic (*evp* – Chapter 3) model. Following section describes the thermal fatigue phenomenon in solder alloys and identifies specific research goals.

5.2 Problem description

Solder joints in an electronic package perform three primary functions

a. Carry electric current

b. Carry away the heat dissipated by the chip.

c. Provide structural support to the chip.

Figure 5.1 shows a schematic of a solder joint. It is composed of three materials having different coefficients of thermal expansion (CTE). Table 5.1 shows CTE values for silicon, Sn/Pb eutectic solder and Copper (typical substrate material). It is evident that the thermal mismatch exists at the joint. It leads to thermal stresses at the joint. Upon application of temperature cycles during operation, the solder joint undergoes thermal fatigue and softening leading to subsequent failure. Figure 5.2 shows photomicrographs of typical solder joint failures (Syed, 2001). It can be observed that the microcracks leading to open cracks initiate and propagate mainly along the chip-solder interface. An open crack or several microcracks at the chip-solder interface may increase the electrical resistivity of the joint. This affects the processing speed and performance of the package.

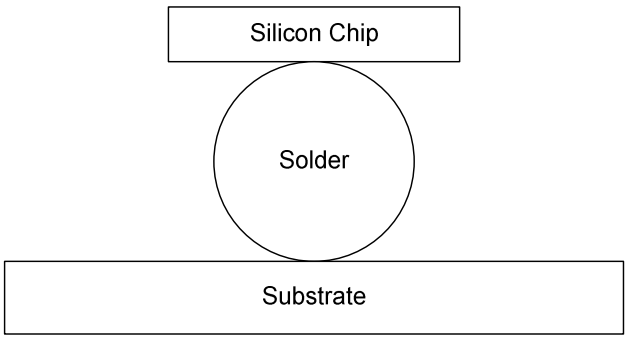

Figure 5.1 Schematic of the solder joint in an electronic package

Properties of the solder alloy thus play an important role in deciding the life of the joint. Hence it is critical to understand the behavior of the solder alloy under cyclic thermal and mechanical loads.

Table 5.1 Coefficients of thermal expansion for the materials forming the solder joint (Tummala and Rymaszewski, 1989)

Material	**CTE (ppm/ ^{0}C)**
Silicon	2.8
Solder alloys	21 – 27
Copper (Substrate)	16

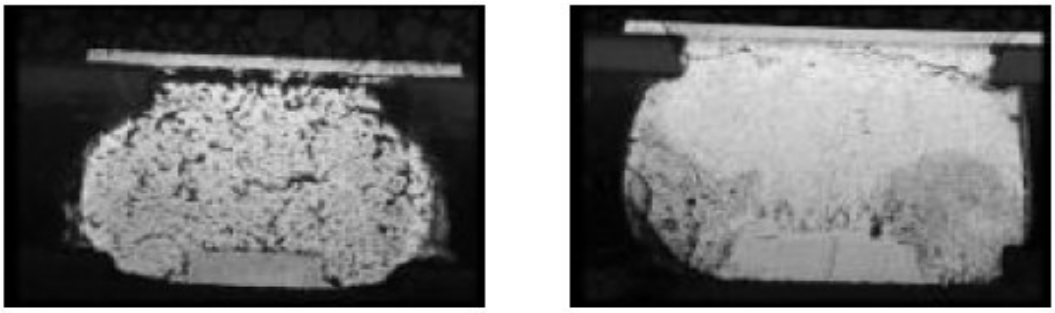

(a) Sn/Pb alloy (b) SAC alloy

Figure 5.2 Typical Solder Joint Failures for (a) Sn/Pb and (b) SAC alloys (Syed, 2001)

Following is a list of specific research objectives for this problem

8. Conduct literature review for following test data
    - Stress-strain tests for SAC alloy.
    - Creep tests on SAC alloy.
    - Cyclic tests on SAC alloy.

- Creep tests on Sn/Pb alloy.

9. Determine material parameters for both alloys (SAC and Sn/Pb) to calibrate the DSC/HISS and creep models. (Note: Elastoplastic parameters for Sn/Pb alloy are determined by Whitenack (2004), In the current work the static and creep parameters for Sn/Pb alloy are also determined)
10. Perform validations of the elastoplastic and elasto-viscoplastic models based on the laboratory test data.
11. Perform thermomechanical fatigue analysis of an electronic package using finite element analysis.
12. Develop a failure criterion based on the analysis results and available test data
13. Compare predicted and observed results based on the failure criterion developed.
14. Apply the proposed rate dependent model (Section 3.4) to predict behavior of the SAC alloy and perform validations.

5.3 Test data from Literature

Calibration of the DSC model involves determination of material parameters from various types of tests on the material. Table 5.2 lists different types of tests and the purpose of each test towards model calibration.

A comprehensive literature review is conducted to find the experimental data for SAC and Sn/Pb alloys for types of tests mentioned in Table 5.2. The test data used for finding parameters is given in following sections.

5.3.1 Stress – Strain tests for SAC alloy

Temperature dependent stress-strain test data for SAC alloy is adopted from Vianco et al (2003). Figure 5.3 shows this data at five different temperatures. Test procedures, sample preparation and other details are discussed in Vianco (2003).

Table 5.2 Different types of tests and their purpose in DSC model calibration

Type of Test	Purpose	Parameters obtained
Tension or compression (stress-strain) tests	To find elastic parameters To find parameters in HISS model.	E, ν $\gamma, \beta, n, \bar{c}, a_1, \eta_1$
Creep tests.	To construct the static curve To find creep parameters.	Γ, N
Cyclic tests.	To find disturbance parameters	A, Z

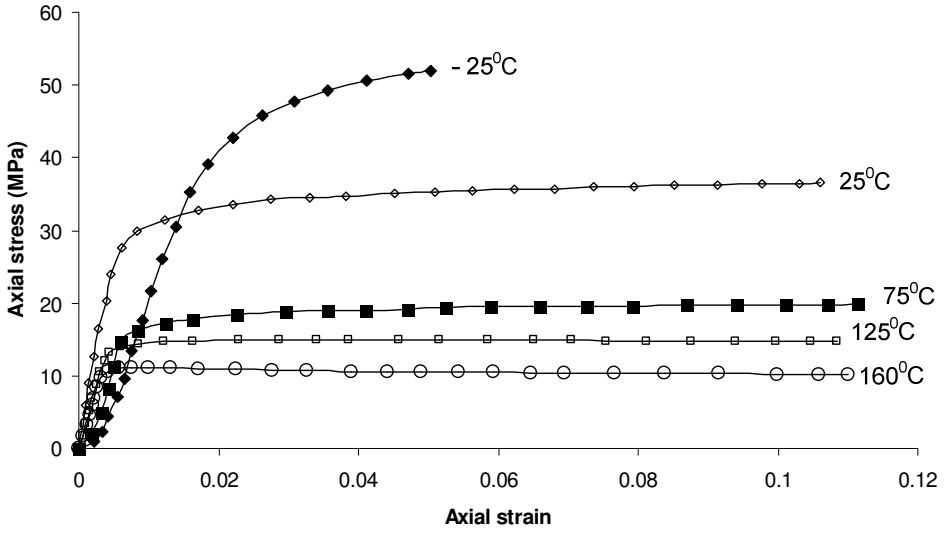

Figure 5.3 Stress–strain test results on SAC alloy used for DSC model calibration at various temperatures (Vianco et al, 2003).

5.3.2 Creep test data

Due to high operating temperature of solder alloys, creep deformation plays an important role in overall material response. This section presents temperature dependent creep test data for SAC and Sn/Pb alloys. This data for both materials is adopted from Xiao and Armstrong (2004).

5.3.2.1 Creep test data for SAC alloy

Figures 5.4 (a-d) show results of creep tests on SAC alloy at four different temperatures. At each temperature various constant axial stresses are applied to the material specimen to obtain various creep curves. Test procedures and other details are given in Xiao and Armstrong (2004). Figure 5.4 (e) shows static curves based on these creep tests as described in Section 3.2.2.2.

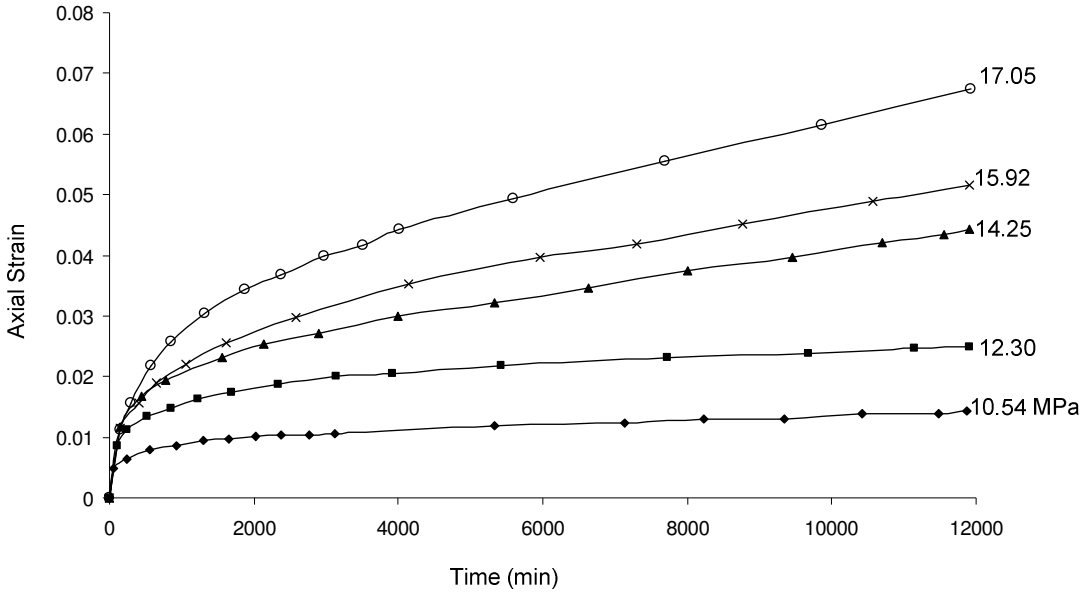

(a) 45^0C

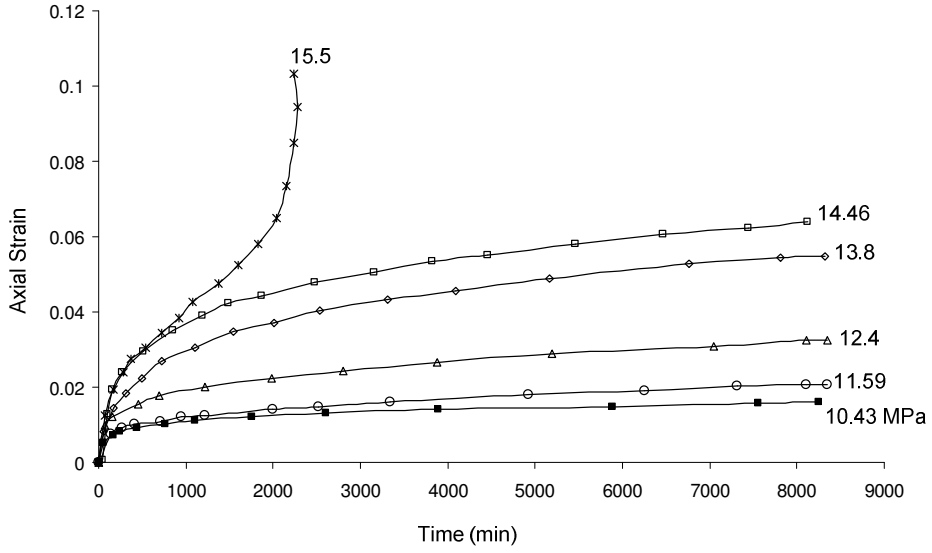

(b) 80^0C

Figure 5.4. Creep test results on SAC alloy at (a) 45^0C (b) 80^0C (c) 115^0C (d) 150^0C (Xiao et al, 2004).

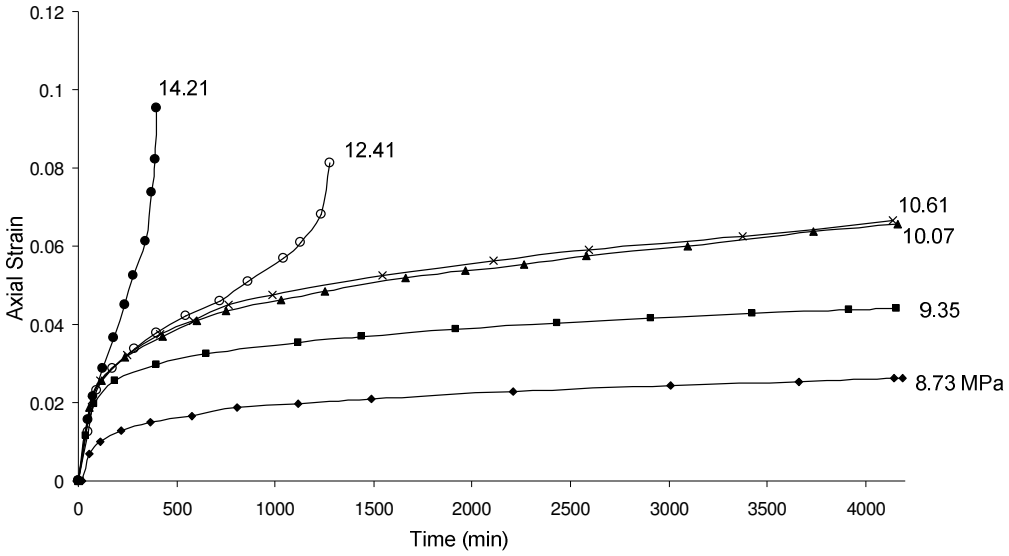

(c) 115^0C

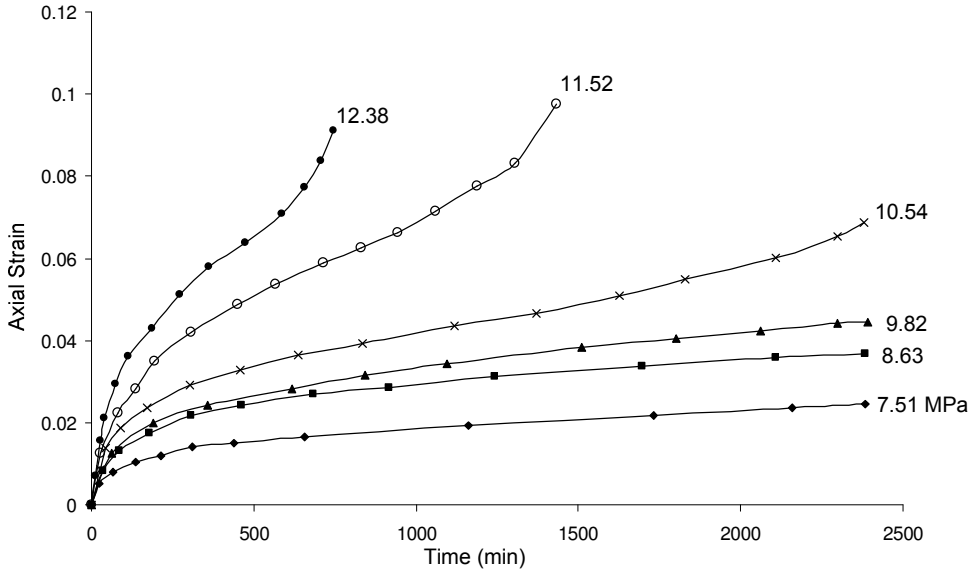

(d) 150^0C

Figure 5.4 (Continued) Creep test results on SAC alloy at (a) 45^0C (b) 80^0C (c) 115^0C (d) 150^0C (Xiao and Armstrong, 2004).

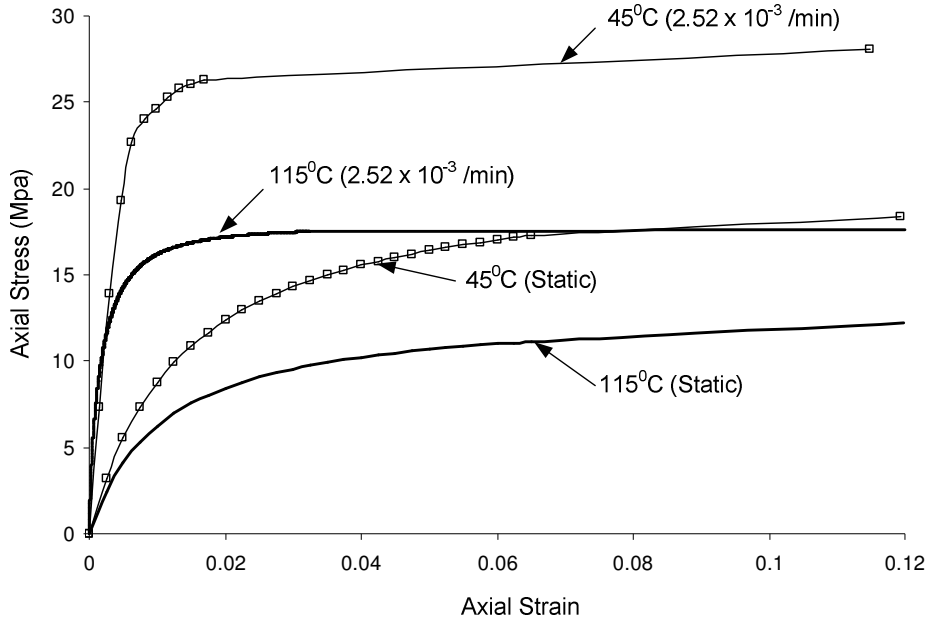

(e) Static curves constructed from creep test results for SAC alloy at 45 and 115^{0}C.

Figure 5.4 (continued)

Creep parameters are determined from these tests results for calibration of the *evp* model (Section 3.3). Creep tests at 45^{0}C and 115^{0}C are used to construct the static curves for the SAC alloy (Figure 5.4 (e)).

5.3.2.2 Creep test data for Sn/Pb alloy

Creep test data for Sn/Pb alloy is also adopted from Xiao and Armstrong (2004) as for the SAC alloy. Figures 5.5 (a-c) show the test curves at various temperatures. Constructed static curves for SnPb alloy at 25^{0}C and 45^{0}C are shown in Figure 5.5 (d)

It must be noted that some of the test results show catastrophic or tertiary creep. For example creep curve for SAC alloy at 80^{0}C (Figure 5.4b) and 15.5 MPa of constant

applied stress shows tertiary creep. Such curves are not used for parameter determination since the formulation of the *evp* model is based on the secondary creep.

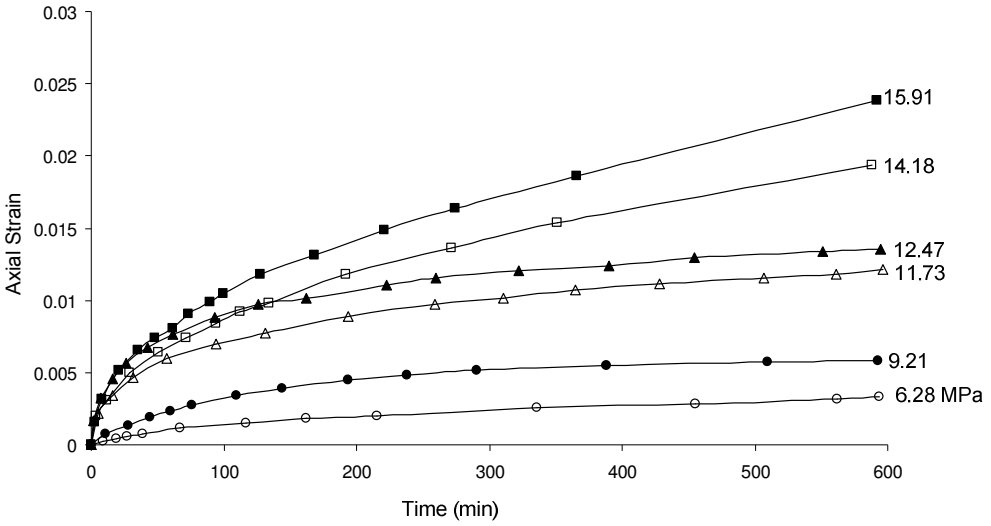

(a) 25^0C

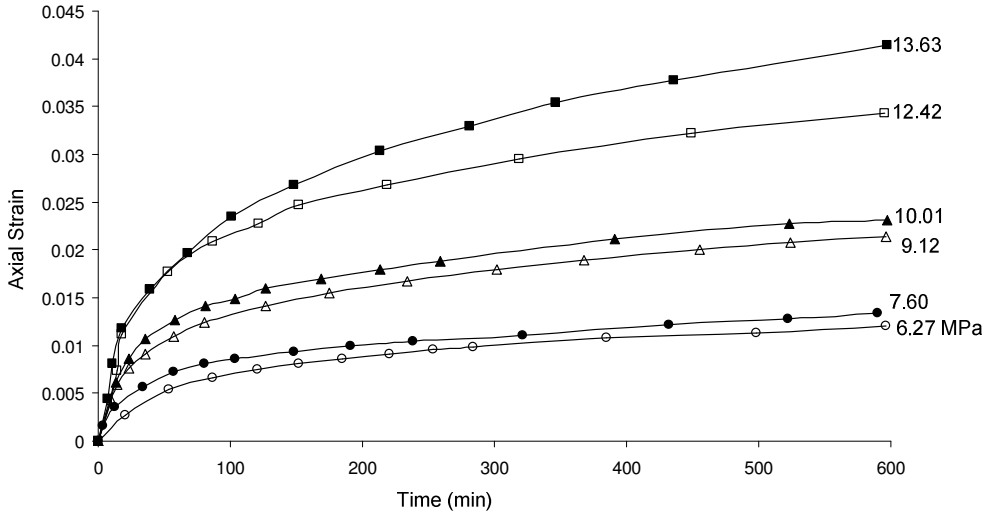

(b) 45^0C

Figure 5.5 Typical Creep curves for Sn/Pb eutectic alloy at (a) 25^0C (b) 45^0C and (c) 80^0C. (Xiao and Armstrong, 2004) (d) Constructed static curves

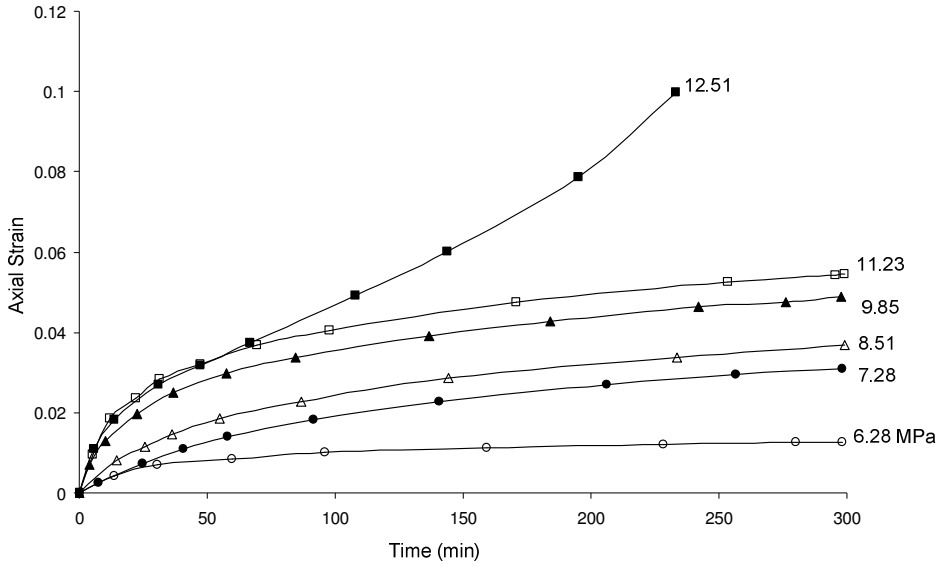

(c) 80^0C

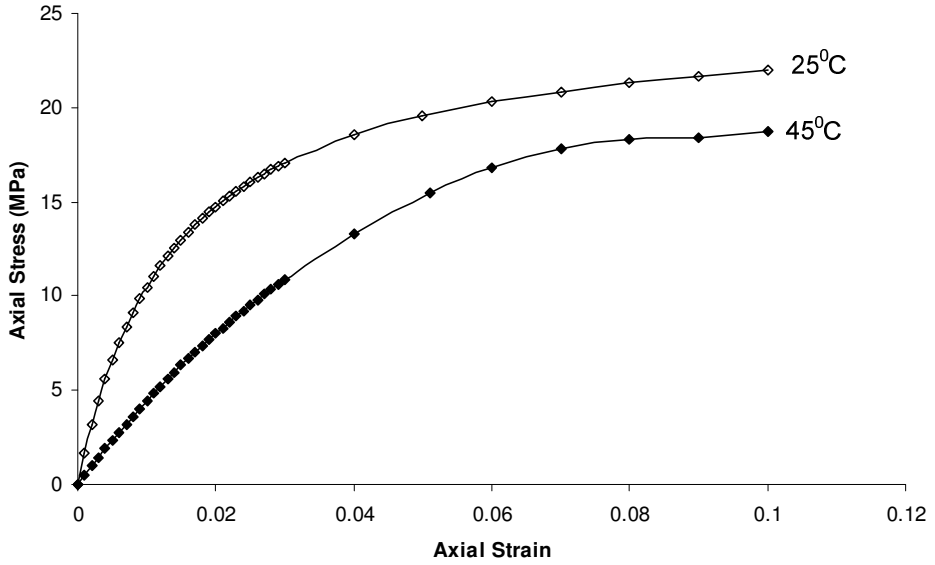

(d) Static curves constructed from creep tests for SnPb alloy at 25 and 45^0C

Figure 5.5 (Continued)

5.3.3 Cyclic test data

As discussed before the solder joint in a package undergoes several temperature cycles leading to failure. Thus in order to accurately predict the behavior of the joint it is critical to understand the behavior of the alloy under cyclic loading. Cyclic test results are used represent the material degradation, which is modeled by using the disturbance function in the DSC. Figure 5.6 shows the cyclic test data for SAC alloy adopted from Zeng et al (2005).

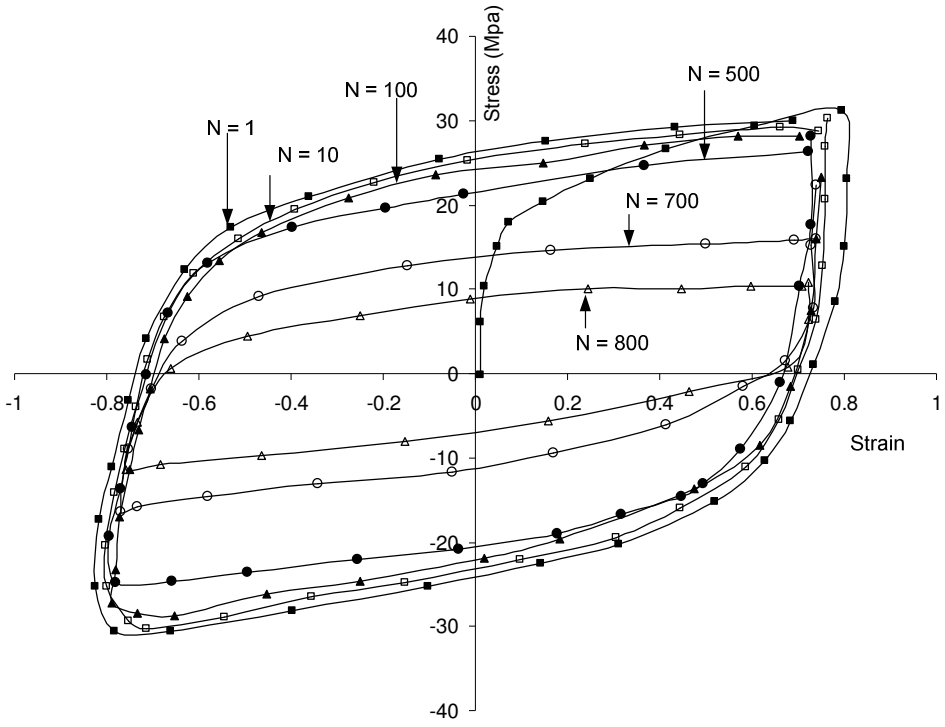

Figure 5.6 Cyclic test data for SAC alloy (Zeng et al, 2005)

5.4 Material Parameters

Based on the above test data the DSC model parameters are determined using the procedures described in Chapter 4. Two types of parameters are required for SAC and Sn/Pb alloys

1. Elastoplastic parameters.

2. Elasto-viscoplastic parameters.

Table 5.3 gives the elastoplastic material parameters for SAC alloy. These parameters are used to conduct the specimen level validations presented in section 5.5.1

Table 5.3. Elastoplastic model parameters for SAC alloy

Parameter	**SAC alloy**	**Temperature Exponent (C)**
Elastic		
E (MPa)	40000	-1.09
ν	0.3474	0
Plastic –		
γ	0.000835	0
β	0	0
n	2.1	0
$\overline{c}$	19.75	-3.2
Hardening		
a_1	3.34×10^{-7}	-2.82
η_1	1.6	0.22
Disturbance		
D_u	1	0
A	0.6	0
Z	0.1	0

Table 5.4 lists the elasto-viscoplastic parameters for SAC and Sn/Pb alloys. These parameters are determined from the constructed static curves. These are used to validate the evp model (section 5.5.2.1 and 5.5.2.2) and also for the boundary value problem (section 5.5.3)

Table 5.4 Parameters for elasto-viscoplastic model

	SAC alloy		Sn/Pb alloy	
	Parameter	**Temperature Exponent (C)**	**Parameter**	**Temperature Exponent (C)**
Elastic				
E (MPa)	2343	-1.12	1874	-0.87
ν	0.3474	0	0.4	0
Plastic				
γ	0.000835	0	0.00082	0
β	0	0	0	0
n	2.1	0	2.1	0
$\overline{c}$	5.28	-3.2	5.87	-2.2
Hardening				
a_1	6×10^{-8}	-3.1	3.73×10^{-6}	-2.6
η_1	2.5	0.2	0.78	0.3
Disturbance				
D_u	1	0	1	0
A	11	0	1	0
Z	1	0	0.6531	0
Creep				
Γ	1.16×10^{-9}	-12.3	3×10^{-8}	-10.4
N	0.4	4.7	0.8	5.1

5.5 Validation

DSC model validation for elastoplastic and elasto-viscoplastic models is presented in this section. In general the validation process is divided into three levels.

- Level 1 – Prediction of test data used to compute the parameters.
- Level 2 – Prediction of test data not used for parameter determination (independent validation)
- Level 3 – Comparison of predicted and observed behavior in a boundary value problem (BVP) for BGA package failure using DSC model implemented in the finite element analysis program.

Table 5.5 shows different validation steps performed in the current work and the section number in which the detailed procedures are presented.

Table 5.5 Different validations performed in the present work

Solder Alloy	**Validation of**		
	elastoplastic model (Level 1 and 2)	**elasto-viscoplastic model (Level 1 and 2)**	**BVP with creep**
SAC	Section 5.5.1	Section 5.5.2.1	Section 5.5.3
Sn/Pb	Desai et al (2004); Wang (2002)	Section 5.5.2.2	Section 5.5.3

5.5.1 Level 1 and Level 2 Validations of Elastoplastic model (No Creep)

Level 1 and 2 predictions are carried out using the FEM analysis. DSC-SST2D (Desai, 1999) program is used for the analysis. The tensile stress-strain test described in Vianco et al (2003) is simulated using the FE procedure. Geometry of the test specimen used is same as that used by Vianco et al (2003) and is shown in Figure 5.7. Plane stress idealization is used for the analysis. Figure 5.7 also shows the FEM mesh used along with geometry, loading and the boundary conditions.

Parameters at different temperatures are used to backpredict the test data. For the current work, material parameters are calculated based on the test data at 25, 75 and$160^{\circ}C$. Thus Level 1 predictions are performed based on these parameters. Level 2 (independent) predictions are performed for test at 125^{0}C.

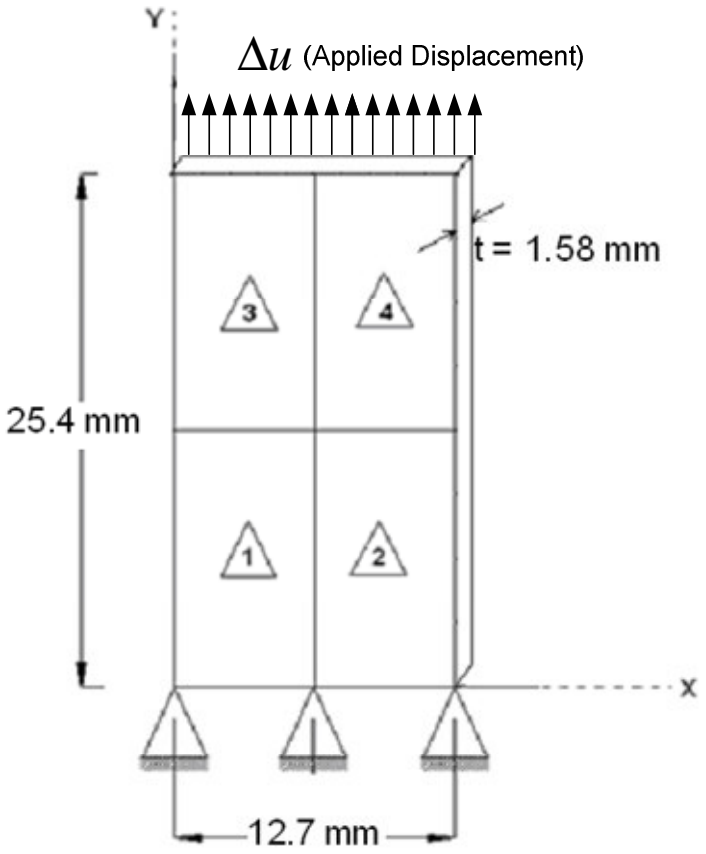

Figure 5.7 Geometry, mesh and boundary conditions for the FEM analysis.

Material parameters used for these validations are listed in Table 5.3. Typical results of Level 1 and Level 2 validations are shown in Figure 5.8 and 5.9, respectively.

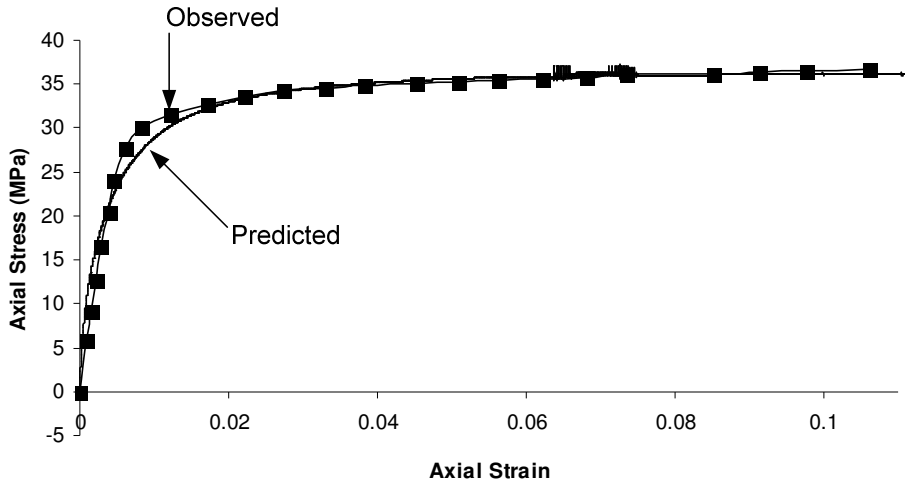

(a) 25^0C

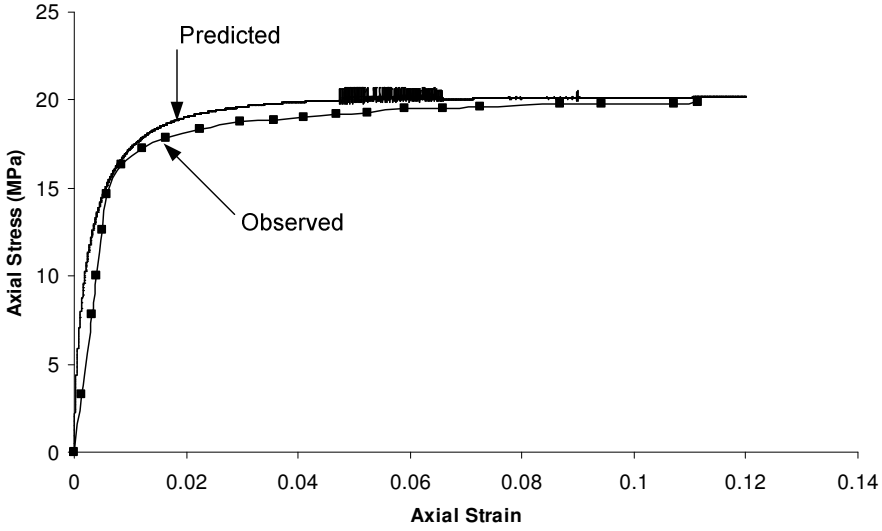

(b) 75^0C

Figure 5.8 Level 1 validation of elastoplastic model for SAC alloy

(Predicted curves show erratic results near the peak stress due to numerical instability. This can be corrected by increasing the maximum number of iterations for convergence)

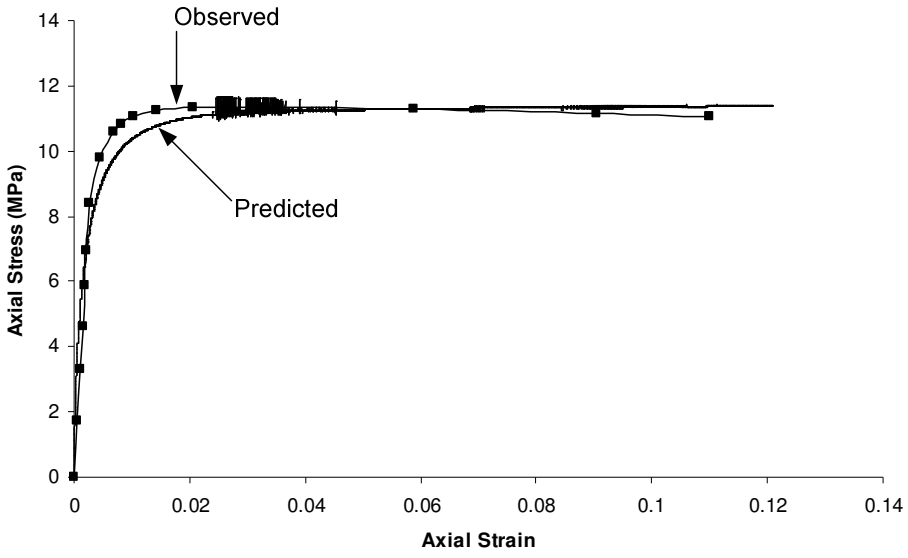

(c) 160^0C

Figure 5.8 (continued) Level 1 validation of elastoplastic model for SAC alloy

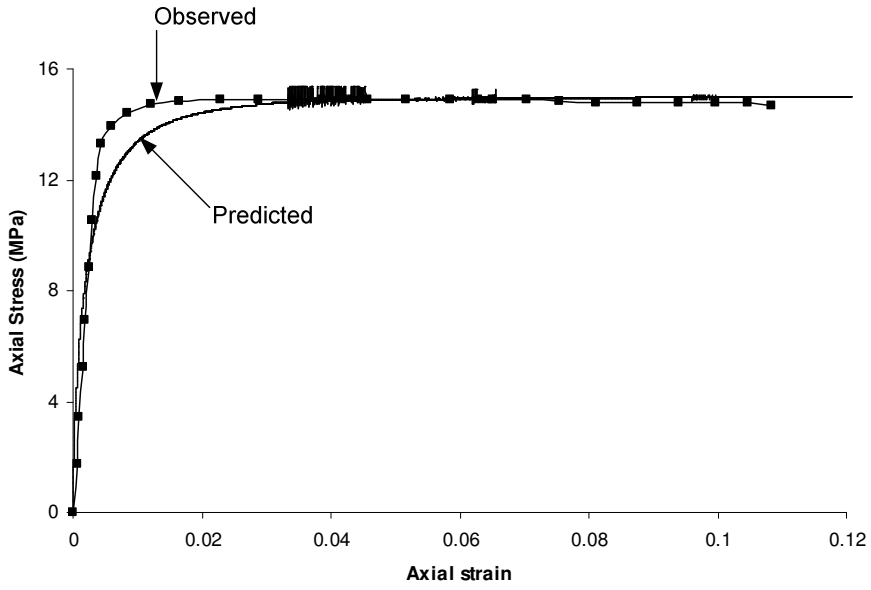

(a) 125^0C

Figure 5.9 Level 2 (Independent) validation of elastoplastic model for SAC alloy

(Predicted curves show erratic results near the peak stress due to numerical instability. This can be corrected by increasing the maximum number of iterations for convergence)

5.5.2 Validation of elasto-viscoplastic (creep) model (Level 1 and 2)

Elasto-viscoplastic model is validated by following a similar procedure as described in previous section. Same mesh and boundary conditions are used for predictions however the loading used is different as shown in Figure 5.10. The constant axial stress is applied in one step and then held constant over time. The predictions are performed using the parameters computed based on the static curve (Table 5.4).

Comparison of the predicted and observed curves is shown in Figure 5.11. It can be seen that the predicted curves are in good agreement with the test curves. This indicates that the MDSC model can be used to successfully characterize the creep behavior of SAC lead free alloy.

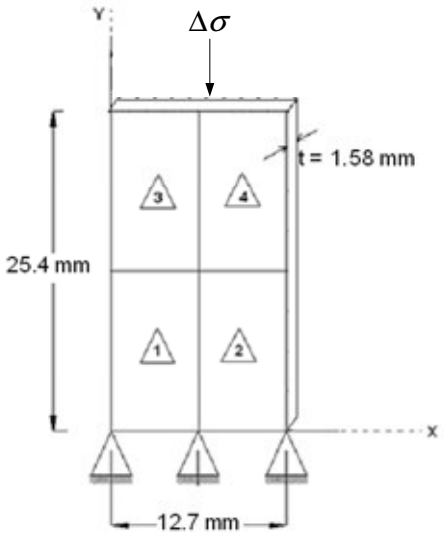

Figure 5.10 FEA mesh, boundary conditions and loading used for validation of elasto-viscoplastic model.

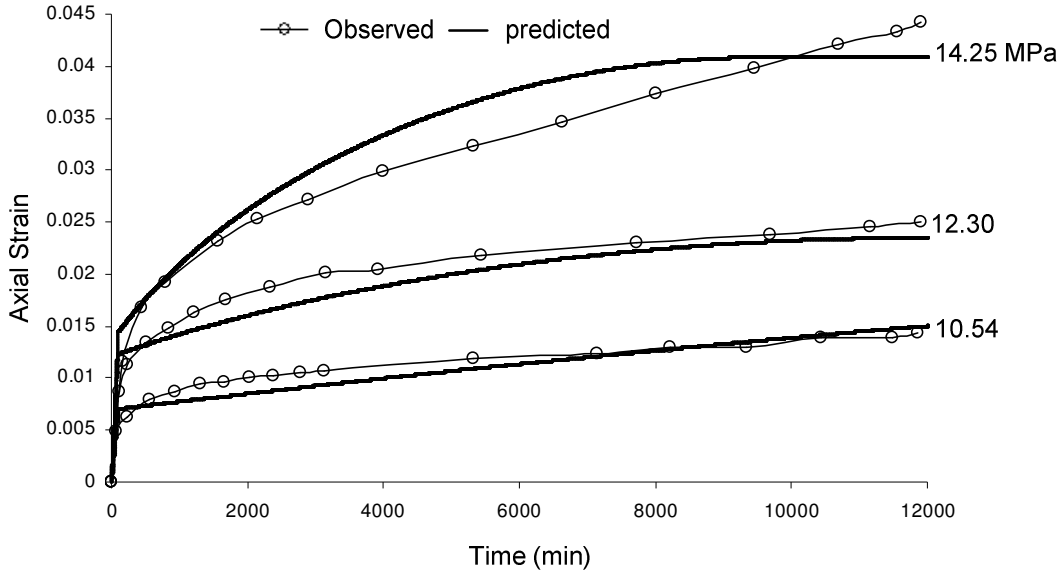

(a) 45^0C (Level 1)

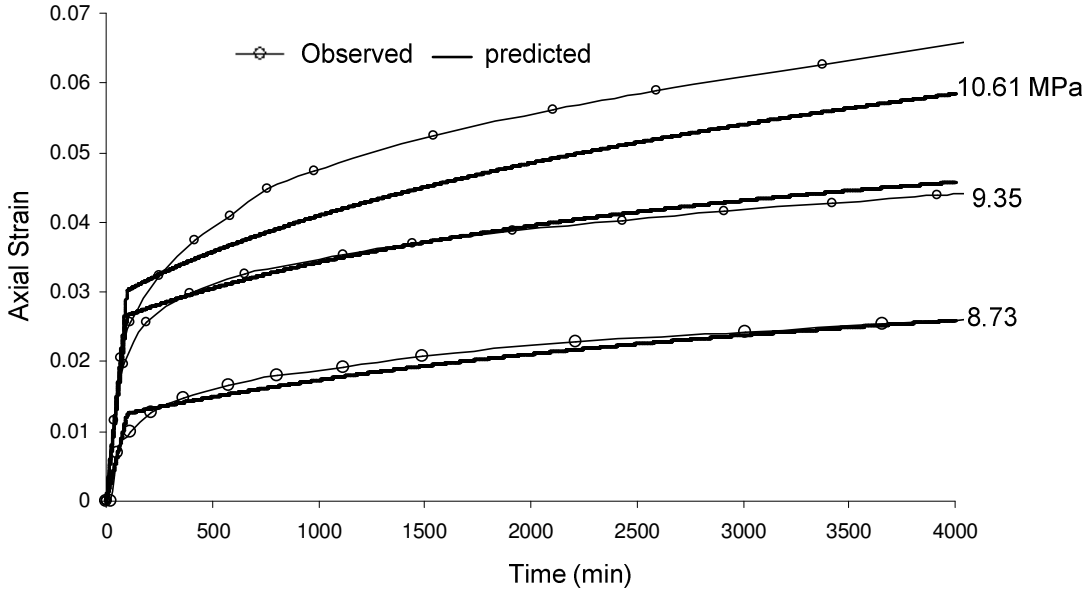

(b) 115^0C (Level 1)

Figure 5.11 Validation of creep model (a) 45^0C (b) 115^0C (c) 80^0C (Level 2)

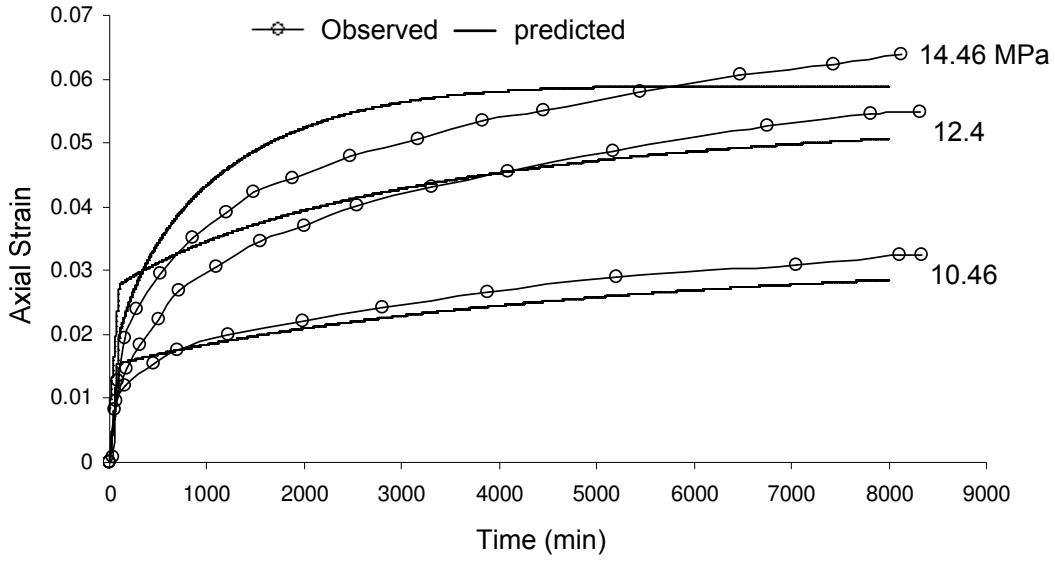

(c) 80^0C (Independent)

Figure 5.11 Validation of creep model (a) 45^0C (b) 115^0C (c) 80^0C (Level 2)

Figure 5.12 shows validation of creep model for Sn/Pb alloy at Level 1 and Level 2. The *evp* model parameters and static parameters used for these validations are listed in Table 5.4.

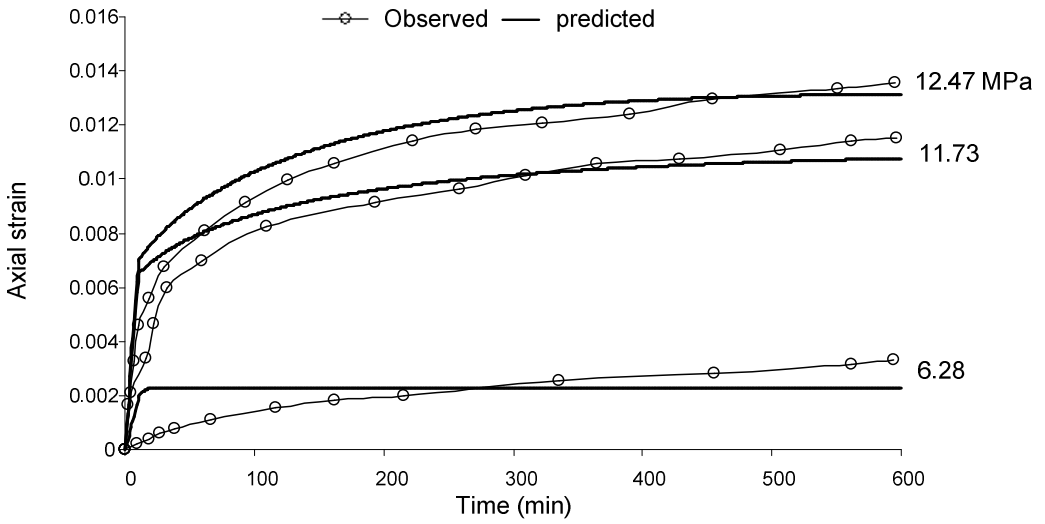

(a) 25^0C (Level 1)

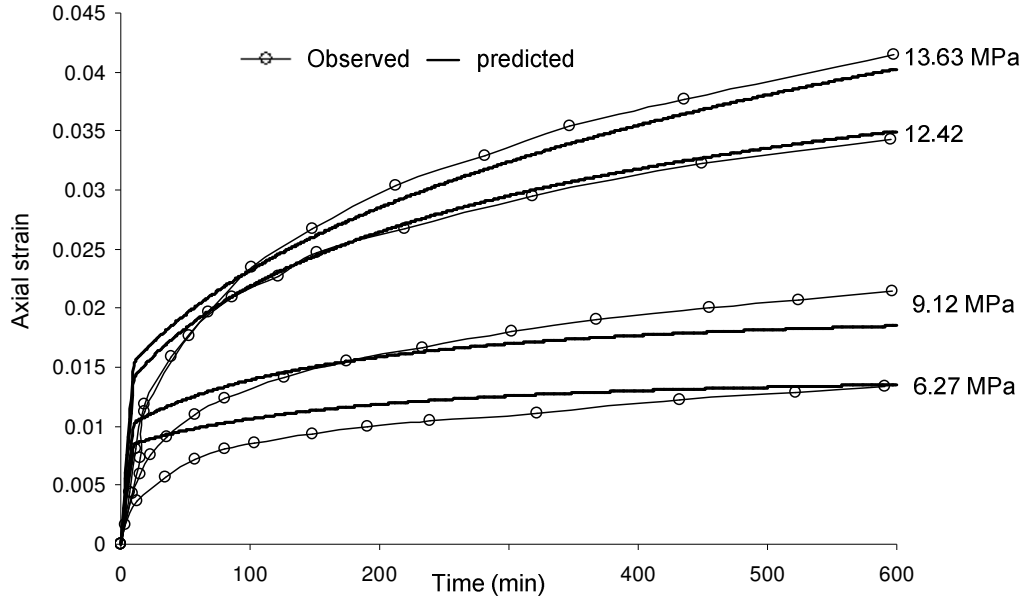

(b) 45^0C (Level 1)

Figure 5.12 Validation of *evp* model for Sn/Pb alloy (a) 25^0C (b) 45^0C (c) 80^0C (Level 2)

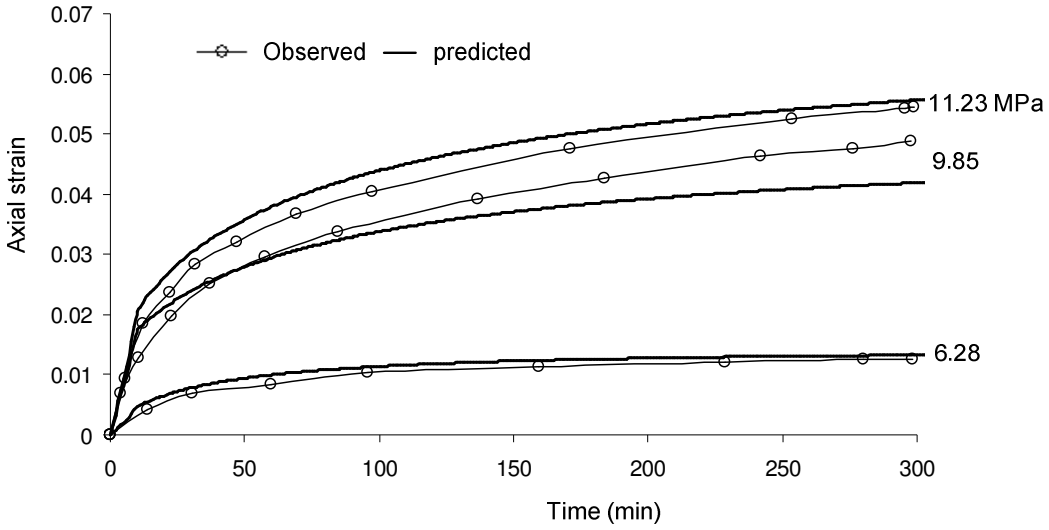

(c) 80^0C (Independent)

Figure 5.12 (continued) Validation of *evp* model for Sn/Pb alloy

5.5.3 Simulation of a Boundary Value Problem

This step is treated as Level 3 validation of the model. Thermal fatigue analysis of BGA 225 package using the DSC model is discussed here. Schematic of the BGA 225 package is shown in Figure 5.13. The corner ball in the array (Figure 5.13) is considered to be the critical solder ball (Whitenack, 2004). The critical ball is then characterized using the DSC model under thermomechanical loading to predict the number of cycles to failure. DSC model prediction is compared with results of actual tests conducted at Boeing (Rassaian and Lee, 2007).

5.5.3.1 Test Results

Thermal cycling tests on BGA 225 packages are conducted at Boeing. Some tests are performed using SAC alloy as the solder joint material while in other tests Sn/Pb

eutectic alloy is used. Two different loading conditions are used. The test results are given in Table 5.6.

Table 5.6: Test data for number of cycles to failure on BGA 225 package (Rassaian and Lee, 2007)

Solder	Temperature cycling between	Mean cycles to failure
SAC	-55 to 125^0C	3248
Sn/Pb	-55 to 125^0C	2679
Sn/Pb	-20 to 80^0C	7447

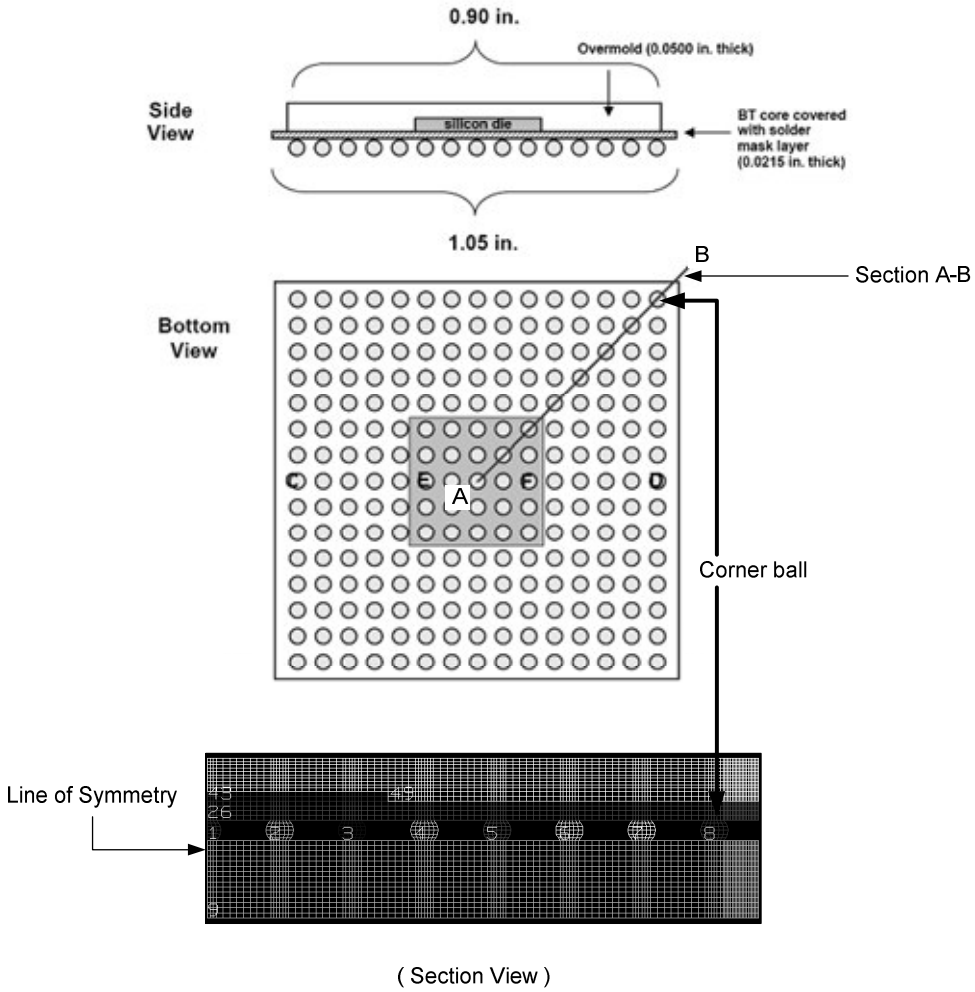

Figure 5.13 Schematic of the BGA 225 package (Rassaian and Lee, 2007)

Three analyses are performed using properties of two solder alloys under two different loading conditions as shown in Table 5.7. For convenience each analysis is referred by a short name as listed in Table 5.7.

Table 5.7: Different analyses used for validation

Solder alloy	Temperature cycling between	Short name
SAC	-55 to 125^0C	SAC_1
Sn/Pb	-55 to 125^0C	SnPb_1
Sn/Pb	-20 to 80^0C	SnPb_2

Following sections discuss various details of the analysis procedure.

5.5.3.2 Mesh

The mesh details given here are common for the three analyses listed in Table 5.7. Four node quadrilateral elements are used. A FEM mesh consisting of 360 elements and 399 nodes used in the current analyses is shown in Figure 5.12. Nodal co-ordinates and element connectivity is generated by Boeing using LS-MAZE preprocessor (Rassaian and Lee, 2007).

Whitenack (2004) successfully analyzed 313 PBGA package under similar loading conditions using 2D plane stress idealization. Thus the current analysis is also based on the same assumption.

5.5.3.3 Boundary conditions (Applied displacements):

When temperature cycles are applied to the solder joint the top and bottom interfaces of the solder ball experience thermal displacements. These displacements

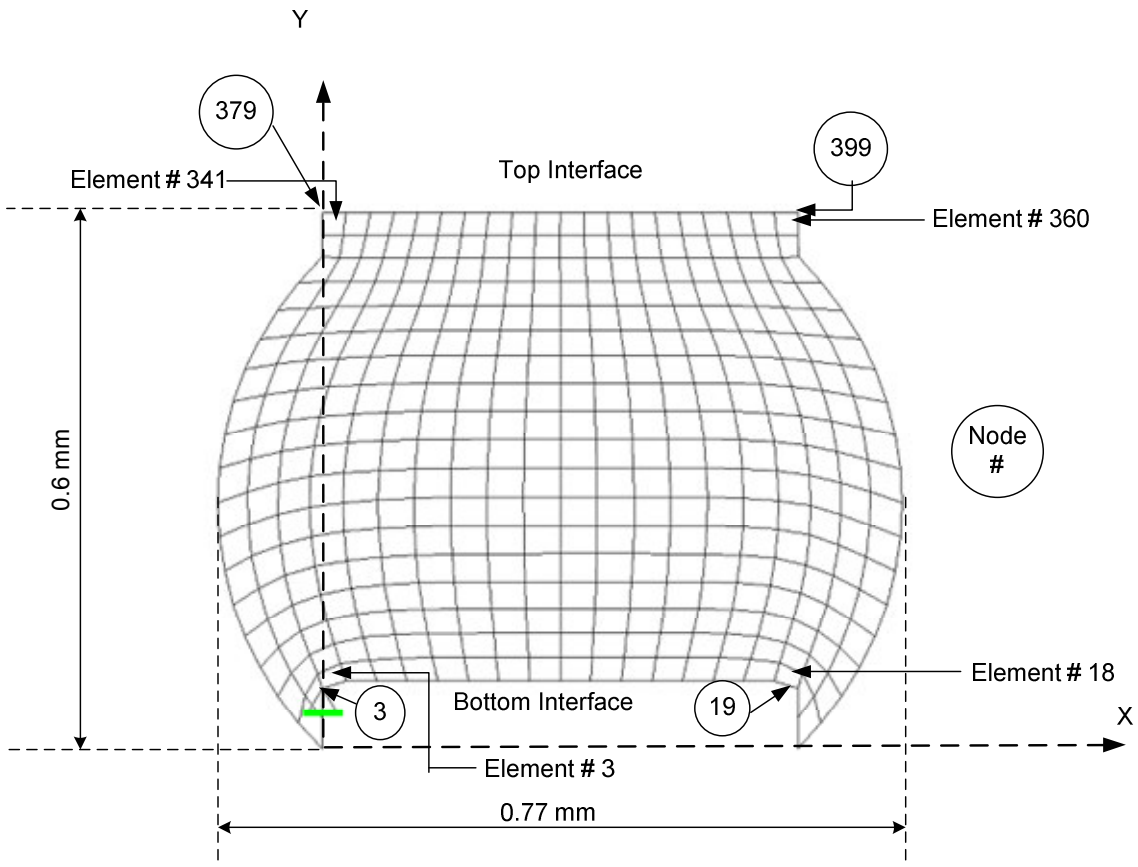

Figure 5.14 Geometry, FEM mesh and nodal fixity for critical solder ball

are computed by performing a 2D FEM analysis of the diagonal section A-B (Figure 5.11) . This analysis is referred as global analysis. It is performed at Boeing using Nike-2D software by assuming that the solder joint material is linear elastic. Node No 3 is assumed to be fixed in both X and Y directions, and absolute nodal displacements obtained from the global analysis are converted to displacements relative to Node no. 3. Nodes 1,2,20 and 21 near the bottom interface are free in both X and Y directions.

Table 5.8 Applied relative displacements (Rassaian and Lee, 2007)

	SAC_1		SnPb_1		SnPb_2	
Node #	X Disp (in)	Y Disp (in)	X Disp (in)	Y Disp (in)	X Disp (in)	Y Disp (in)
4	3.48E-06	1.62E-06	2.24E-06	9.23E-07	1.99E-06	9.23E-07
5	6.96E-06	3.23E-06	4.48E-06	1.85E-06	3.98E-06	1.85E-06
6	1.04E-05	4.85E-06	6.72E-06	2.77E-06	5.96E-06	2.77E-06
7	1.39E-05	6.46E-06	8.97E-06	3.69E-06	7.95E-06	3.69E-06
8	1.74E-05	8.08E-06	1.12E-05	4.62E-06	9.94E-06	4.61E-06
9	2.09E-05	9.69E-06	1.34E-05	5.54E-06	1.19E-05	5.54E-06
10	2.44E-05	1.13E-05	1.57E-05	6.46E-06	1.39E-05	6.46E-06
11	2.78E-05	1.29E-05	1.79E-05	7.39E-06	1.59E-05	7.38E-06
12	3.13E-05	1.45E-05	2.02E-05	8.31E-06	1.79E-05	8.31E-06
13	3.48E-05	1.62E-05	2.24E-05	9.23E-06	1.99E-05	9.23E-06
14	3.83E-05	1.78E-05	2.47E-05	1.02E-05	2.19E-05	1.02E-05
15	4.18E-05	1.94E-05	2.69E-05	1.11E-05	2.39E-05	1.11E-05
16	4.52E-05	2.10E-05	2.91E-05	1.20E-05	2.58E-05	1.20E-05
17	4.87E-05	2.26E-05	3.14E-05	1.29E-05	2.78E-05	1.29E-05
18	5.22E-05	2.42E-05	3.36E-05	1.39E-05	2.98E-05	1.38E-05
19	5.57E-05	2.58E-05	3.59E-05	1.48E-05	3.18E-05	1.48E-05
399	-2.82E-05	9.15E-05	-1.45E-05	7.31E-05	-1.61E-05	5.23E-05
398	-2.57E-05	9.30E-05	-1.29E-05	7.40E-05	-1.47E-05	5.31E-05
397	-2.32E-05	9.44E-05	-1.14E-05	7.49E-05	-1.32E-05	5.39E-05
396	-2.07E-05	9.58E-05	-9.88E-06	7.57E-05	-1.18E-05	5.48E-05
395	-1.81E-05	9.73E-05	-8.34E-06	7.66E-05	-1.04E-05	5.56E-05
394	-1.56E-05	9.87E-05	-6.81E-06	7.74E-05	-8.93E-06	5.64E-05
393	-1.31E-05	0.0001	-5.27E-06	7.83E-05	-7.49E-06	5.72E-05
392	-1.06E-05	0.000102	-3.74E-06	7.92E-05	-6.06E-06	5.81E-05
391	-8.09E-06	0.000103	-2.20E-06	8.00E-05	-4.62E-06	5.89E-05
390	-5.58E-06	0.000104	-6.69E-07	8.09E-05	-3.19E-06	5.97E-05
389	-3.07E-06	0.000106	8.65E-07	8.17E-05	-1.75E-06	6.05E-05
388	-5.57E-07	0.000107	2.40E-06	8.26E-05	-3.18E-07	6.14E-05
387	1.95E-06	0.000109	3.93E-06	8.35E-05	1.12E-06	6.22E-05
386	4.47E-06	0.00011	5.47E-06	8.43E-05	2.55E-06	6.30E-05
385	6.98E-06	0.000112	7.00E-06	8.52E-05	3.99E-06	6.38E-05
384	9.49E-06	0.000113	8.54E-06	8.61E-05	5.42E-06	6.46E-05
383	1.20E-05	0.000115	1.01E-05	8.69E-05	6.86E-06	6.55E-05
382	1.45E-05	0.000116	1.16E-05	8.78E-05	8.29E-06	6.63E-05
381	1.70E-05	0.000117	1.31E-05	8.86E-05	9.73E-06	6.71E-05
380	1.95E-05	0.000119	1.47E-05	8.95E-05	1.12E-05	6.79E-05
379	2.2E-05	0.00012	1.62E-05	9.04E-05	1.26E-05	6.88E-05

Computation of relative displacements is accomplished at Boeing using procedures described in Whitenack (2004). Table 5.8 lists the relative displacements provided by Boeing (Rassaian and Lee, 2007). Typical time variation of applied displacement at node

No. 4 is shown in Figure 5.15. The displacements are applied in a cyclic manner and the magnitudes given in Table 5.8 are the amplitudes for various nodes.

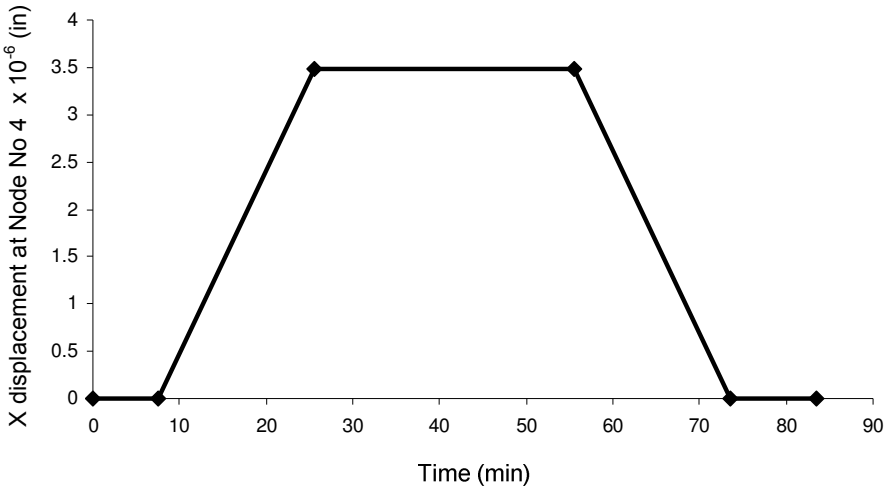

Figure 5.15 Time variation of applied X displacement at node No. 4

5.5.3.4 Applied thermal loading

Applied temperature cycles to the packages are of two different types. Time variation of applied temperature for both cases is shown in Figure 5.16. For SAC_1 and SnPb_1 the temperature is reduced to -55^{o}C from room temperature (20^{o}C) and then it is cycled between -55 and 125^{o}C. For SnPb_2 the temperature is reduced to -20^{o}C from room temperature (20^{o}C) and then it is cycled between -20 and 80^{o}C. Thus the temperature amplitudes in first and second case are 180^{o}C and 100^{o}C, respectively.

For both cases, the temperature is varied at the rate of 10^{o}C per minute. The dwell time at high temperature is 30 min and that at low temperature is 10 min.

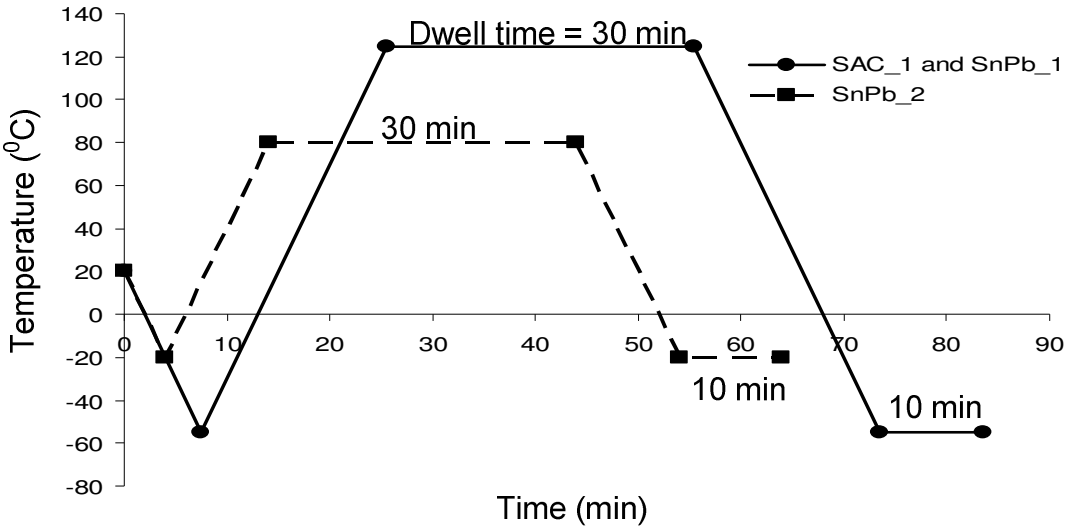

Figure 5.16 Variation of applied temperature with time for various cases

5.5.3.5 Material properties.

Solder alloys are characterized by the *evp* specialization of the MDSC model. e*vp* model parameters for SAC and Sn/Pb alloy listed in Table 5.4 are used for the analyses.

5.5.3.6 Prediction of Failure

The DSC assumes failure when a significant volume fraction (V_f) of the material reaches a critical disturbance (D_f) predefined by the designer. The DSC finite element program (DSC-SST2Dv413) predicts the failure cycle number (N_f) at given D_f and V_f using accelerated procedure (Whitenack et al, 2007; Whitenack 2004; Desai and Whitenack 2001).

Following procedure is used to determine specific pairs of D_f and V_f corresponding to observed failure (Table 5.6)

1. Six different values of D_f are selected. At each D_f, various V_f values (1%, 2%, 3% … 20%) are chosen as shown in Table 5.9.
2. DSC finite element program is used to predict N_f at each set of D_f and V_f.
3. Variation of volume fraction vs predicted number of cycles, for each level of disturbance is plotted. Figures 5.17, 5.18 and 5.19 show such plots for SAC_1, SnPb_1 and SnPb_2 analyses, respectively.
4. Based on observed N_f, the critical volume fraction V_f, at each of the selected D_f is read from the plots as shown in Figures 5.14, 5.15 and 5.16. These combinations of D_f and V_f at observed failure are listed in Table 5.10.

Table 5.9 Chosen sets of D_f and V_f

D_f	V_f (%)
0.750	1, 2, 3 … 20
0.770	1, 2, 3 … 20
0.800	1, 2, 3 … 20
0.820	1, 2, 3 … 20
0.850	1, 2, 3 … 20
0.900	1, 2, 3, 4 and 5

Table 5.10. Various sets of D_f and V_f at observed failure

Disturbance	SAC_1 (N = 3248)	SnPb_1 (N = 2678)	SnPb_2 (N = 7447)
Df	**Vf**	**Vf**	**Vf**
0.75	0.125	0.065	0.09
0.77	0.11	0.055	0.08
0.8	0.09	0.05	0.07
0.82	0.08	0.045	0.06
0.85	0.065	0.035	0.05
0.9	**0.03**	**0.02**	**0.0235**

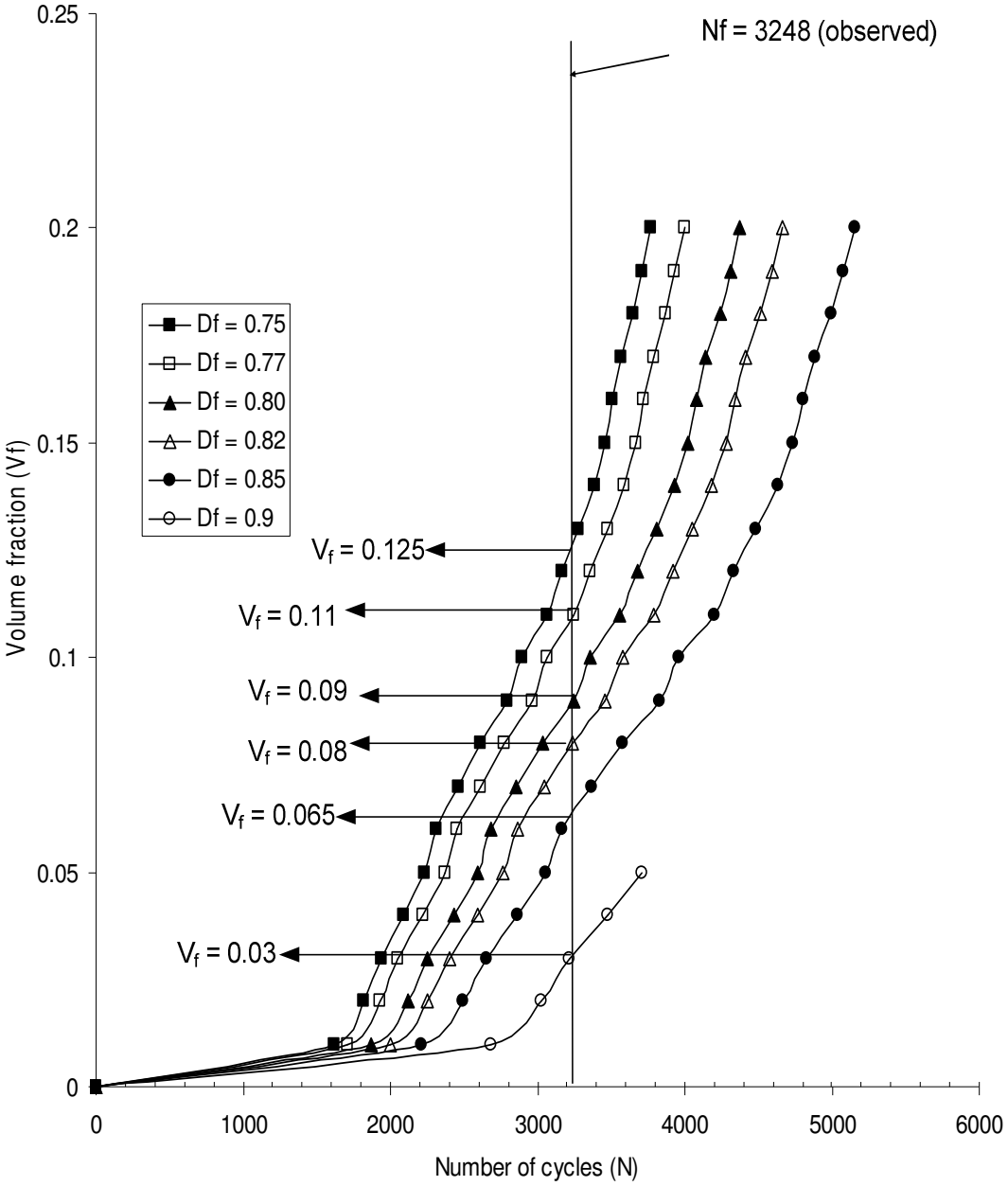

Figure 5.17 Calibration of failure criterion for SAC_1

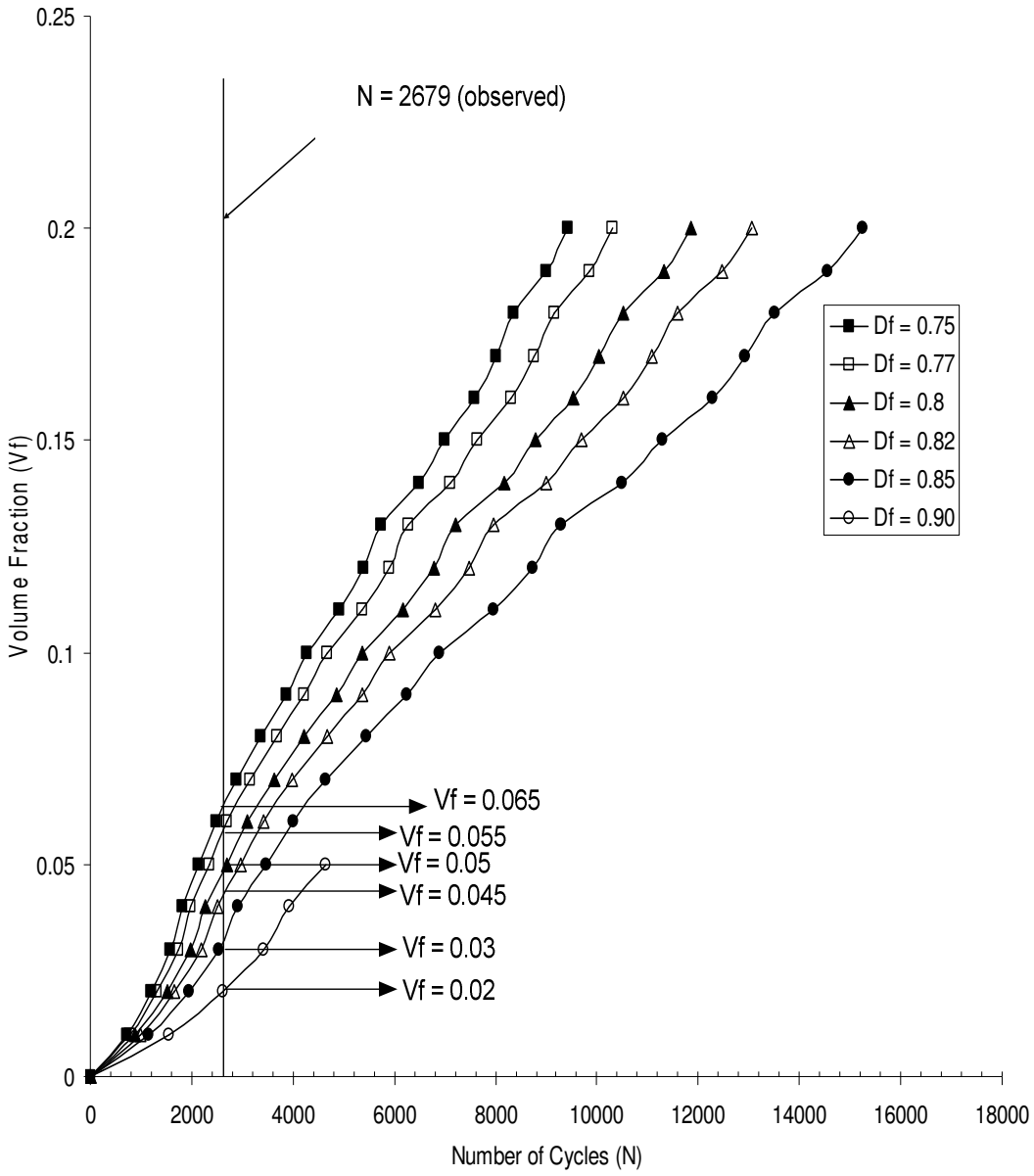

Figure 5.18 Calibration of failure criterion for SnPb_1

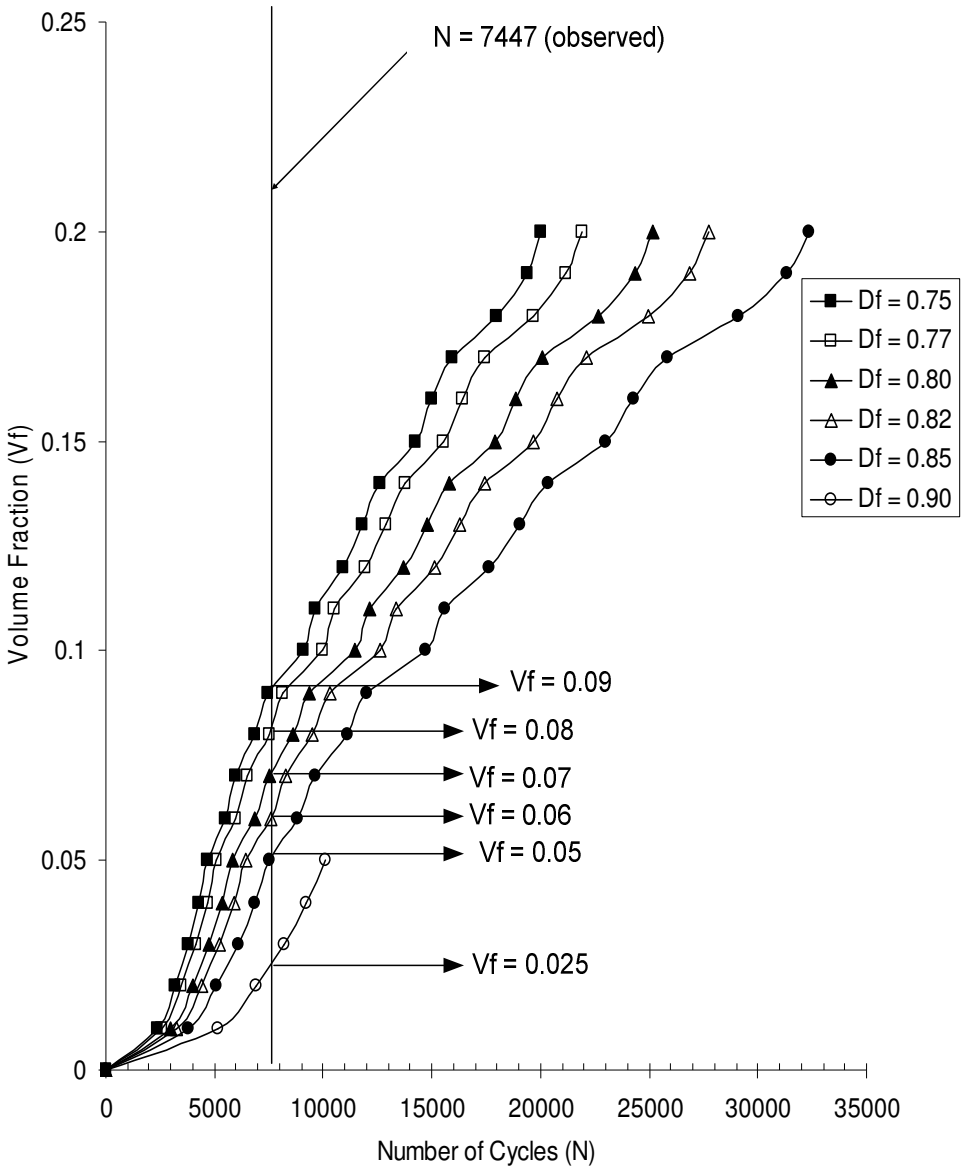

Figure 5.19 Calibration of failure criterion for SnPb_2

From Table 5.10, it appears that at $D_f = 0.9$, the V_f is approximately same (in the range of 2 to 3%); hence $D_f = 0.9$ may be used as an approximate failure criterion for the three cases. In general the final choice of D_f depends upon the properties, geometry and design requirements for specific applications. Based on this approximate criterion, D_f = 0.9, V_f = 0.025 (average), the predicted values of N_f are found from figures 5.17 to 5.19 for each of the three cases (Table 5.11). For example, from Figure 5.17 (SAC_1), at D_f = 0.9 and V_f = 0.025, failure cycle number (N_f) can be read out to be 3124. Similarly N_f for SnPb_1 and SnPb_2 are computed as 3020 and 7563, respectively.

Table 5.11 Comparison of DSC prediction with observed data

At	SAC_1		SnPb_1		SnPb_2	
Df = 0.9	Predicted N_f	Observed N_f	Predicted N_f	Observed N_f	Predicted N_f	Observed N_f
Vf = 0.025	3124	3248	3020	2679	7563	7447

Thus it can be seen that by using the above approximate failure criterion, a good failure prediction can be obtained for the three cases. Failure location can be approximately identified based on the disturbance contours shown in Figures 5.20 (SAC_1) , 5.21 (SnPb_1) and 5.22 (SnPb_2).

SAC_1 (Observed N_f = 3248)

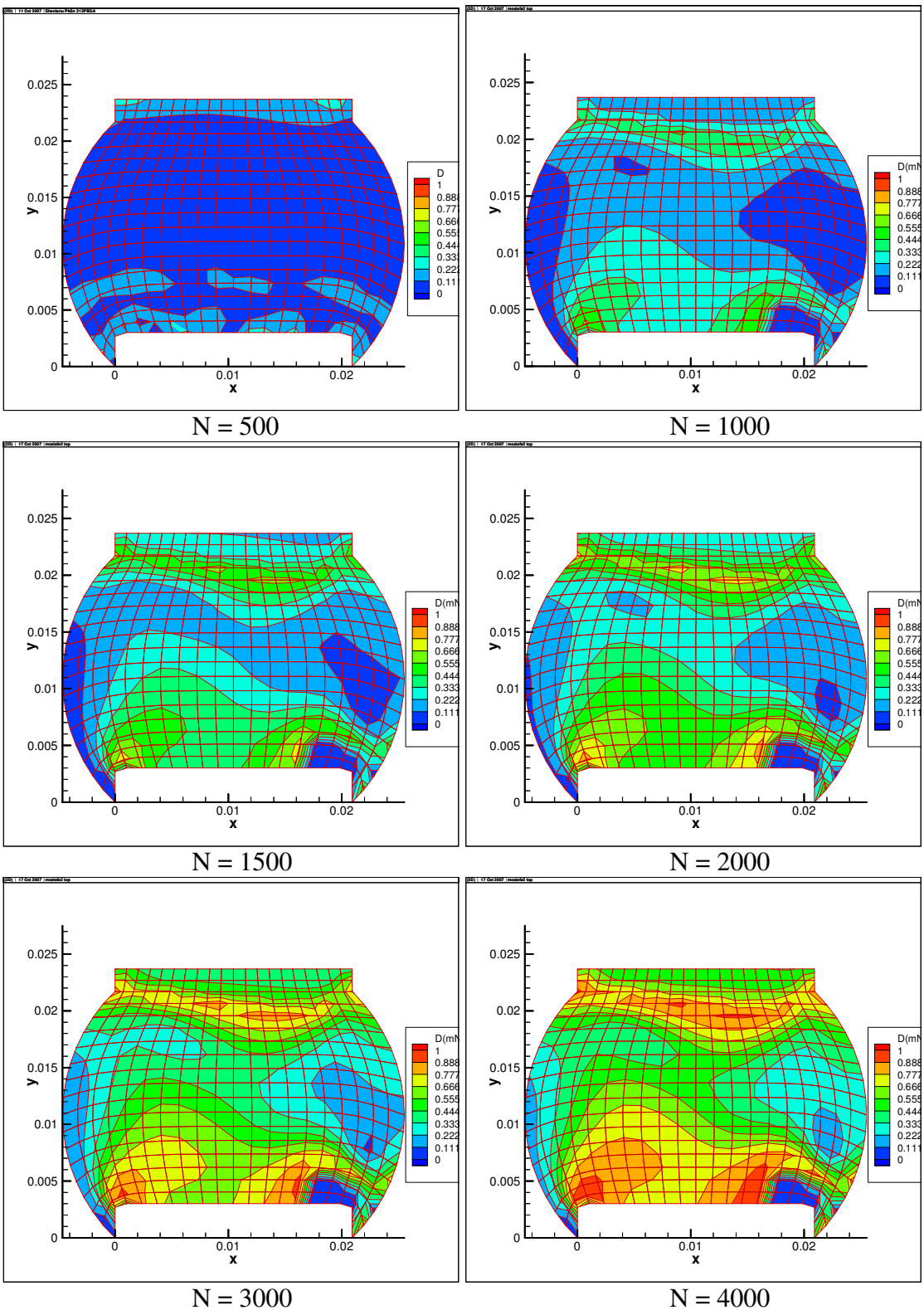

Figure 5.20 Disturbance contours for SAC_1

SnPb_1(Observed N_f = 2679)

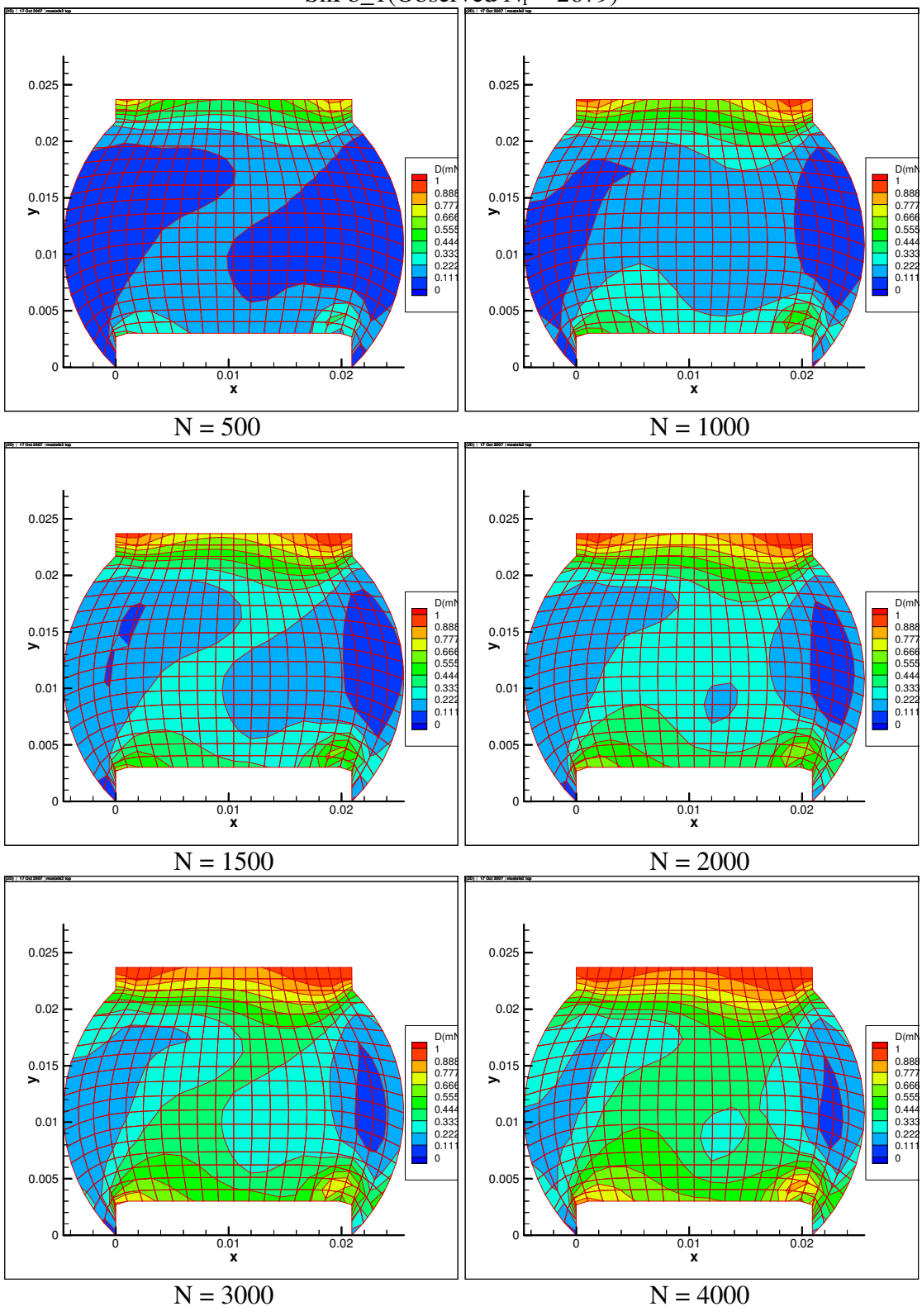

Figure 5.21 Disturbance contours for SnPb_1

SnPb_2 (Observed N_f = 7447)

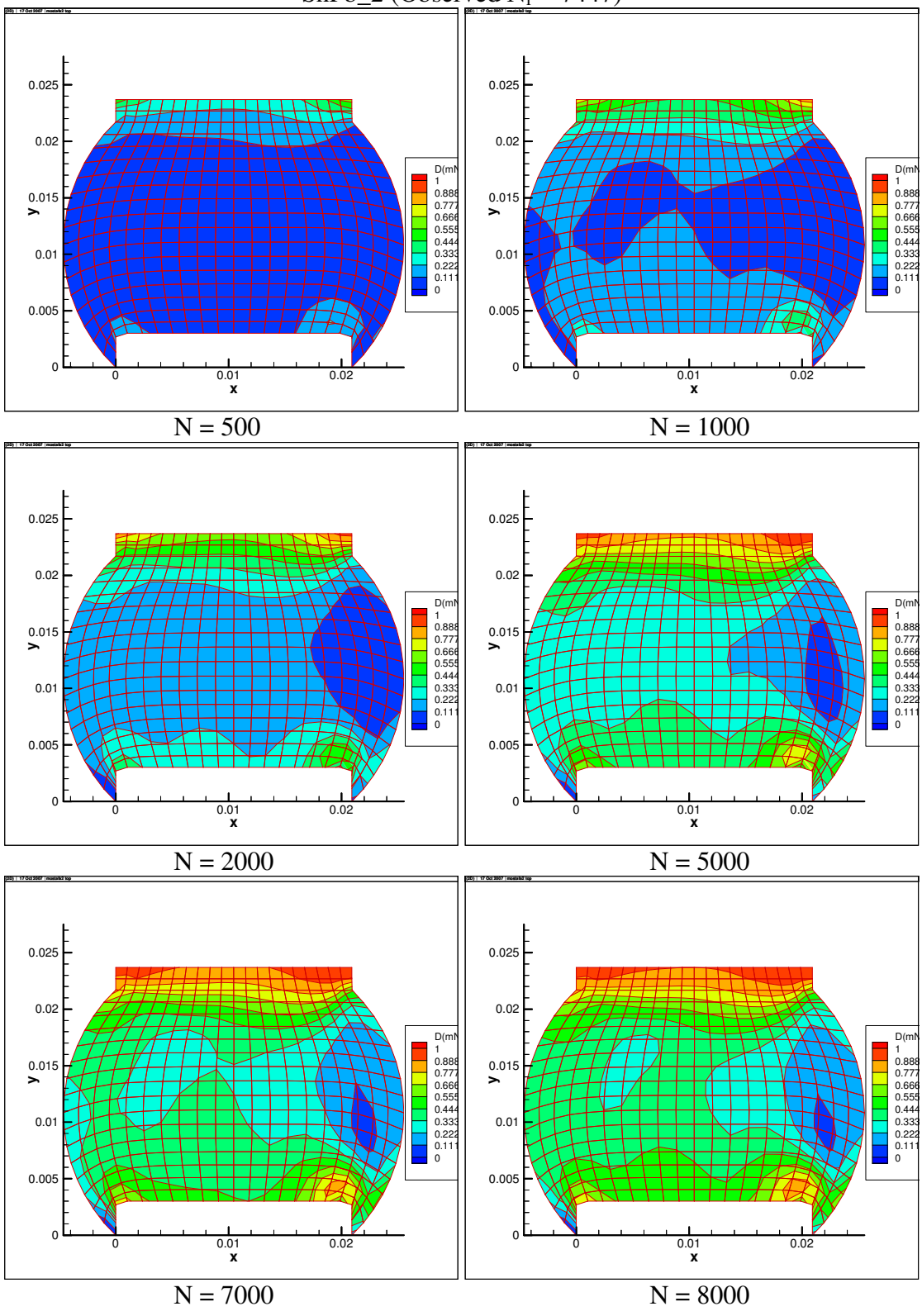

Figure 5.22 Disturbance contours for SnPb_2

5.5.3.7 Comments

From Table 5.11 it can also be seen that the predicted and observed failure cycles are in good agreement. Thus the failure criterion of $D_f = 0.9$ and $V_f = 0.025$ can be considered to be reliable. This criterion is derived based on three examples and for a given material it can be modified as additional test data becomes available. However, the choice of the appropriate criterion for design would depend upon the design requirements for the specific problem, geometry, boundary conditions and loading conditions.

Based on the disturbance contours for SAC_1 (Figure 5.20), a zone just below the top interface can be seen to experience higher disturbance compared to other areas. A small failure zone identified by $D_f = 0.9$ initiates at N = 1000. It grows with number of cycles and between N=3000 and N=4000, a significant fraction of the volume ($V_f = 0.025$) reaches $D_f = 0.9$ in the interface region. This compares well with observed $N_f = 3248$ cycles.

For SnPb_1 and SnPb_2 (Figures 5.21 and 5.22) the high disturbance zone occurs at the top interface. Small failure zones identified by $D_f = 0.9$ initiate at N = 1000 and N = 2000 for SnPb_1 and SnPb_2, respectively. These zones grow in size with number of cycles. For SnPb_1 a significant portion of top interface reaches $D_f = 0.9$ between N = 2000 and N = 3000. This compares well with observed $N_f = 2678$ for SnPb_1. Similar observation can be made for SnPb_2 between N = 7000 and N = 8000, which compares well with observed $N_f = 7447$.

The overall failure locations predicted by DSC can be said to occur in the vicinity of the top interface (between chip and solder alloy). This is consistent with the photomicrographs of typical solder joint failures as shown in Figure 5.2 (Syed, 2001).

Observations made by Whitenack (2004) for the eutectic Sn/Pb alloy are also consistent with this. An exact location of failure may be different depending upon various factors such as geometry of the joint, loading conditions and boundary conditions.

Table 5.6 lists test results for SAC and SnPb alloys under similar loading conditions i.e. under temperature cycling between -55 and 125^0C (SAC_1 and SnPb_1). Number of failure cycles for SAC and SnPb alloys are $(N_f)_{SAC} = 3248$ and $(N_f)_{SnPb} = 2679$, respectively. Thus the SAC alloy shows higher resistance to thermal fatigue as compared to the SnPb. It can be seen that $(N_f)_{SAC}$ is approximately 20% more than $(N_f)_{SnPb}$. This is consistent with observations made by Syed (2001) that the thermal fatigue reliability of SAC alloy is 2 to 20% higher than that of SnPb depending upon the package and thermal loading conditions. Thus the SAC alloy may be considered to be more resistant to thermal fatigue compared to SnPb.

5.5.3.8 Effect of dwell time on failure

Figure 5.16 shows the thermal cycling conditions used for the analyses discussed so far. The dwell time (D_w) as shown in the loading diagram plays an important role towards failure of the solder joint. It can be anticipated that as the dwell time increases the material will develop additional viscoplastic strains per thermal cycle and may experience failure at an earlier cycle. To determine the effect of dwell time on failure, five different analyses similar to the SAC_1 (Table 5.7) are performed. The mesh, boundary conditions, loading conditions and material properties used for these analyses are exactly the same as SAC_1 except for the dwell times. Dwell times (at high temperature) of 15, 30, 60 and 120 min are used.

The failure cycle is predicted in a similar manner as described in the previous section. The approximate failure criterion derived earlier (D_f = 0.9 and V_f = 0.025) is used to identify failure. Figure 5.23 shows the effect of dwell time on the number of cycles to failure.

As expected the failure occurs at an earlier cycle as the dwell time is increased. Also, reducing the dwell time (from 30 to 15 min) delays the failure as indicated by higher N_f. Thus it may be considered that the DSC model successfully characterizes the viscoplastic material behavior.

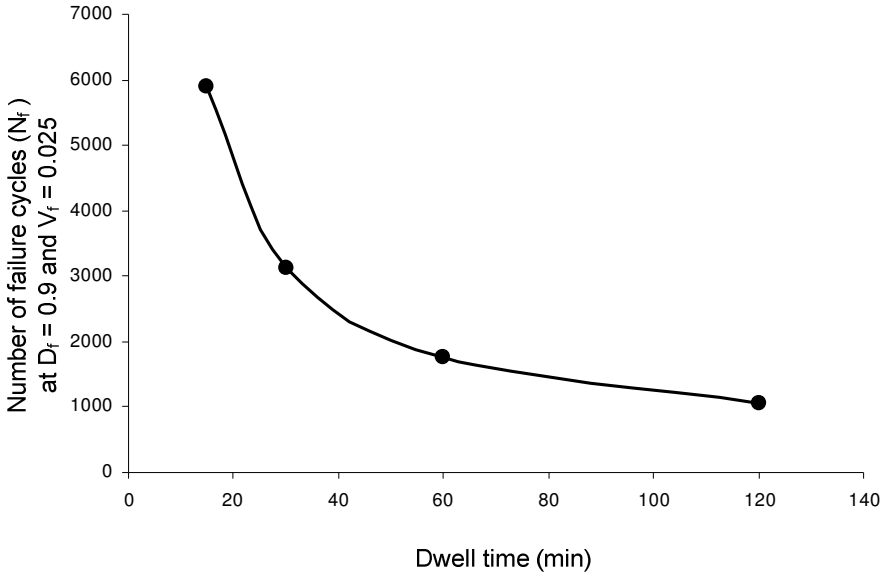

Figure 5.23 Effect of dwell time on failure for BGA 225 package

5.5.4 Validation of Rate Dependent model for SAC alloy

This section discusses the validation of proposed rate dependent model (Section 3.3). The rate dependent model described in Section 3.3 is applied and stress strain

behavior of SAC alloy at different rates is predicted. The procedure for predicting the rate dependent stress strain behavior is described below

1. Construct static curve based on the creep test data (Section 3.2.2.2)
2. Find material parameters for *evp* model at static state as described in chapter 4.
3. Perform stress-strain predictions at various strain rates based on the incremental numerical procedure discussed below.

5.5.4.1 Incremental procedure for non-linear rate dependent stress strain prediction.

Figure 5.24 shows a flow chart of the incremental procedure developed for prediction of rate dependent stress strain behavior. Following are the algorithmic steps and related equations used for predictions

- Input material properties, initial stresses and strain rate at which stress strain behavior is to be predicted
- In case of non-zero initial stresses the initial value of hardening function (α_0) is computed using the condition $F = 0$, where F is the HISS yield function given by Equation 2.8 (a).
- For zero initial stresses an initial α_0 can not be computed. Thus a high value of α_0 (typically 1000) is assumed. A high α_0 implies negligible initial plastic strains as seen from following equation

$$\alpha = \frac{a_1}{\xi^{\eta_1}} \tag{5.1}$$

Thus at a negligible initial value of plastic strain trajectory ξ the denominator of equation 5.1 becomes too small which makes the value of initial hardening function α to be very high.

1. Once α_0 is computed the incremental loading procedure can be started
2. At each applied stress increment the stress invariants (J_1, J_{2D}, J_{3D}) and derivatives of the yield function with respect to stress ($\frac{dF}{d\sigma}$) are computed.
3. The static yield function F_S is computed by using equation 2.8 (a).

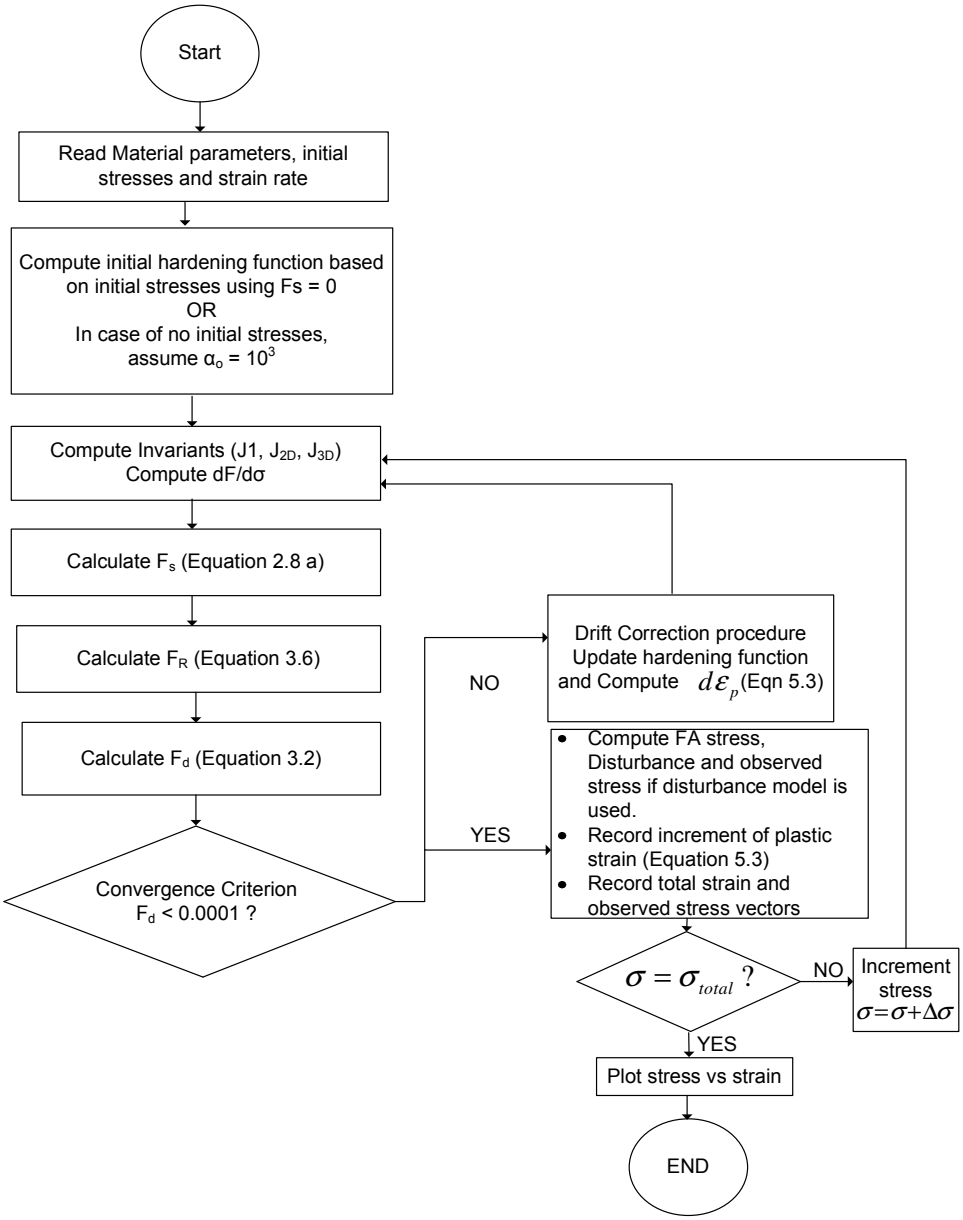

Figure 5.24 Flow chart for numerical procedure developed for validation of proposed rate dependent model.

4. The rate dependent factor F_R (Section 3.3.1) is computed from Equation 3.6 using the given strain rate.
5. Dynamic yield function F_d (Equation 3.2) can be computed.

6. Drift correction procedure (Desai, 2001) is used to correct the current value of $d\xi$ as follows

   - First the normality constant λ is computed based on the known quantities as given by

$$\lambda = \frac{-F_d}{\{-(\frac{dF}{d\sigma})^T . \underset{\sim}{C}^e . (\frac{dF}{d\sigma}) + (\frac{dF}{d\alpha} . \frac{d\alpha}{d\xi}) . ((\frac{dF}{d\sigma})^T (\frac{dF}{d\sigma}))\}} \tag{5.2}$$

   - Then the increment of plastic strain is computed as

$$d\underset{\sim}{\varepsilon}^p = \lambda \frac{dF}{d\sigma} \tag{5.3}$$

   - The increment of plastic strain trajectory is then computed as

$$d\xi = [(d\underset{\sim}{\varepsilon}^p)^T (d\underset{\sim}{\varepsilon}^p)] \tag{5.4}$$

7. $F_d < 1 \times 10^{-4}$, is used as the convergence criterion. Iterations are stopped when this criterion is satisfied
8. The increment of plastic strain (Equation 5.3) obtained in the last iteration is stored along with the increment of applied stress. The total strain increment is obtained from

$$d\varepsilon = d\varepsilon^e + d\varepsilon^p \tag{5.5}$$

where $d\varepsilon^e$ is the increment of elastic strain obtained from Hooke's law

9. Total strain and stress are computed as follows

$$\begin{aligned} \underset{\sim}{\varepsilon} &= \underset{\sim}{\varepsilon} + d\underset{\sim}{\varepsilon} \\ \underset{\sim}{\sigma} &= \underset{\sim}{\sigma} + d\underset{\sim}{\sigma} \end{aligned} \tag{5.6}$$

10. If disturbance model is used, the FA stress, disturbance and observed stress are computed using equations 2.7 (b), 2.12 and 2.13, respectively. The computed values are then recorded (stored) for use in plotting.
11. Steps 1 to 9 are repeated for every load step.
12. Observed stress and strain values recorded in step 10 are plotted to obtain the stress strain curve.

The above procedure is applied to predict the rate dependent behavior of the SAC alloy. Material parameters listed in Table 5.4 are used. Figures 5.25 to 5.27 show rate dependent predictions for the SAC alloy at 125^0C, 75^0C and 25^0C, respectively. It can be seen that the predictions are in very good agreement with the test data. As expected the material can be seen to exhibit stronger response as the strain rate increases. The proposed rate dependent model (Section 3.3) can thus be considered to be capable of successfully handling the effect of strain rate on material behavior.

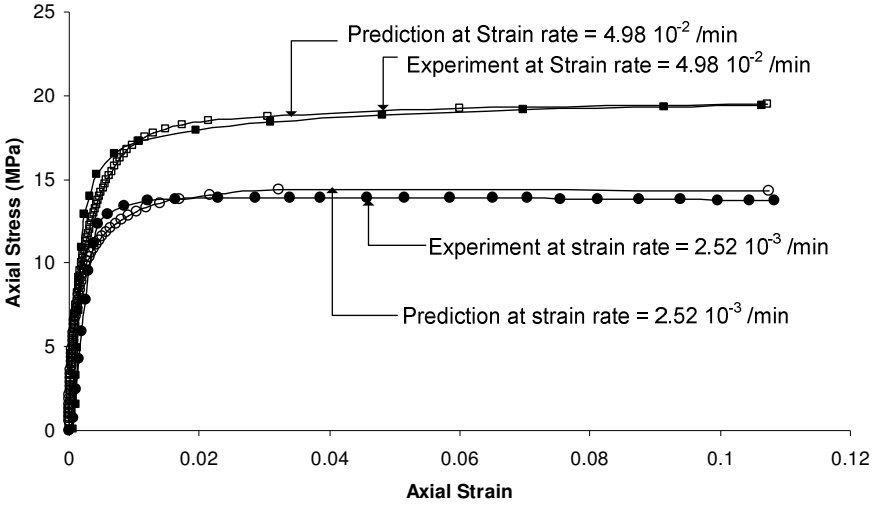

Figure 5.25 Rate dependent prediction of stress strain behavior for Sn/3.9Ag/0.6Cu solder alloy at 125^{o}C

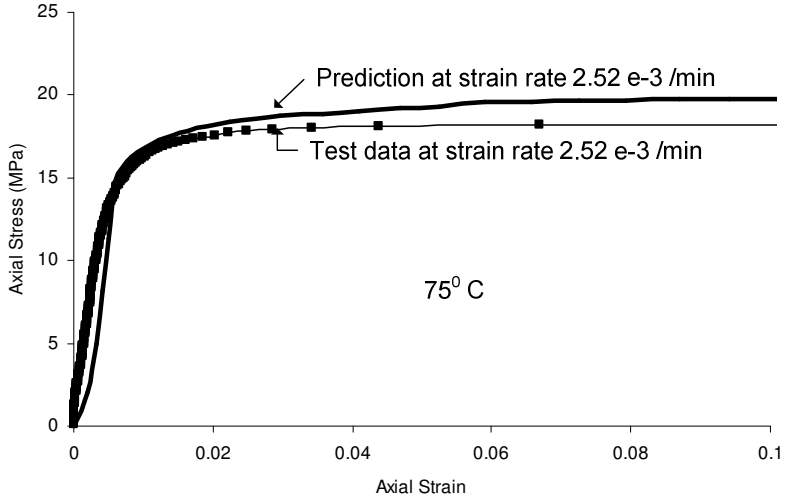

Figure 5.26 Rate dependent prediction of stress strain behavior for Sn/3.9Ag/0.6Cu solder alloy at 75^{o}C

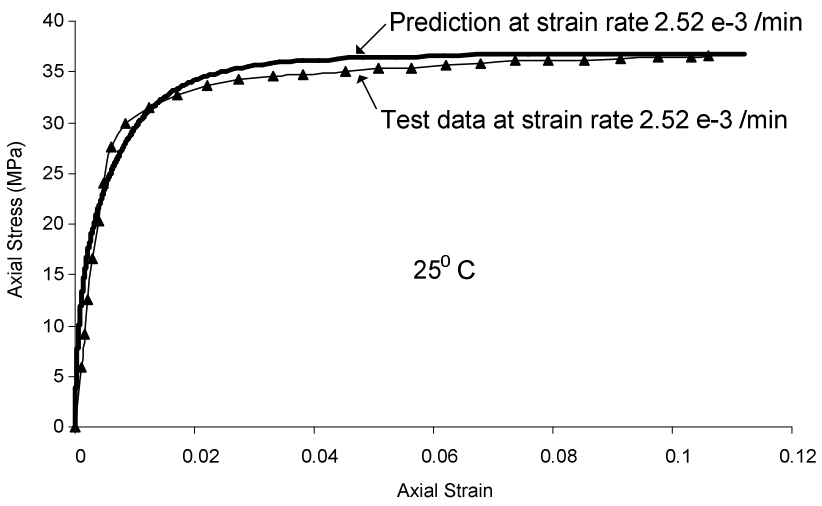

Figure 5.27 Rate dependent prediction of stress strain behavior for Sn/3.9Ag/0.6Cu solder alloy at 25^{o}C

CHAPTER 6

APPLICATION of DSC to PREDICTION of GLACIAL MOTION

6.1 Introduction

Glaciers and Ice sheets cover more than fifteen percent (Patterson, 2004) of the earth's land area. They move continuously and the movement can be as rapid as tens of meters per year. The global sea level and climate are affected due to this motion. It is thus critical to understand the factors causing it and the mechanics behind them. The overall motion is generally divided into three parts,

1. Deformation in the ice
2. Sliding at the interface between ice and underlying sediment.
3. Sediment (till) deformation

For many years, researchers believed that the contribution of sediment deformation toward overall motion is negligible; however, recent studies have shown that the sediment (till) deformation may contribute as much as 90 percent of the overall motion (Boulton and Jones 1979). The current research focuses on characterizing the behavior of till to better understand its role and contribution towards overall motion. Following section describes the problem and identifies specific research goals.

6.2 Problem description and research objectives

Figure 6.1 shows a schematic of the ice sheet and its underlying sediments. The accumulation zone represents the area in which extreme cold conditions prevail and snow fall occurs. At the other end, marked as ablation zone, the warm conditions prevail

causing rapid ice melting and calving into the sea. In the mid region the ice bed may be frozen and coupled to ice (Non-deforming sediment) or warm from geothermal heat (deforming sediment). The warm bedded parts of ice sheets are supported by the deforming sediments or tills. Bedrock shown in the figure represents rigid non deforming rock supporting the deforming or non deforming sediments.

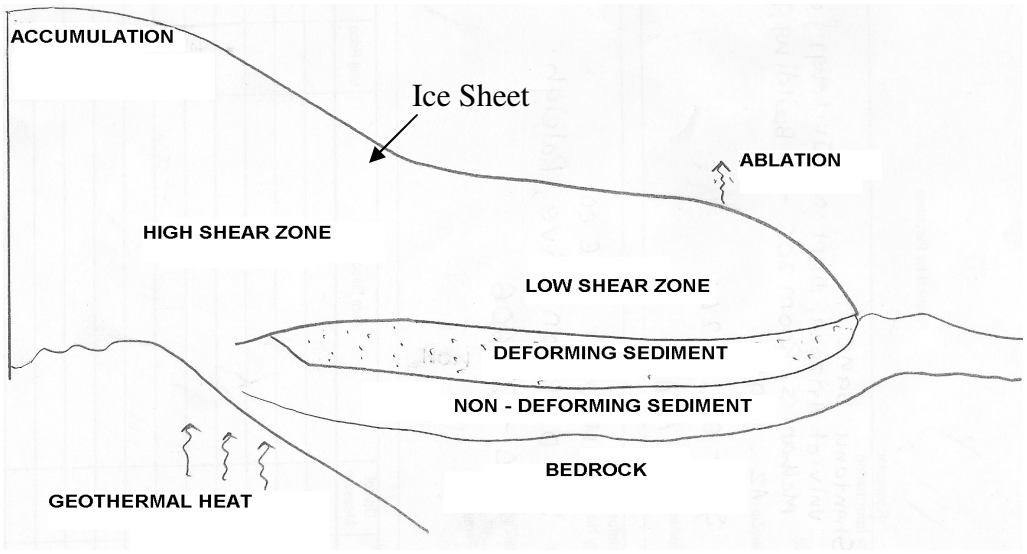

Figure 6.1 Schematic of the ice sheet and underlying sediments.

Part of the ice sheet motion which is caused due to sediment deformation is mainly due to the gravity induced shear stresses at the ice – till interface. The properties and mechanical behavior of the tills play an important role in understanding the overall motion. Hence in this work two glacial tills are studied for their mechanical behavior.

Till characterization is accomplished by conducting a series of laboratory tests and using the test results for calibration of the DSC model. Later, a numerical simulation of a hypothetical field problem is performed to formulate a criterion for failure and motion of the tills. Comparison of the current approach and Mohr Coulomb approach,

which has been widely used in the past, is also performed. Specific research objectives for this problem are listed below

1. Collection till samples from the field.
2. Determination of soil index properties.
3. Laboratory tests on tills for shear and creep behavior.
4. Determination of DSC model parameters.
5. Specimen level validation of the DSC model.
6. Numerical simulation of an idealized field problem.
7. Development of a failure and motion criterion.
8. Comparison of DSC and Mohr Coulomb models.

Following sections describe the procedure used for DSC characterization of the glacial tills.

6.3 Glacial tills selected and their significance.

The first of the tills selected for this study is the lower unit of the Tiskilwa Formation in northern Illinois, deposited by the Lake Michigan Lobe of the Laurentide Ice Sheet (Hansel and Johnson, 1996). It is one of the most extensive till units in the Midwest (Wickham and Johnson, 1981), and it represents the widespread tills deposited along the southern Laurentide Ice Sheet margin (Mickelson, et al., 1983; Wickham and Johnson, 1981). Samples for testing were obtained at mid-section of the till layer.

The second till is the Sky Pilot Till of northern Manitoba (Klassen, 1986). The Sky Pilot Till was deposited across the Hudson and James Bay lowlands by southwesterly ice flow (Klassen, 1986; Thorleifson, et al., 1992), and is representative of

the substrate underlying a large portion of the center of the ice sheet (Dredge and Nielsen, 1985; Nielsen, et al., 1986; Thorleifson, et al., 1992). The till is approximately 6 m thick in the study area. Samples were obtained at mid-section. Sample collection for both tills is performed by Dr John Jenson and Dr. Anders Carlson who were co-investigators in this research.

Following section discusses the laboratory test program

6.4 Laboratory Testing of glacial tills

In order to characterize the glacial till using DSC model a series of triaxial tests are performed on both tills. Tests are mainly required to find the parameters for the elastic, plastic, disturbance, and creep aspects of the DSC model. Two types of triaxial tests were performed on the tills.

1. Conventional Triaxial Compression (CTC) tests.
2. Creep tests.

Table 6.1 lists the details of the test program.

6.4.1 Conventional triaxial compression (CTC) tests

In this type of test, the sample is first consolidated by applying a hydrostatic or confining pressure, σ_3', in the triaxial cell, and then a strain-controlled test is performed with the strain rate of 0.05 in/min (1.275 mm/min), during which the axial stress, σ'_1, is increased to produce the shear stress, $\sigma_1 - \sigma_3$.

6.4.2 Creep tests

For creep tests samples are first consolidated in the triaxial cell under a given confining pressure and then a constant axial load is applied by using dead weights. Then

Table 6.1 Details of the triaxial tests for Tiskilwa and Sky Pilot Tills.

Type	Number of Tests		Confining pressure (kPa)		Comments
	Tiskilwa	Sky Pilot	Tiskilwa	Sky Pilot	
Consolidated undrained (CTC)	10	8	100,200 300,500	100,200, 300,400	Results of these tests are used to calculate the DSC model parameters.
Consolidated undrained (CTC) (Independent)	2	2	150,400	150, 500	Results of these tests are not used for parameter calculation but are used for independent validations.
Creep Tests	11	11	100, 200, 400	100, 200, 400	At each confining pressure, 4 tests are performed at 20, 40, 60 and 80% of the peak stresses (obtained from CTC tests). Results of these tests are used to obtain the parameters for the MDSC model.
Creep Tests (Independent)	4	4	300	300	These are similar to above tests, but results of these tests are not used for parameter calculation but rather are used for independent validations.

[a]Note: At least 2 unloading cycles before and after the peak stress are performed, except for the creep tests.
[b]Low-confining-pressure test conducted using procedures described in Section 3.2 for Tiskilwa till only.

the growth of strain in the sample with time is recorded. The constant axial stresses applied to the creep samples are 20, 40 , 60 and 80% of the observed peak stress obtained from the CTC test at corresponding confining pressure.

The procedure used for reconditioning of the field samples and preparation of samples for laboratory testing is presented in the following section.

6.5 Soil conditioning and sample preparation

Following steps are followed in order to prepare samples for laboratory tests on Tiskilwa and Sky Pilot tills. For both types of tests, the following procedure is used for sample preparation.

6.5.1 Resizing of field material

Tills collected from the field are in the form of large chunks. They are powdered such that all of them pass through a 2.00 mm sieve. Rocks and other random inclusions in the till are discarded.

6.5.2 Consolidation before testing

Powdered material is mixed with sufficient water so that it forms uniform slurry such that the soil has somewhat greater amount of water than required for 100% saturation. Excess water is drained in the process of consolidation that follows. Consolidation is achieved by using a special consolidometer of diameter 325 mm (13 inches) and height of 275 mm (11 inches). The consolidation pressure applied on the soil should not be greater than the actual test conditions so that the samples are not overconsolidated. Typically, if the lowest confining pressure at which triaxial test is carried out is σ'_3 and the consolidation pressure is σ_0 then the ratio of σ'_3 to σ_0 should not be less than 1.5 (Head, 1986). For most of the tests performed in this research the minimum confining pressure is 100 kPa so the consolidation pressure used is 50 kPa. Additional tests (See Section on low confining pressure tests, below) were performed at 20 and 50 kPa to verify applicability of the test results at the low-confining pressures.

6.5.3 Sample extrusion

After consolidation i.e. when there is no significant change in the measured vertical displacements, Shelby tubes are pushed in the soil in the consolidation device. These tubes are then placed on the sample extruder to obtain cylindrical samples. This process of remolding does not have any significant effect on the observed stress strain behavior (Bell, 2002).

6.5.4 Consolidation in triaxial cell

The sample 7.0 cm x 14.0 cm (2.8 in X 5.6 in) (diameter x height) is placed in the triaxial cell and is consolidated by applying the planned confining pressure before the subsequent shear test.

6.5.5 Shear test

The tests are conducted under undrained conditions with displacement controlled loading at the rate of 1.275 mm/min (0.05 in/min). Deviatoric stress $(\sigma_1 - \sigma_3)$, axial strain (ε_1) and pore water pressure (u) during the test are recoded. Loads and displacements are applied using a MTS hydraulic actuator. The hydraulic actuator functions are controlled electronically by using MTS – Test star II software.

6.5.6 Low-confining-pressure tests

Effective stresses in the glacial till at the base of modern ice sheets (Engelhardt and Kamb, 1997; Engelhardt et al., 1990; Kamb, 2001) have been observed to be very low, in the range of 10 to 50 kPa. Thus the parameters computed from the triaxial (CTC) test results should be checked for validity at lower confining pressures. However, in the

laboratory it is difficult to perform triaxial tests on the soils at very low confining pressure because of following reasons:

1. It is difficult to obtain a cylindrical sample that can stand its own weight at low confining pressures. (Often, the sample collapses even before installing it in the triaxial cell.)
2. The sample may deform in arbitrary and irregular shapes. Hence, it is difficult to compute stress based on the deforming diameter.

For this work, the method of sample preparation for low confining pressures was altered so as to partly overcome above problems. Thick slurry of the till (Till + water) was poured in cylindrical molds and then it was frozen so that the sample can stand its own weight. After freezing, the mold is taken apart and the sample is installed in the triaxial cell. Loading procedure is the same as other CTC tests. Tests were performed at $\sigma_3' = 20$ and 50 kPa.

6.6 Index Properties of the tills

The two glacial tills were investigated for basic index properties such as grain size distribution, liquid limit and plastic limit. Standard test procedures (Lambe and Whiteman, 1979) were used. Field moisture content of Tiskilwa and Sky Pilot till is recorded as 17 and 16 percent, respectively.

Figure 6.2 shows the grain size distribution of the two tills. It was observed that the Tiskilwa and Sky Pilot tills have a significant silt content of 39% and 57%, respectively (Carlson, 2005). The high silt content in Sky Pilot till is evident from the slight red color. Table 6.2 shows other index properties of the tills. It can be observed that

the two tills have similar composition and properties. Results of the CTC and creep tests presented in next section also indicate this similarity.

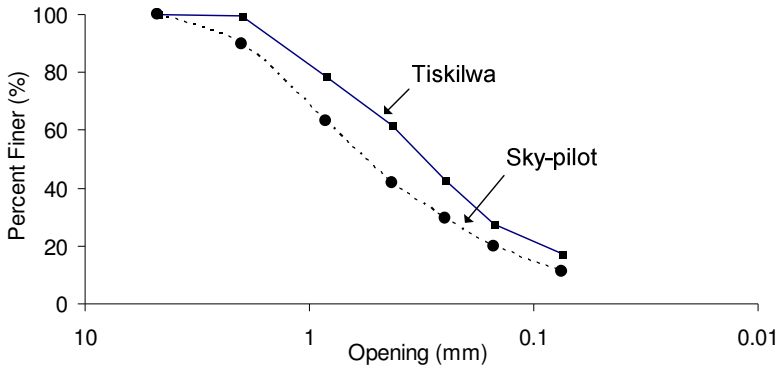

Figure 6.2 Grain size distributions for Tiskilwa and Sky Pilot till.

Table 6.2 Index Properties of Two Tills

Properties	**Tiskilwa**	**Sky Pilot**
Field Moisture Content (%)	17	16
Plasticity Index (%)	16±2	18±2
Liquid limit (%)	22 ±2	20 ±2

6.7 Test results

Figures 6.3 and 6.4 show results of CTC tests on Tiskilwa and Sky Pilot till, respectively. As noted before the CTC results on two tills are similar in nature. Both tills show initial hardening behavior leading to peak followed by degradation or softening. The Sky Pilot till shows relatively less softening compared to the Tiskilwa till.

The creep tests on both tills are conducted at various confining pressures and different axial stresses. The results of creep tests on Sky Pilot tills are shown in Figures

6.5(a) through 6.5(d). Typically four tests are conducted at 4 confining pressures. At each confining pressure, four different constant axial stresses are the applied. These are computed as 20%, 40%, 60% or 80% of the peak stress observed from the CTC test at that confining pressure.

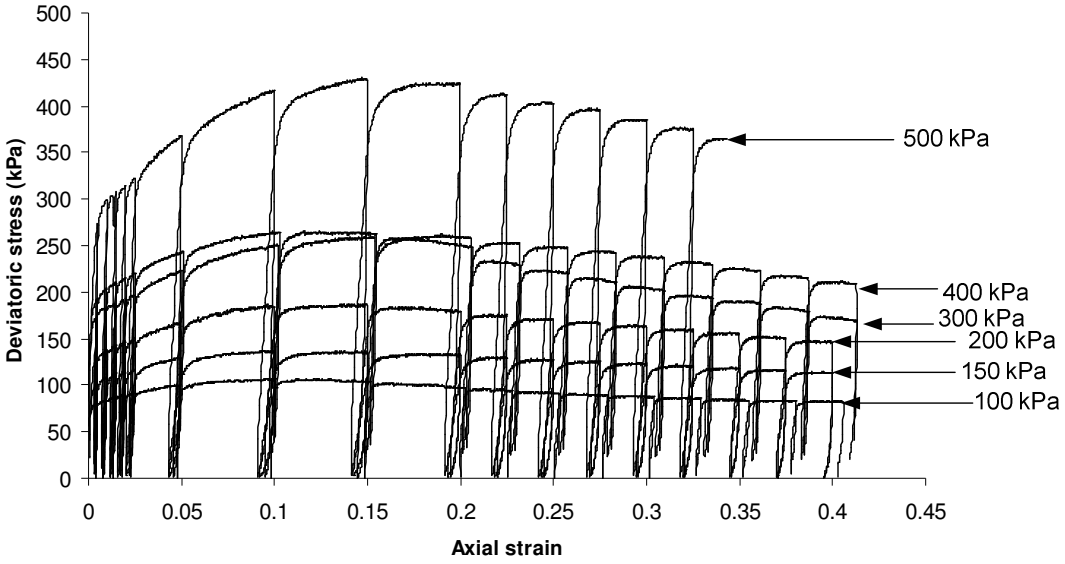

Figure 6.3 CTC test data for Tiskilwa till.

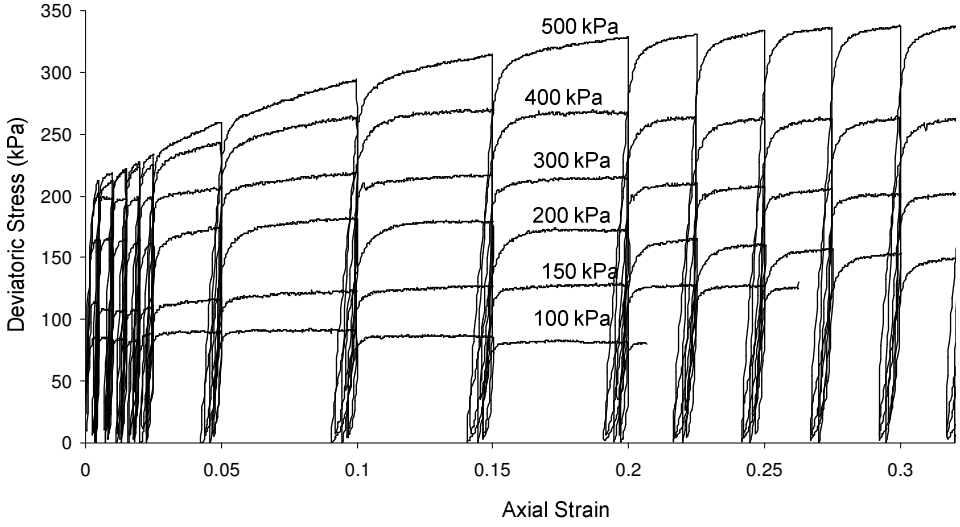

Figure 6.4 CTC test data for Sky Pilot till

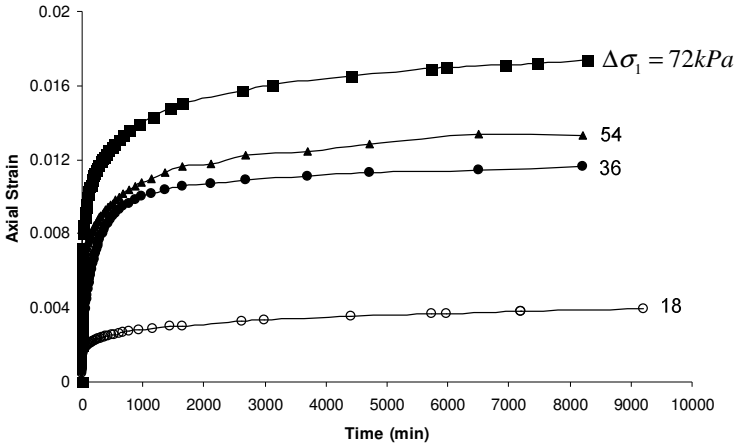

(a) Confining pressure = 100 kPa

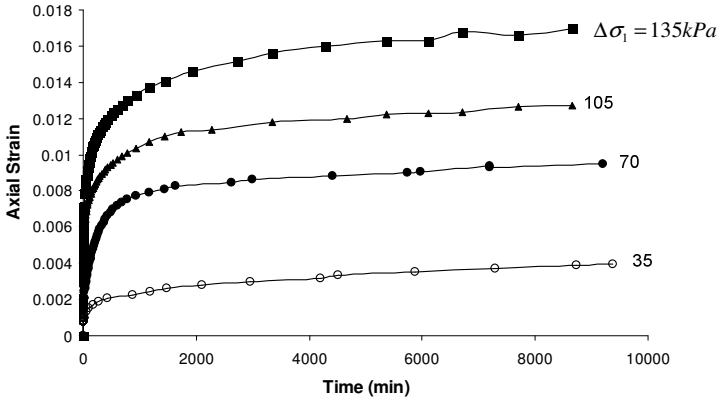

(b) Confining pressure = 200 kPa

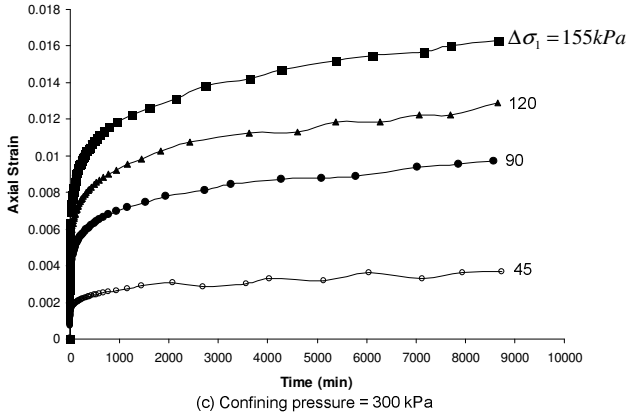

(c) Confining pressure = 300 kPa

Figure 6.5 Creep tests on Sky Pilot tills at (a) 100, (b) 200 (c) 300 (d) 400 kPa confining pressure.

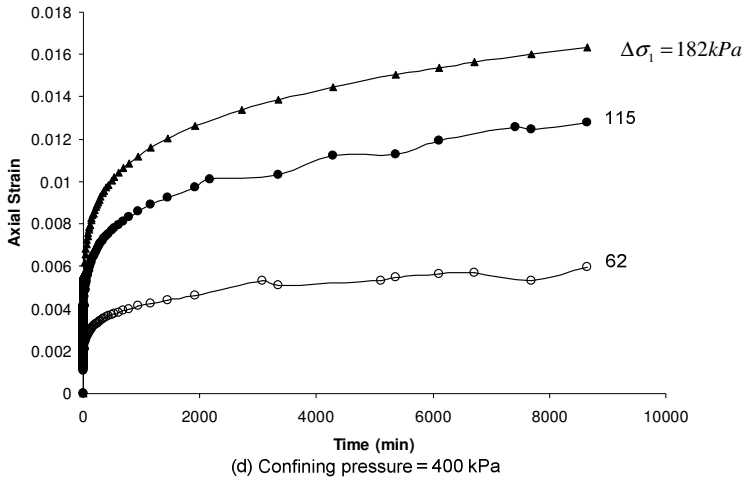

Figure 6.5 (continued) Creep tests on Sky Pilot tills at (a) 100 (b) 200 (c) 300 (d) 400 kPa confining pressure.

Rate dependent behavior

In order to see the effect of strain rate on behavior of glacial tills three rate dependent tests on Sky Pilot Till are conducted. The three rates at which the tests are performed are 12.8, 1.28 and 0.128 mm/min (0.5, 0.05 and 0.005 in/min). Figure 6.6 shows results of the three tests.

It can be seen that the till gains strength as the applied strain rate is higher. It is also observed that the peak stress occurs at different strains for all the three tests. For the test conducted at 0.128 mm/min (0.005 in/min) the peak occurs at axial strain of about 0.16 whereas for the tests at 1.28 and 12.8 mm/min the peak occurs at axial strain of 0.1 and 0.03, respectively.

It should also be noted that the test at the rate of 12.8 mm/min has fewer unloading cycle compared to other two. It is a result of faster loading rate which does not allow enough time for the data acquisition system to record sufficient number of data points. Figure 6.6 (b) shows constructed static curves which may be considered as very slow rate tests for Sky Pilot till.

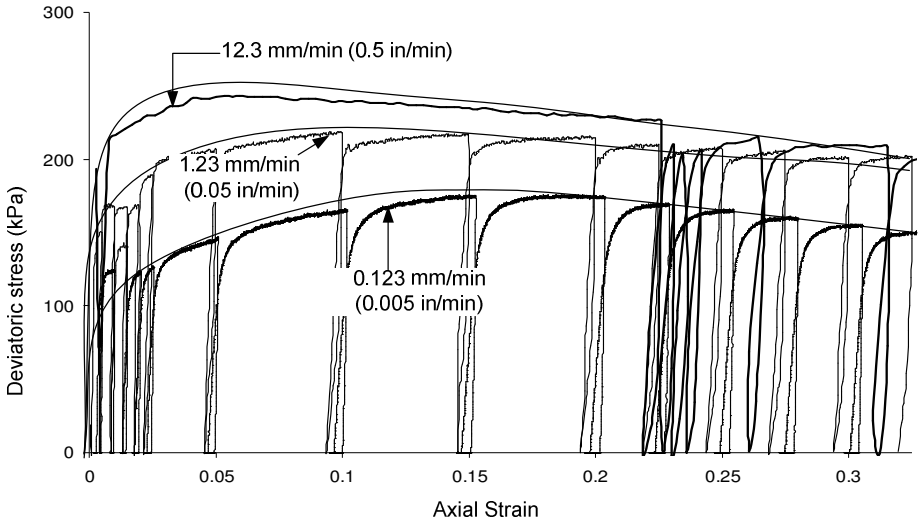

(a) Rate dependent tests on Sky Pilot till (300 kPa confining pressure)

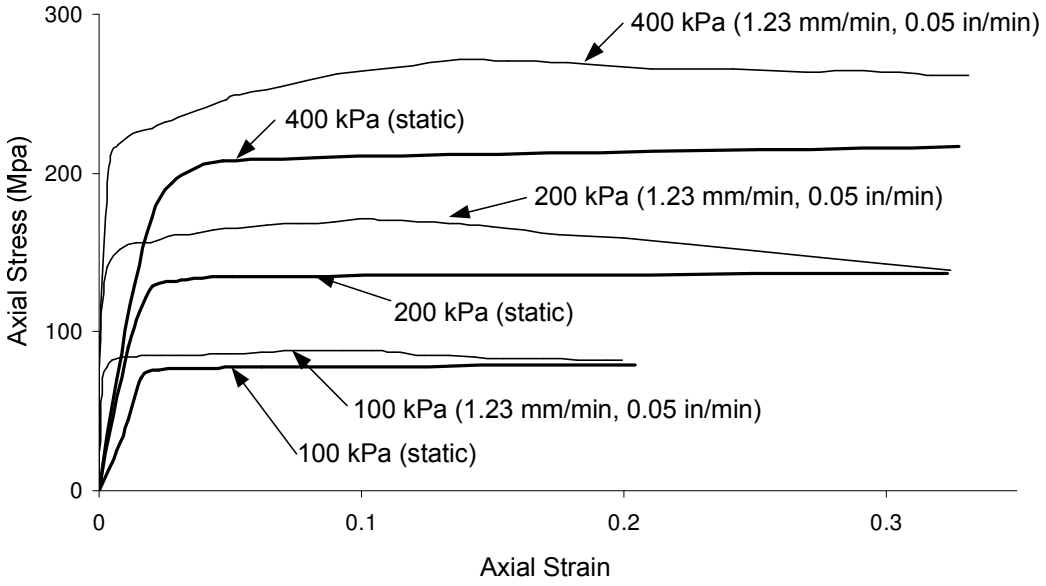

(b) Static curves constructed from creep test data for Sky Pilot till
Figure 6.6 Rate dependent tests and static curves for sky pilot till.

Some of the CTC and creep tests presented above are used for determination of DSC model parameters. Procedure for parameter determination is given in Chapter 4. Smooth curves enveloping the actual test curves are drawn to show the overall response.

6.8 DSC model parameters

For Tiskilwa till the elastoplastic parameters are computed from the CTC tests at 100,200,300 and 500 kPa confining pressure. The tests at 150 and 400 kPa used for independent validations.

For Sky Pilot till the elastoplastic parameters are computed from the CTC tests at 100, 200, 300 and 400 kPa confining pressure. Tests at 150 and 500 kPa are used for independent validations. Creep parameters for Sky Pilot till are computed by construction of static curves as shown in Figure 6.6 (b). The creep test results at 100, 200 and 400 kPa confining pressure are used for parameter determination while the tests at 300 kPa are used for independent validation. Table 6.3 – 6.5 lists the parameters for elastoplastic, elasto-viscoplastic and viscoelastic-viscoplastic models, respectively. Parameters in the *evp* model as determined from the static curves.

6.9 DSC model validation

Validation of the DSC model involves

1. Validation of elastoplastic model (6.9.1)
2. Validation of creep model. (6.9.2)
3. Validation of rate dependent model (6.9.3)

Table 6.3 Elastoplastic parameters for Tiskilwa and Sky Pilot tills

Category	Symbol	Tiskilwa Till	Sky-Pilot Till
Elastic	E	52732	50470
	ν	0.45	0.45
Plastic - HISS	γ	0.0178	0.0092
	β	0.36	0.52
	n	3.6	6.85
	$\bar{c}$	6.789	16.67
Plastic - hardening	a_1	2e-4	1.35e-7
	η_1	0.27	0.14
Disturbance	A	20.2	5.5
	Z	2.68	1
FA (critical) state	$\bar{m}$	0.1	0.09
	λ	0.21	0.16
	e_0	0.48	0.52

Two levels of validation for each model is performed

- Level 1 – Prediction of test results used for determination of parameters.
- Level 2 – Predictions of tests not used for parameter determination. This is also termed as independent validation.

Level one and level two back predictions are performed by using a computer program (Desai, 2002) for integration of incremental equations (Equation 2.13).

Table 6.4 Static (HISS) parameters for Sky-Pilot till.

Category	Symbol	100 kPa	200 kPa	400 kPa
Elastic	E	41000	45000	58000
	ν	0.45	0.45	0.45
HISS	γ	0.0092	0.0092	0.0092
	β	0.52	0.52	0.52
	n	6.85	6.85	6.85
	$\overline{c}$	16.67	16.67	16.67
	a_1	5×10^{-7}	2.43×10^{-9}	2.45×10^{-9}
	η_1	1.33	1.23	1.24
Creep(*evp*)				
	Γ	5.5E-06	2.17E-07	3.4E-08
	N	1.625	2.2	2

Table 6.5 *vevp* model parameters for Sky-Pilot till

vevp* creep parameters	**Confining pressure ($\sigma_2 = \sigma_3$)**		
	100 kPa	**200 kPa**	**400 kPa**
E_1 **(kPa)**	6666	24244	30000
E_2 **(kPa)**	42500	83333.33	63333.33
ν_1	0.45	0.45	0.45
ν_2	0.45	0.45	0.45
Γ_1 **(kPa^{-1}min^{-1})**	0.001446	0.001841	4.24E-06
Γ_2 **(kPa^{-1}min^{-1})**	0.006	0.006	0.006
N_1	2.275	4	1.4
N_2	1.625	2.2	2

6.9.1 Validation of elastoplastic model.

Figures 6.7 and 6.8 show results of Level 1 and Level 2 predictions for Tiskilwa Till, respectively. Similarly, Figures 6.9 and 6.10 validation results for Sky Pilot till.

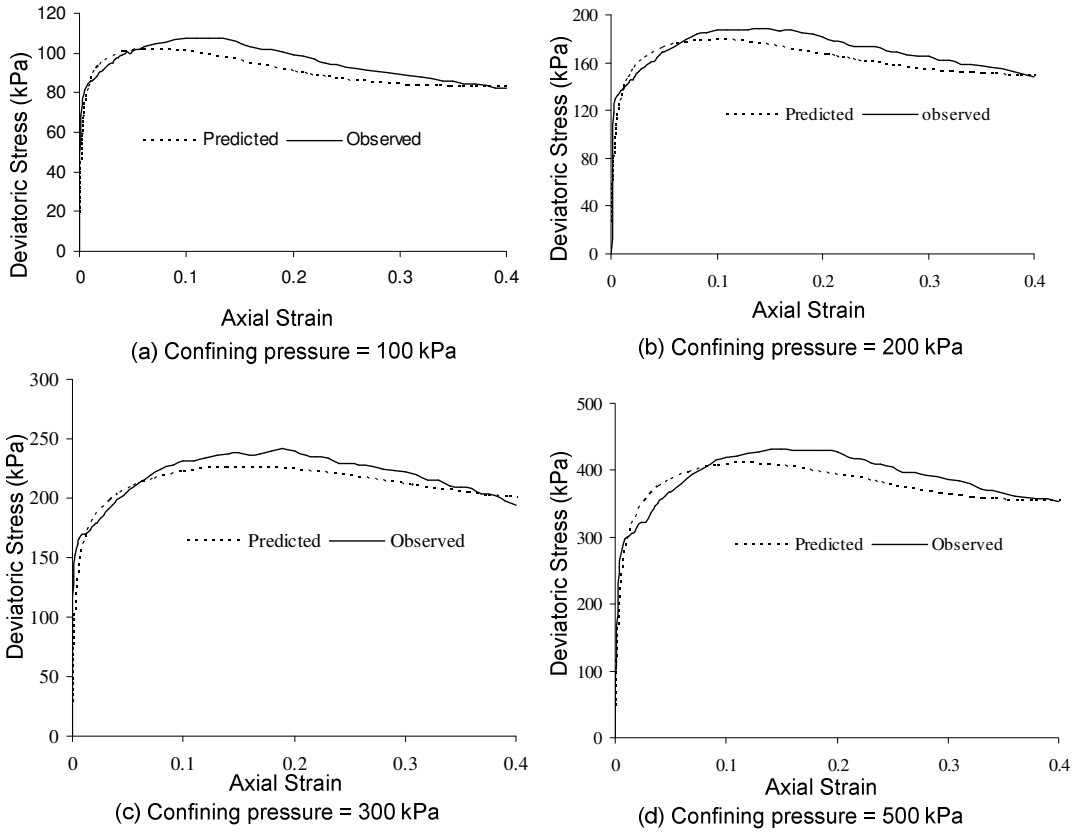

Figure 6.7 Level 1 validation results for Tiskilwa till.

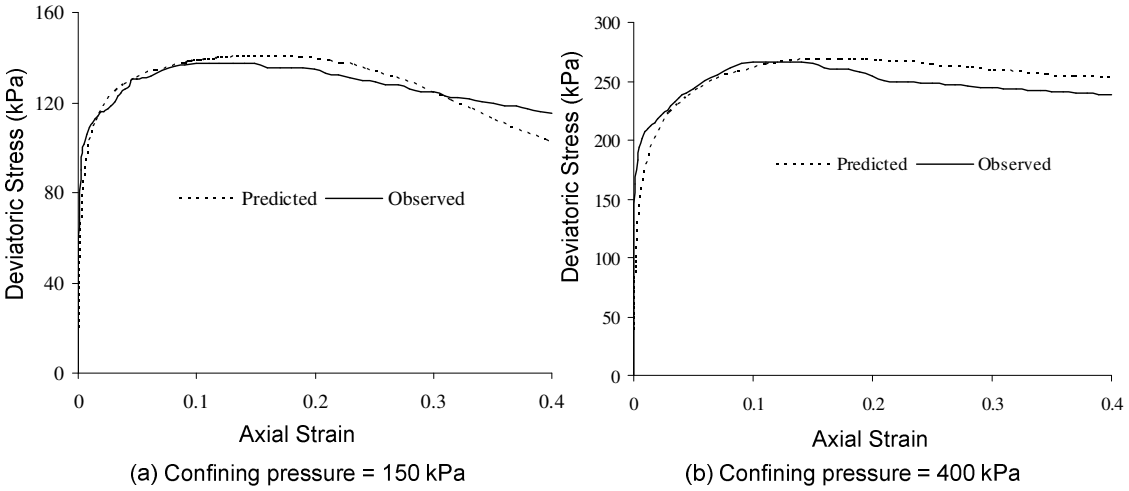

Figure 6.8 Level 2 (Independent) validation results for Tiskilwa till.

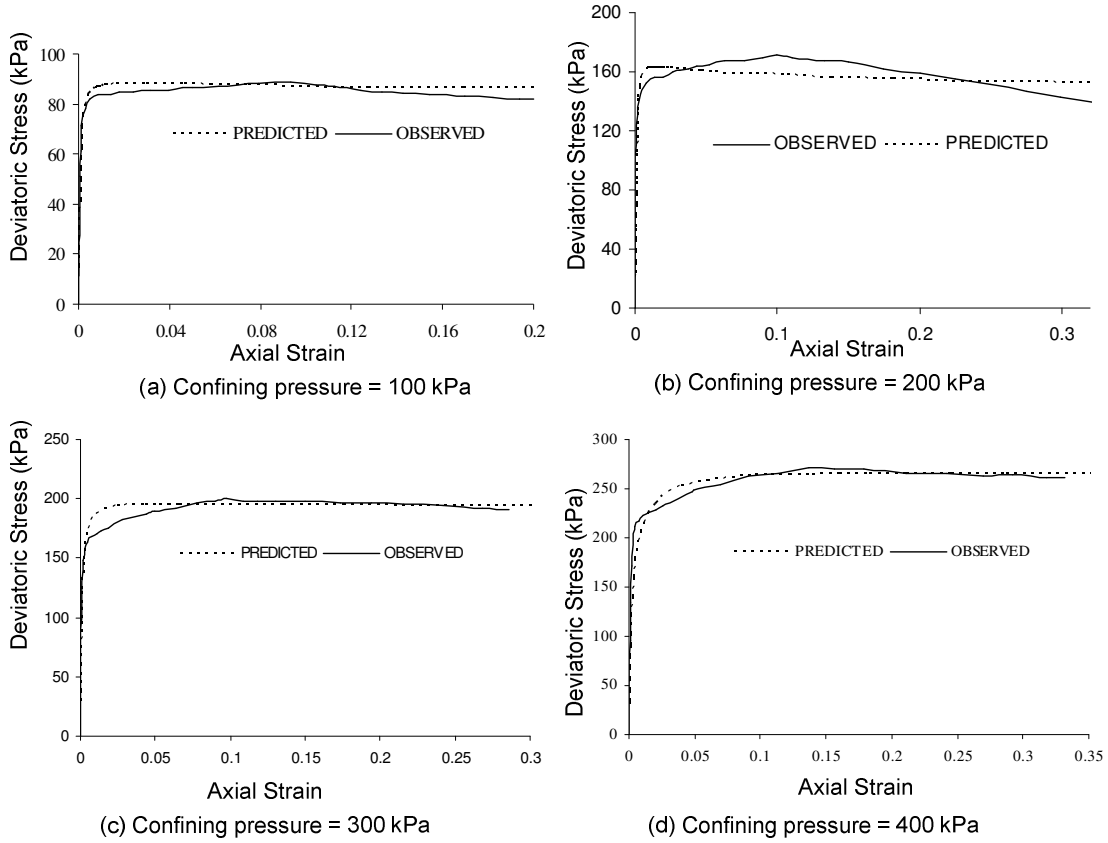

Figure 6.9 Level 1 validation results for Sky Pilot till.

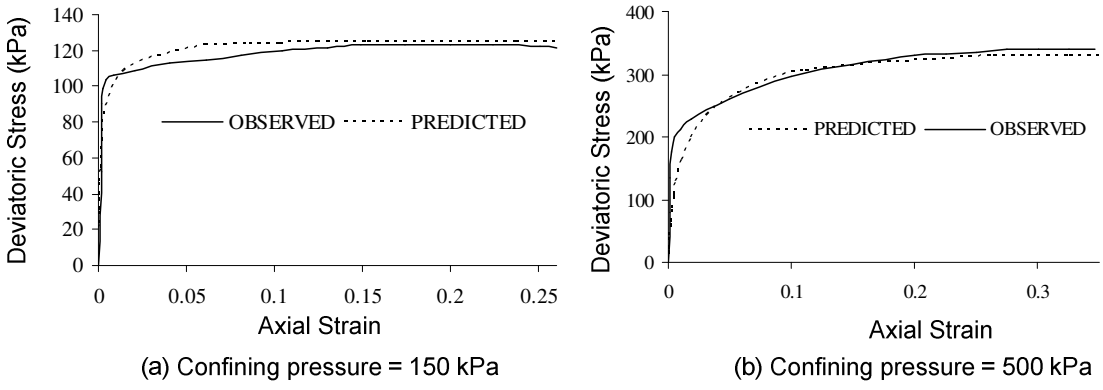

Figure 6.10 Level 2 (Independent) validation results for Sky Pilot till.

In both cases it can be seen that the predictions are in strong agreement with the observed

data. Thus the DSC model can be considered to be capable of successfully characterizing the elastoplastic behaviour of glacial till.

6.9.2 Validation of creep (*evp* and *vevp*) model

Validation of the MDSC model is performed using a 2D finite element program DSC-SST2D (Desai, 1999). The finite element mesh with axis symmetric idealization along with applied loads and boundary conditions is shown in Figure 6.11 Loading is done in two steps. First the confining stress is applied as shown ($\sigma_2 = \sigma_3$). A constant axial stress ($\Delta\sigma_1$) is then applied and kept constant over time. Material properties used for the *evp* and *vevp* analyses are listed in Tables 6.4 and 6.5, respectively.

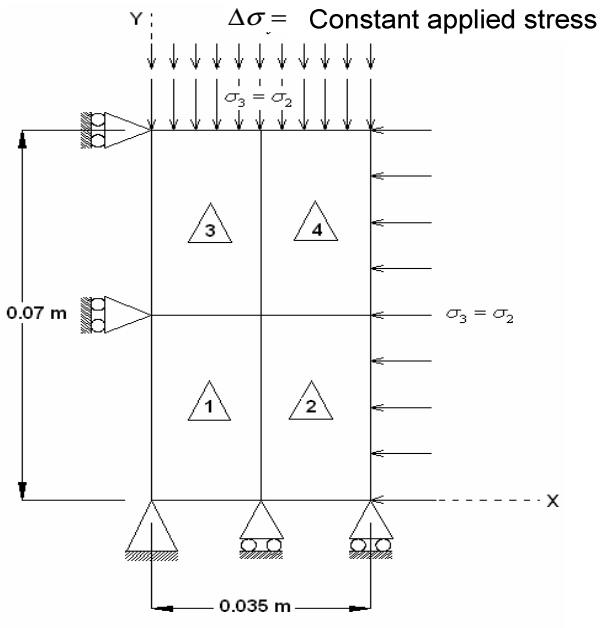

Figure 6.11 FEM mesh, boundary conditions, and loading used for creep predictions.

Figures 6.12 – 6.15 show results of the Level 1 and Level 2 validations for Sky Pilot till.

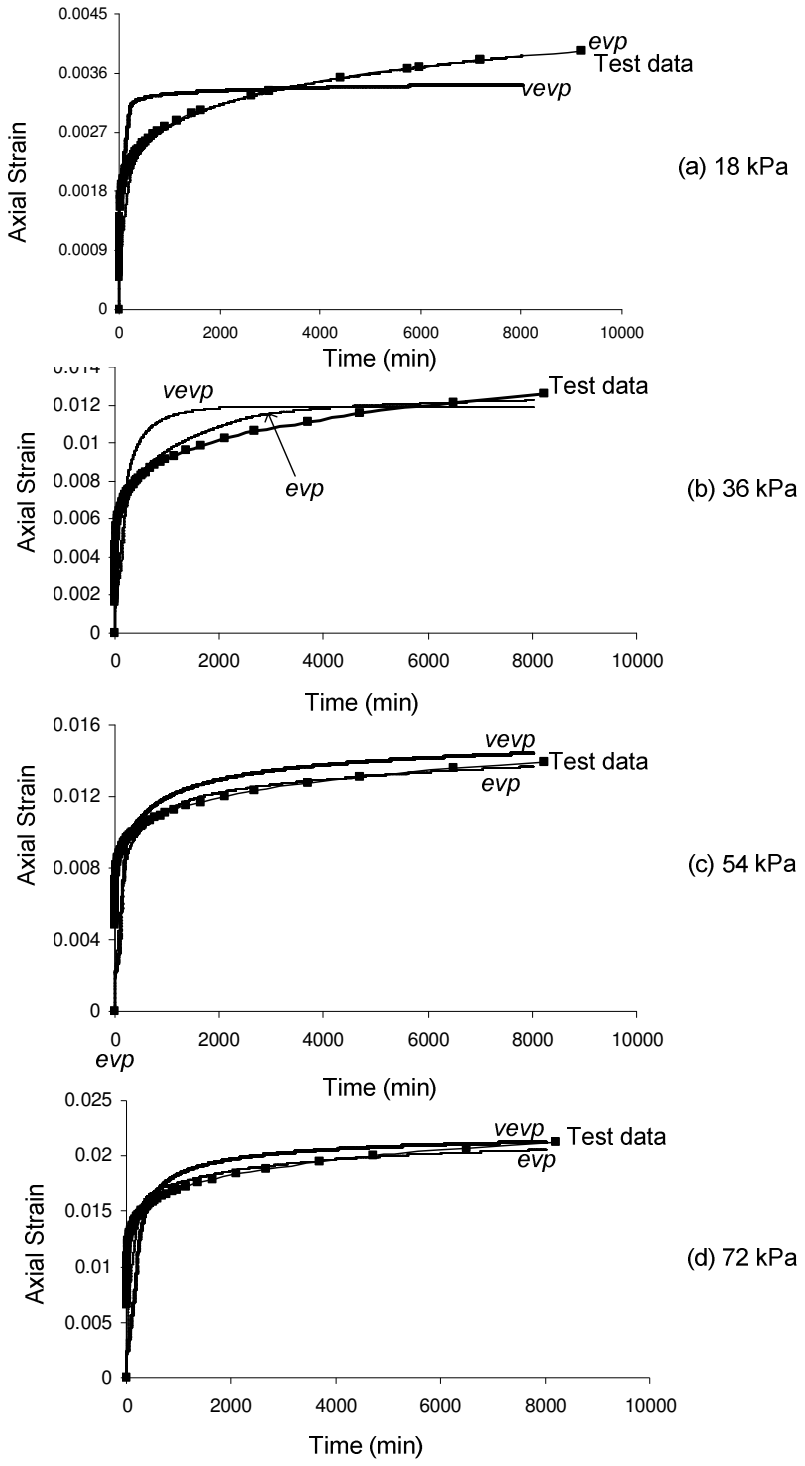

Figure 6.12 Creep model validation at 100 kPa confining pressure (Level 1)

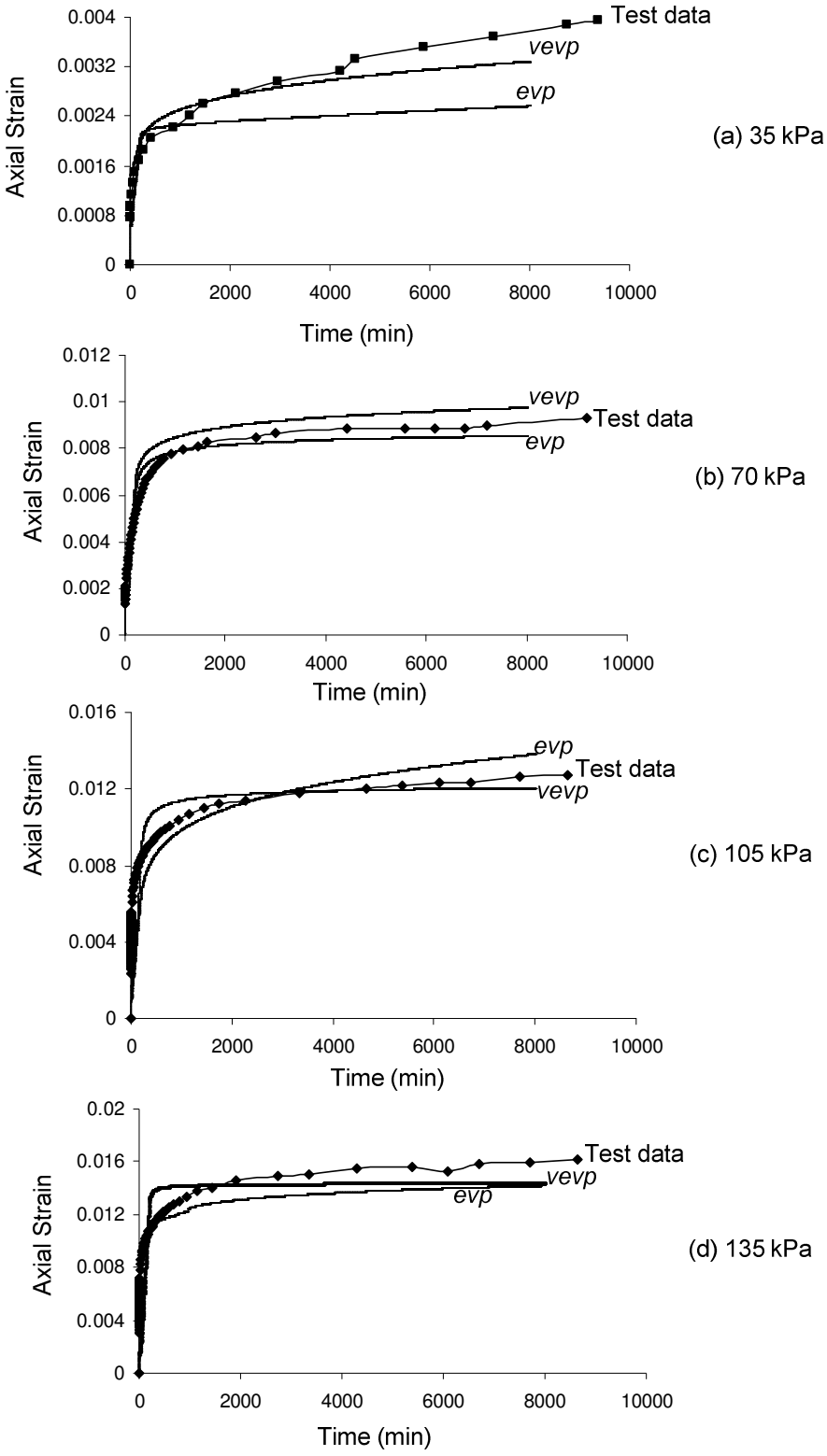

Figure 6.13 Creep model validation at 200 kPa confining pressure (Level 1)

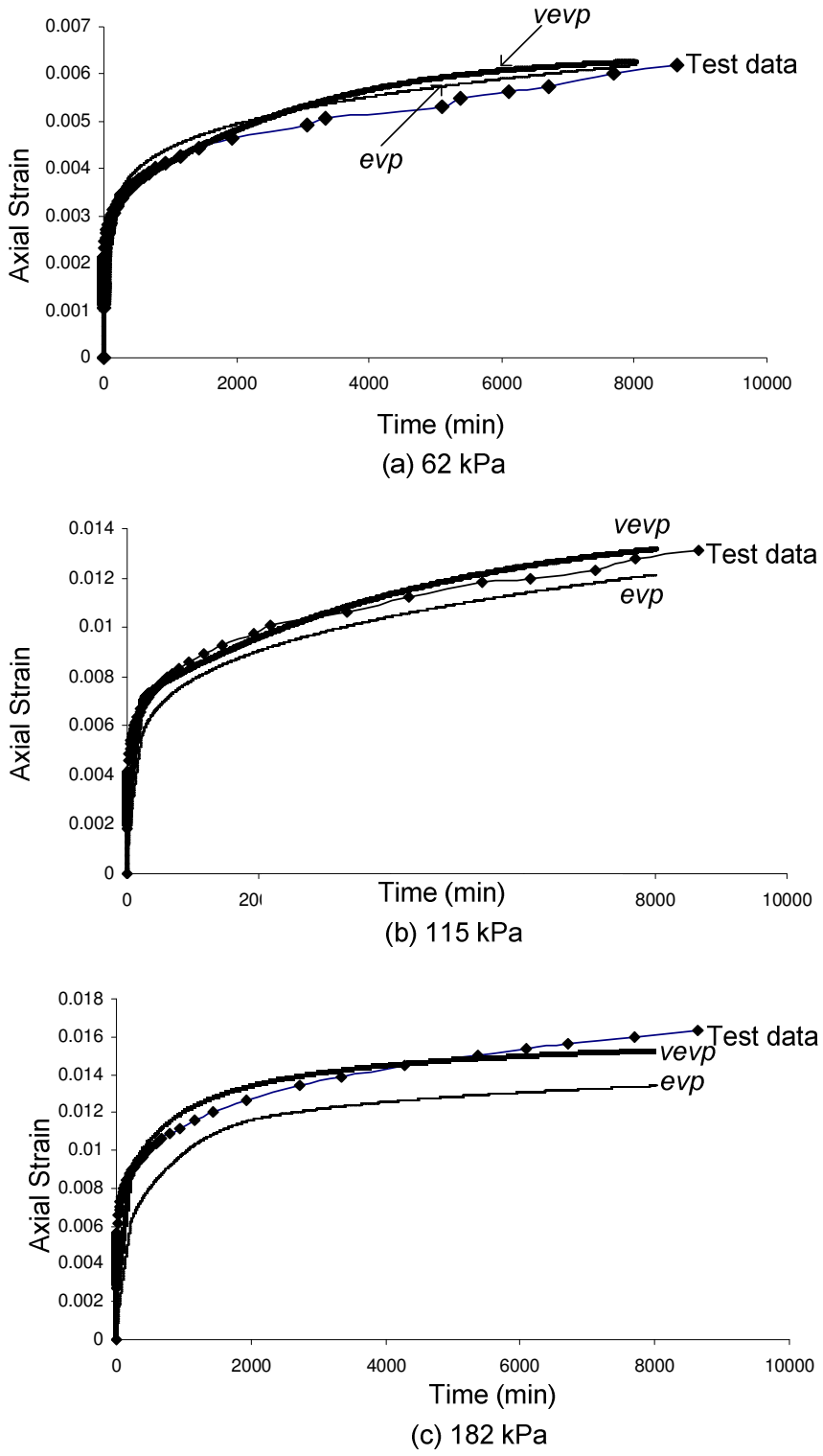

Figure 6.14 Creep model validation at 400 kPa confining pressure (Level 1)

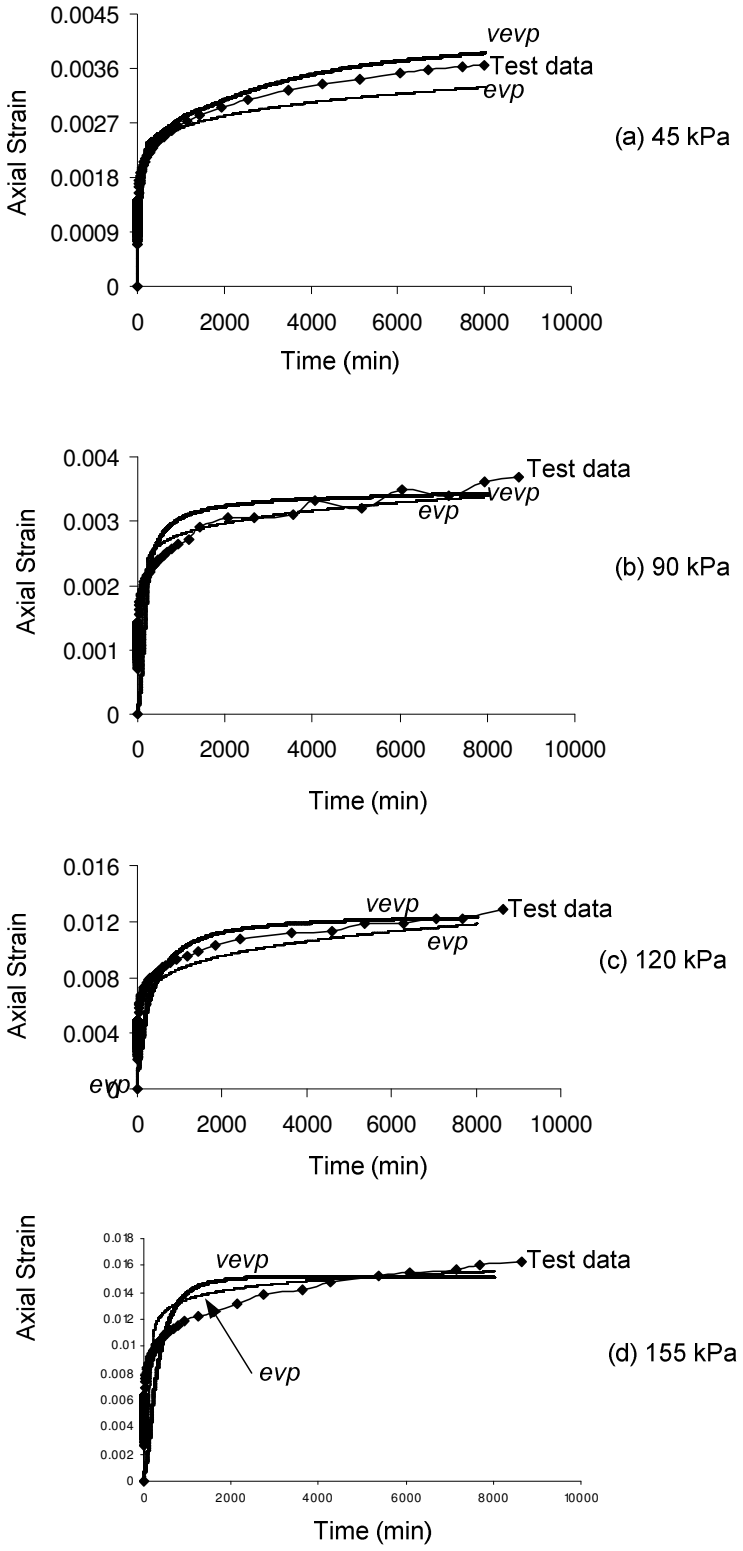

Figure 6.15 Creep model validation at 300 kPa confining pressure (Level 2)

A comparison of predictions performed by *evp* and *vevp* versions of MDSC is plotted in these figures. It can be seen that the predicted curves and test data compare well. The MDSC model can thus be considered to successfully model the creep behavior of glacial tills.

6.9.3 Validation of Rate Dependent Model

Validation the rate dependent model which is proposed and discussed in section 3.3 is presented here. Procedure for performing prediction of rate dependent stress strain curves is described earlier in section 5.5.4.1. Static material parameters for Sky Pilot till at 300 kPa (Table 6.4) are used for the predictions. Figure 6.16 shows results of the rate dependent predictions.

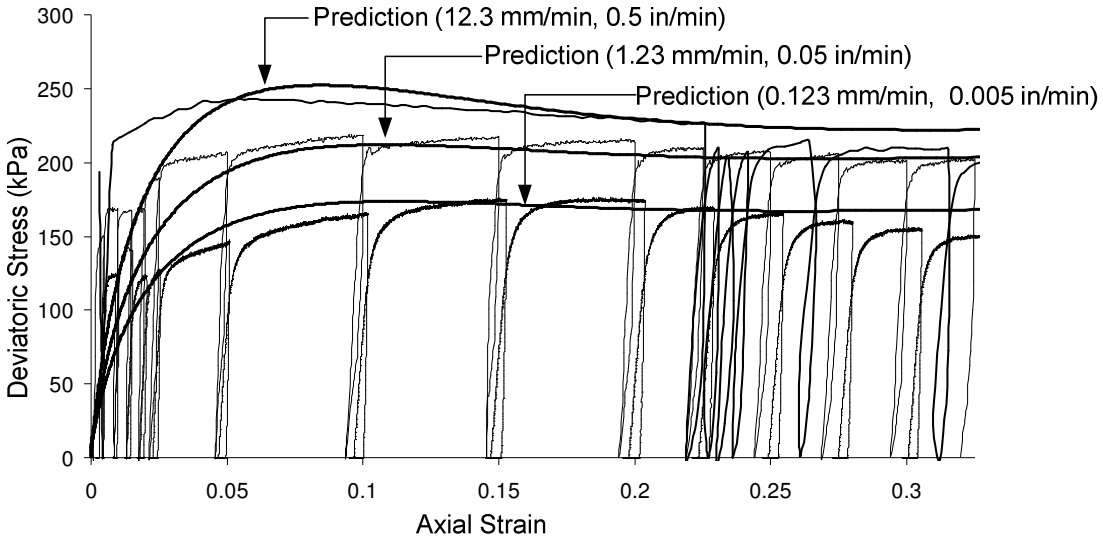

(a) Comparison of predicted and observed rate dependent curves for Sky Pilot till.

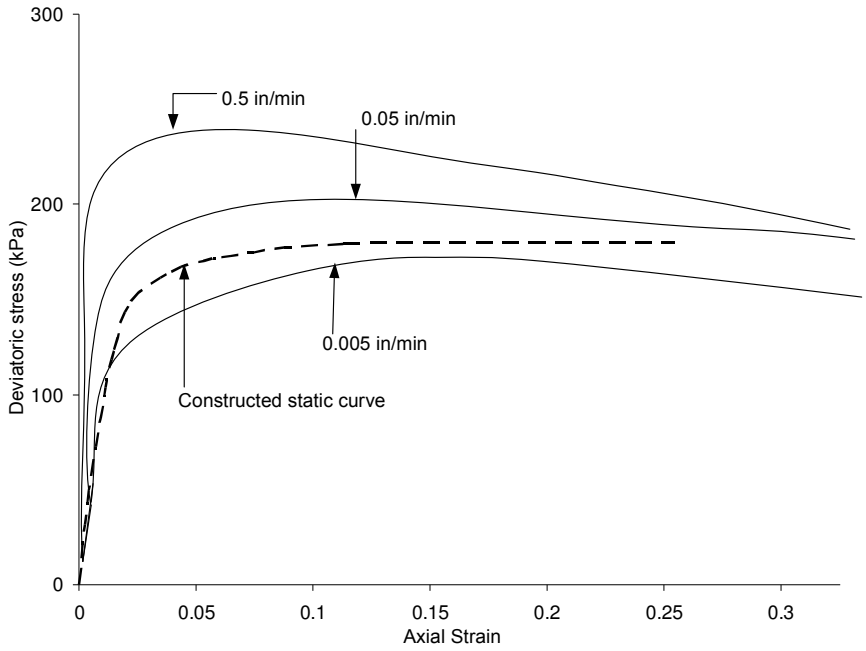

(b) Comparison between constructed static curve and rate dependent tests (smooth curves enveloping the actual test curves are used for clarity).

Figure 6.16 (continued) Validation of rate dependent model

It can be seen that the predictions are in reasonable agreement with the test data for three tests shown. Figure 6.16 (b) shows the comparison between the constructed static curve and test curves at three strain rates. It can be seen that the test at 0.005 in/min is very close to the static curve indicating that 0.005 in/min may be the static rate for Sky Pilot till.

An important observation here is that the rate dependent model has been successfully applied along with disturbance model. Thus the degradation in the material and effect of rate of loading can be modeled successfully by using the same model.

6.10 Numerical (FEM) simulation of an idealized physical system

Based on the results of the validations presented in the previous section, the DSC model can been considered to be capable of modeling the mechanical behavior of glacial tills. The DSC can thus be applied for solving boundary value problems involving mechanical behavior of tills.

In this section, a numerical simulation of an idealized (hypothetical) system consisting of ice and till is performed. A finite element method based numerical program called DSC-SST2D in which the DSC has been implemented is used for the simulation. Following sections describe various steps in the analysis followed by results and discussions.

6.10.1 Problem geometry and FEM mesh

The simulated section and idealized FEM mesh with applied loading is shown in Figure 6.17. Ice is not modeled for the analysis. The FEM mesh is used to model the till layer that is 1.5 m thick. The length of the till section is decided as discussed in the next section. Table 6.6 shows the geometrical details and physical properties used for the analysis.

Plane strain analysis is carried out by discretizing the domain into 4000 elements. Deforming sediment under the ice is assumed to be made of the Tiskilwa Till whose properties are given in Table 6.3. Two analyses, one using DSC/HISS model with plasticity, and the second using Mohr-Coulomb model, are performed. The analysis with Mohr Coulomb model is performed to compare the difference in two approaches. The comparison is discussed along with the results

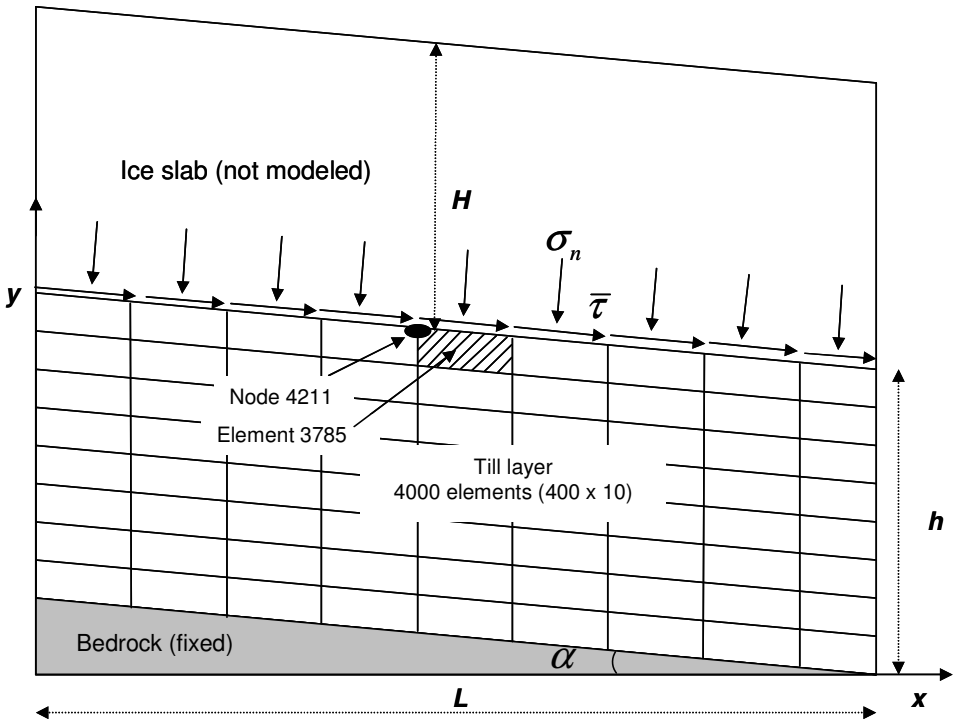

Figure 6.17: Simulated section of ice sheet on till and idealized finite element mesh with loading. (Not to scale.)

Table 6.6: Geometric details and physical parameters for FEA analysis of idealized field problem

Quantity (Symbol)	Value / Unit
GEOMETRICAL PARAMETERS	
Height of till layer (h)	1.5 m
Length along the direction of motion (L)	1000, 5000, 10000 m
Bed angle (α)	4º
Average Ice thickness (H)	100 m
PHYSICAL PROPERTIES OF ICE AND TILL	
Density of the till (ρ_t)	2000 kg·m^{-3}
Density of ice (ρ_{ice})	900 kg·m^{-3}

6.10.2 Boundary conditions

The nodes in the bottom row are fixed to simulate the rigid glacier bed (Figure 6.18). Sides are restrained in y direction as shown since the motion occurs predominantly in x direction.

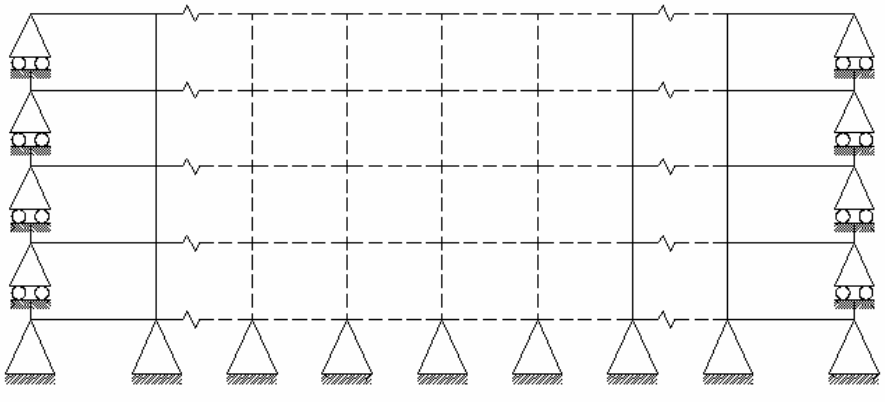

Figure 6.18 Boundary condition at the base and on the sides.

6.10.3 Applied loading and *in situ* stresses

Figure 6.19 shows the applied loading and *in situ* stresses in the till. The analysis is based on the effective stress theory (Holtz and Kovacs, 1981). The pore water pressures are calculated and are subtracted from the total stress values. In this analysis, it is assumed (Iverson and Iverson, 2001) that the pore water pressure developed is 90% of the total ice weight. The *in situ* stress vector $\underset{\sim}{\sigma}_0$ is computed at the mid height of the till layer (y = h/2) as shown below:

$$\underset{\sim}{\sigma}_0 = [\sigma_{x0} \;\; \sigma_{y0} \;\; \tau_{xy0}]^T \tag{6.1}$$

where

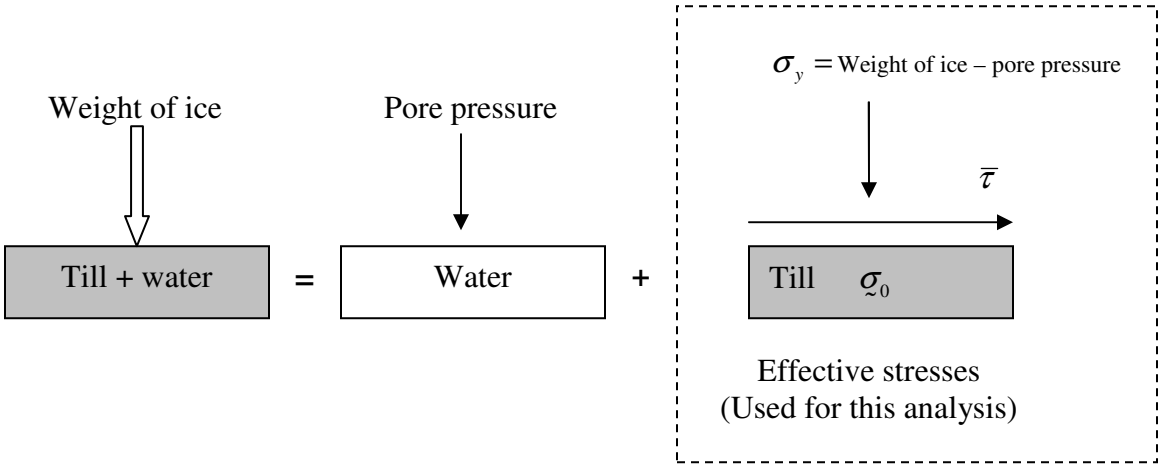

Note: Bed angle is not shown.

Figure 6.19 Applied loading and *in situ* stresses.

$$\sigma_{x0} = K_0 \sigma_{y0} \tag{6.2}$$

$$K_0 = 1 - \sin\phi' \tag{6.3}$$

$$\sigma_{y0} = 0.10(\rho_{ice}.g.H) + \rho_t.g.(h/2) - \rho_w g(h/2) \tag{6.4}$$

$$\tau_{xy0} = 0 \tag{6.5}$$

where the subscript '$_0$' denotes initial stresses, K_0 is the coefficient of lateral earth pressure (computed to be 0.55 from Equation 6.3), ϕ' is the effective angle of friction (27º for Tiskilwa till), u is the pore water pressure, ρ_{ice} is density of ice, ρ_w is the density of water, g is gravitational acceleration, H is the average ice thickness, ρ_t is density of till and h is the height of the till layer. The initial shear stress (Equation 6.5) is assumed to be zero since the surface is approximately horizontal.

Shear stress $\bar{\tau}$ and normal stress σ_n at the interface of the ice and till (Figures 6.17 and 6.19) are applied. These stresses are calculated as (Hooke, 2005)

$$\sigma_n = 0.10(\rho_{ice} g H) \tag{6.6}$$

$$\bar{\tau} = \rho_{ice} g H \alpha \tag{6.7}$$

where α is the bed angle in radians (Figure 6.17). These stresses are applied at the top nodes, in 100 increments in the finite element analysis.

6.10.4 Selection of length of the simulated section

It is observed that the boundary conditions on the sides of the mesh affect the results of the analysis. To avoid such an effect the boundary should be at sufficiently greater distance from the mid-section of the mesh. To decide the optimum length for the mesh, three different trials, L = 1000 m, 5000 m and 10000 m, are conducted with 400 elements. It is expected that each section (across the length) of the till, except few sections near the sides, will behave in similar manner since the length of the ice sheet is very long in the field.

Figure 6.20 shows computed distributions of disturbance, D, at failure, which is approximately defined at τ = 60 kPa at which the majority of the till zone has experienced assumed critical disturbance of D_c = 0.85 (Figure 6.20). It is observed that an increase in length from 1000 m to 5000m has significant effect in the disturbance

contours. However, increasing the length from 5000m to 10000m does not produce any significant difference and the disturbance contours are essentially the same. Thus the length L = 5000 m is chosen to be the optimum length. The subsequent (final) analysis is then performed with 4000 elements and at L = 5000 m.

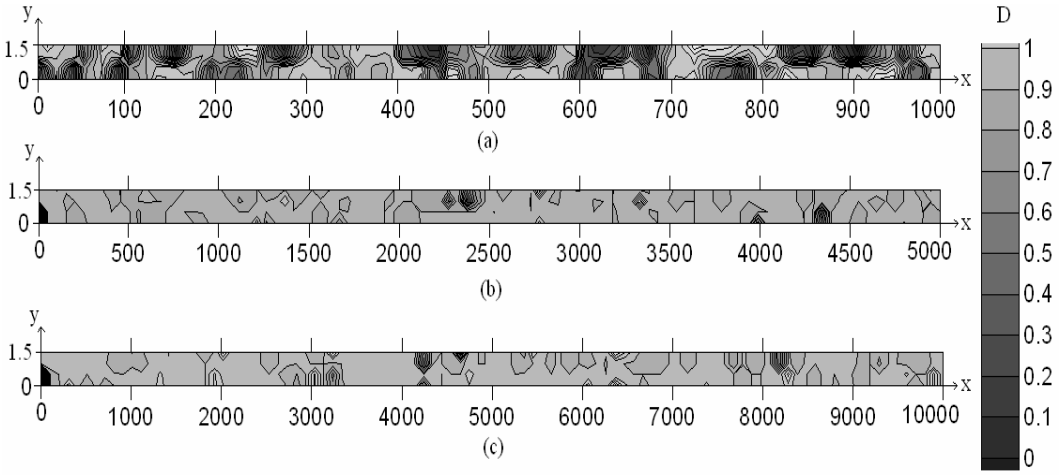

Figure 6.20 Selection of length of simulated section (400 elements) based on disturbance contours for (a) L = 1000 m (b) L = 5000 m (c) L = 10000 m at $\bar{\tau}$ = 60 kPa

6.10.5 Analysis results

This section discusses the results of the analyses performed using the DSC model as well as the Mohr Coulomb model. Figure 6.21 shows the distribution of computed disturbance in the middle 1000-m segment of the 5000-m domain (i.e., from x = 2000 to 3000 m) of the till layer during the incremental application of shear stress, $\bar{\tau}$, from 0 to 65 kPa. It can be seen that the disturbance grows from very small value to greater than the critical disturbance, D_c = 0.85, around the applied stress, $\bar{\tau}$, of about 60 kPa between

55 and 65 kPa. Figures 6.21 (b) and (c) show the variation of induced shear stress τ_{xy} (internal shear stress) developed vs. shear strain, γ_{xy} in an element at the ice till interface near the top mid-section for the DSC and Mohr-Coulomb models, respectively. τ_{xy}, γ_{xy}, and D increase gradually with the applied shear stress. The induced shear stress, $\tau_{xy,}$ reaches a peak value at about 60 kPa in the DSC/HISS model, and then decreases. The critical disturbance, D_c, at which the failure causing the ice slab motion is assumed to occur, is observed in the post-peak zone at induced shear stress of $\tau_{xy} \approx 23$ kPa, and shear strain, $\gamma_{xy} \approx 0.75$ (Figures 6.21 b and 6.22 a).

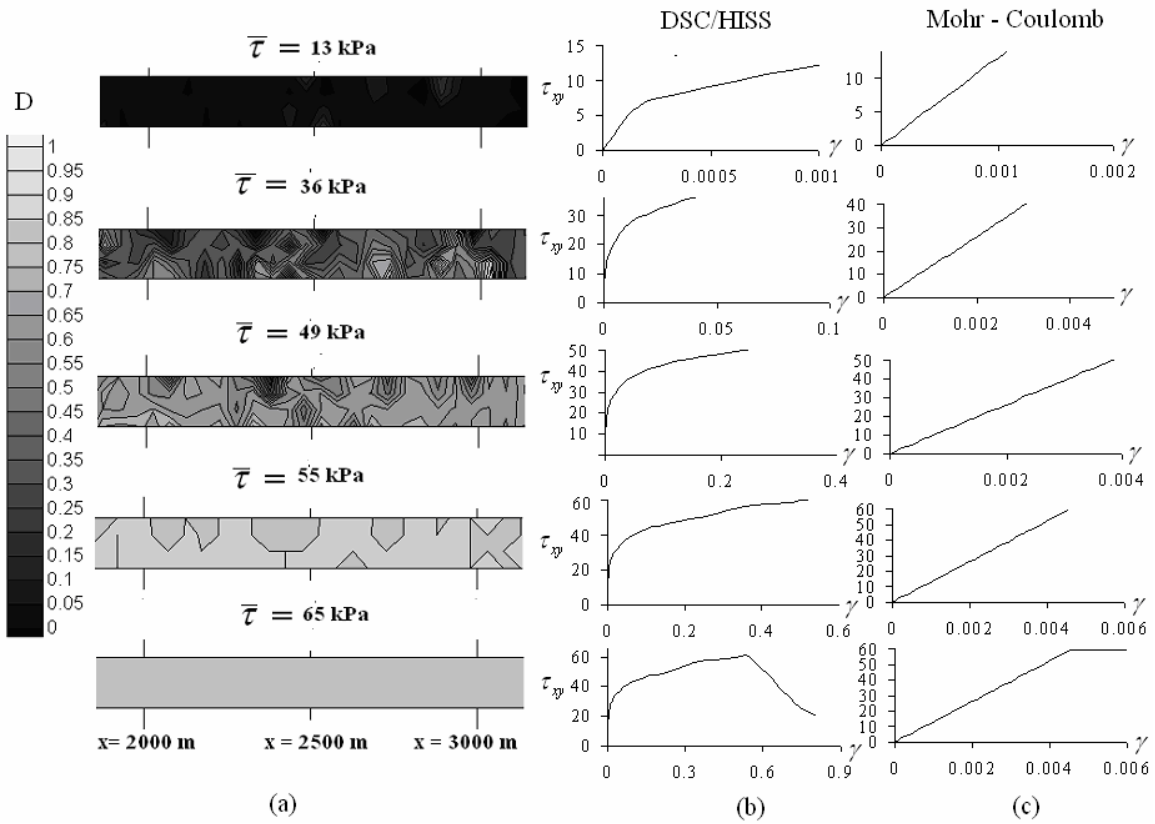

Figure 6.21 (a) Contours of disturbance in the central 1000-m section from DSC/HISS model at intermediate increments of external applied loading and shear stress-shear strain curves from (b) DSC/HISS model (c) Mohr-Coulomb model.

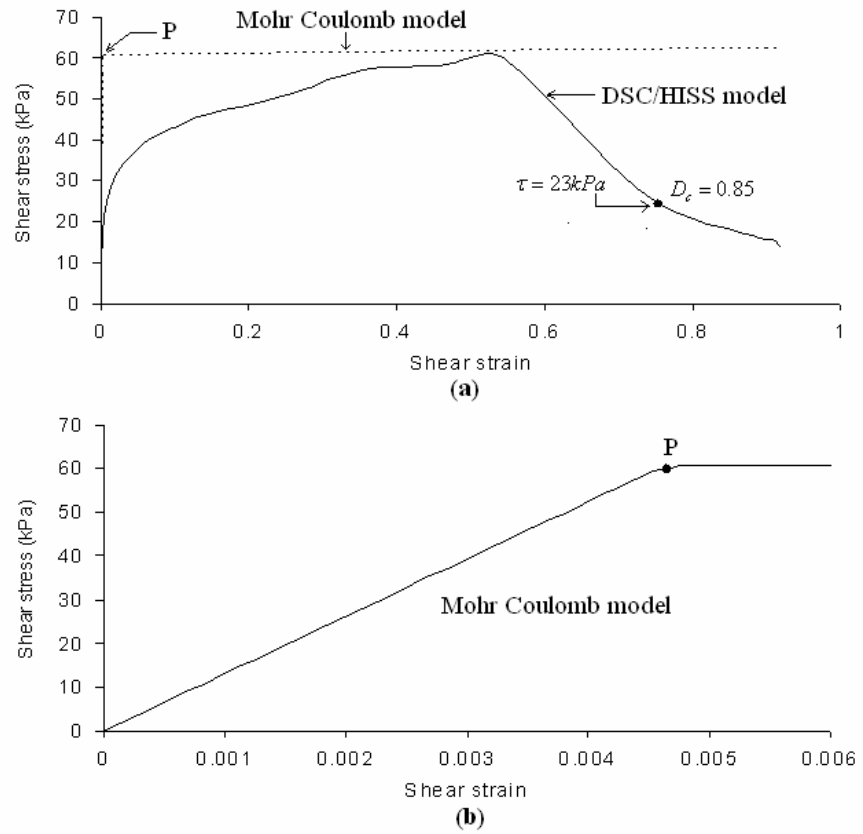

Figure 6.22 Comparison between mechanism of "failure" in DSC/HISS and Mohr-Coulomb model. (a) Typical stress-strain behavior with DSC/HISS model and Mohr-Coulomb model: element No. 3745 (x = 2500 m, y = 174.81 m). (b) Enlarged stress-strain response from Mohr-Coulomb model in region, strain = 0 to 0.006.

On the other hand, the strains computed from the Mohr-Coulomb model are very small, and failure at the peak stress of about $\tau_{xy} \approx 62$ kPa occurs at elastic shear strain of about $\gamma_{xy} \approx 0.0048$ (Figures 6.21 c and 6.22 b).

Figure 6.23 shows growth of horizontal displacement over the height of the till section predicted by the two models for various applied stresses. In the DSC model, displacement of about 4.5 m occurs at the applied $\bar{\tau}$ = 65 kPa. On the other hand, for the

Mohr-Coulomb model, failure takes place at about τ_{xy} = 60 kPa, Figure 18 (b), at very small shear strain ($\gamma_{xy} \approx 0.0048$). Moreover, after failure (i.e., after $\gamma_{xy} \approx 0.0048$) the displacements are very large, of the order of about 16 m, i.e., catastrophic (Figure 19 b).

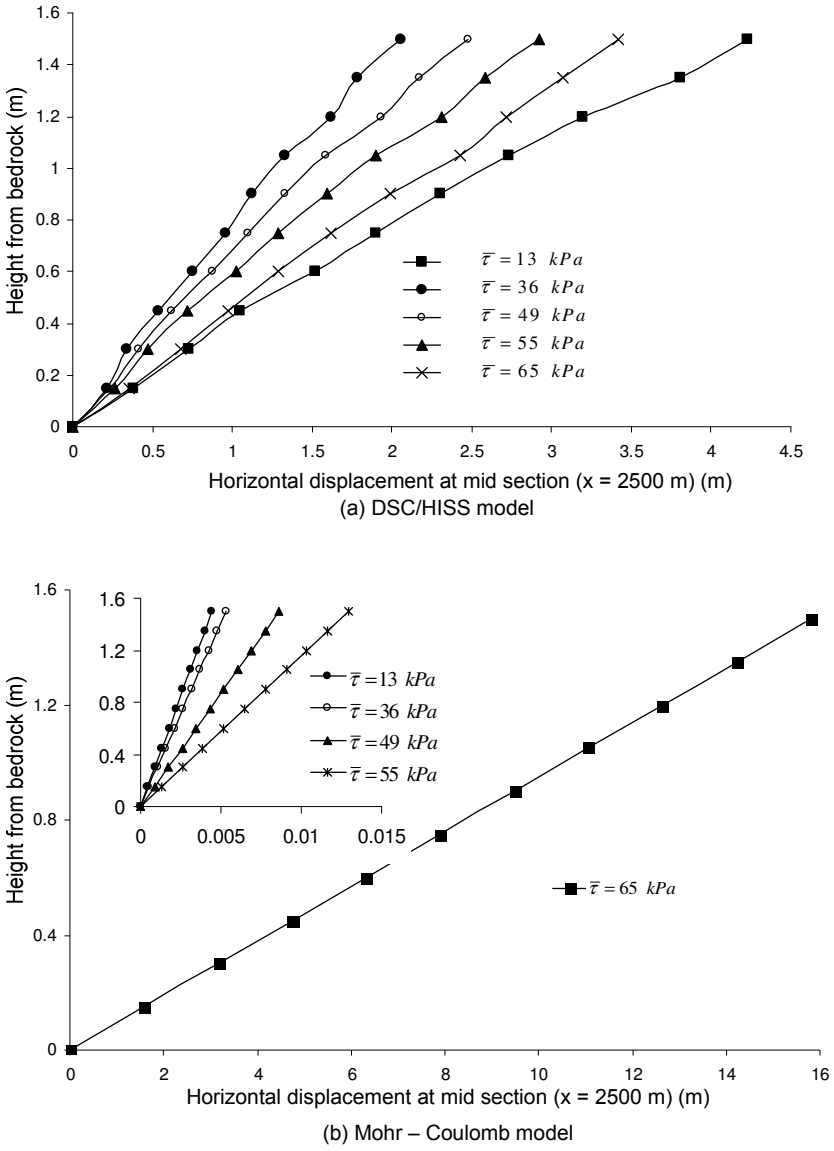

Figure 6.23 Horizontal displacement at mid-section (x = 2500 m) predicted from (a) DSC/HISS model and (b) Mohr-Coulomb model.

6.11 Comparison between the Mohr-Coulomb and DSC models.

In the previous section, the DSC and Mohr Coulomb models are compared based on the results of the numerical simulation. Here a more fundamental comparison between the two approaches is presented.

Mohr Coulomb model, which has been widely used to model the mechanical behavior of glacial tills, assumes linear elastic behavior of the till upto the peak stress. After the peak, catastrophic failure is predicted. This is mainly due to the fact that the failure is defined based on only one factor, stress.

The DSC considers the material to behave in elastoplastic manner from the onset of loading. Thus plastic strains are considered before and after the peak. Also, disturbance in the material is another factor used to characterize the failure. The DSC assumes failure when a significant mass of the material reaches critical disturbance. Thus the overall failure definition is based on stresses, plastic strains and disturbance. Thus the DSC can be considered to define the failure in a more detailed and fundamental manner as compared to the Mohr Coulomb model. Following illustration based on the CTC test results of Tiskilwa till further supports this statement.

Figures 6.24 (a) and (b) show the disturbance versus total and plastic (deviatoric) strains, respectively, from a CTC test on Tiskilwa Till at σ'_3 = 100 kPa. The Mohr-Coulomb model assumes that the till would deform elastically up to the peak stress (which occurs in this test at about 0.1 total strain). At the peak stress, failure is predicted by Mohr Coulomb model, inducing sudden motion and infinite strain. If a hypothetical definition of disturbance, D, dependent on accumulated plastic strains is assumed then D is zero until peak and it jumps to unity just after peak (Figure 6.24 a) and it is equal to unity throughout plastic strain (Figure 6.24 b).

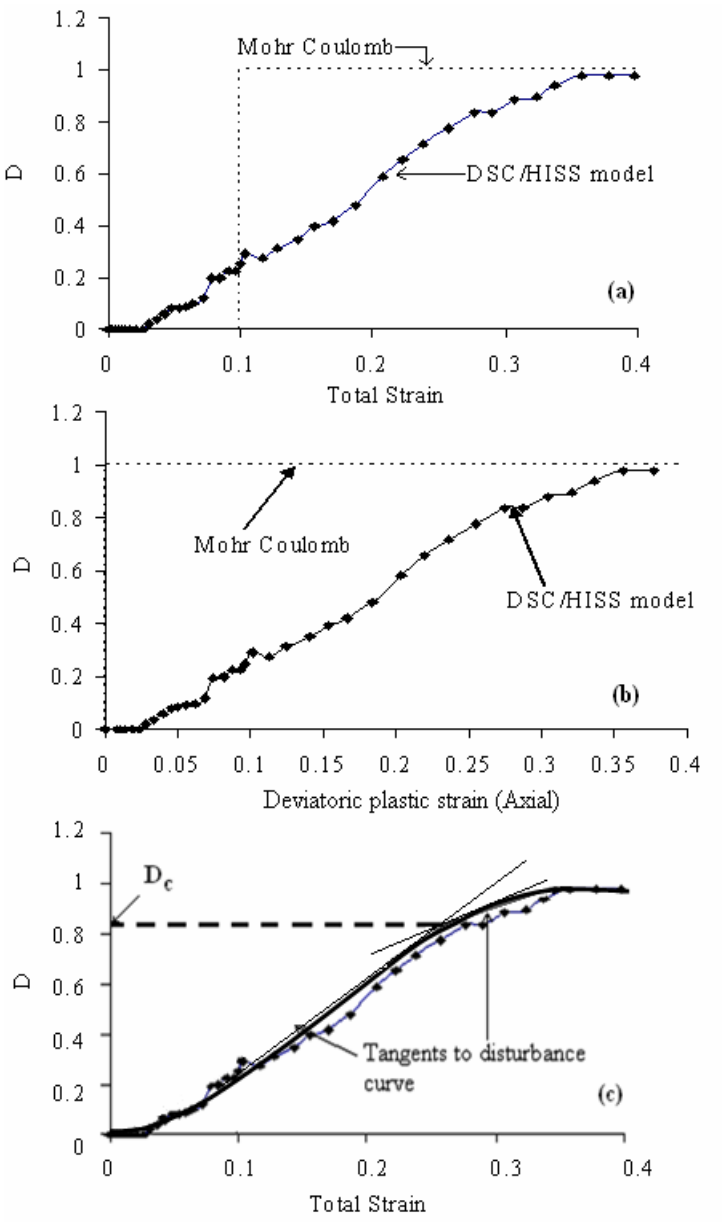

Figure 6.24 (a) Disturbance vs. total strain (b) Disturbance vs. plastic strain (c) computation of critical disturbance, D_c. Calculation is based on laboratory CTC test results on Tiskilwa till at $\sigma_3' = 100$ kPa.

The test data and DSC, however, show that plastic strain (Figure 6.24 b) begins well before the peak stress is reached. It then increases as D approaches its limiting value

of unity. The intersection of the tangents to the early and later parts of the disturbance curve (Figure 6.24 c) locates the critical disturbance, $D_c = 0.85$, at which sufficient mass of the material has approached the FA or critical state. This compares very well with the finite element prediction in which failure and initiation of the motion is assumed to occur at about $D_c = 0.85$ (Figure 18 a).

Thus when the DSC model is used, the failure and motions are predicted to occur when the disturbance reaches the value $D_c = 0.85$, Figure 6.24 c, in about 85 percent of the volume of the till at the total strain of about 0.3 and plastic strain of about 0.27. In contrast, failure and motion with Mohr-Coulomb model occurs at the total strain of about 0.1 and plastic strain zero.

Another fundamental difference in the two approaches is the failure location. The Mohr-Coulomb model assumes the failure to occur along distinct shear planes developed in the material around the peak stress. The DSC on the other hand does not assume any such predefined or preferred failure locations.

The triaxial tests on the Tiskilwa and the Sky Pilot tills indicate no preferred shear or failure planes. In fact, the samples deform continuously and the failure appears to take place when the critical strains (disturbance) occur at distributed locations in the specimen. Photographs of typical samples at failure are shown in Figure 6.25. It can be seen from the pictures that no preferred shear planes or distinct failure zones are observed. Hence, it may be concluded that the failure in the tills, and the relative motion of the ice sheets take place when a critical volume of the material reaches a critical state ($D_c = 0.85$), i.e., when about 85% of the total material reaches failure.

Thus the DSC model can be considered to provide a more realistic description of failure and motion in glacial till compared to that by the Mohr-Coulomb model.

Figure 6.25 Photographs of CTC test samples (a) before the test, and (b), (c), (d) after test: (b) for Sky Pilot, and (c) and (d) for Tiskilwa till.

6.12 Proposed DSC criterion for failure and motion

According to the DSC, failure and resulting motion take place when $D_c \approx 0.85$, i.e., when about 85% of the total mass reaches critical state. The till thus fails under a post-peak induced stress much lower than the peak stress, and at much higher strain involving considerable plastic strain. The parts in the FA (critical) state are distributed

over the entire laboratory specimen (Figure 6.25). We illustrate this criterion in Figure 6.26. Figure 6.26 (a) shows the displacement at the top mid section node of the finite element mesh vs. applied shear stress, $\bar{\tau}$. It can be seen that the displacement increases gradually at approximately constant rate until after the peak induced stress of $\tau_{xy} \approx 60$ kPa. Induced shear stress then declines rapidly, and at around the point at which the induced stress $\tau_{xy} \approx 23$ kPa, and $D_c \approx 0.85$ is reached, a sudden increase in the rate of growth of displacement is observed. Figure 6.26 (b) shows the accumulated plastic strain, ξ, vs. applied axial strain for the laboratory test on the Tiskilwa Till at $\sigma'_3 = 100$ kPa. It can be seen that at $\xi \approx 0.33$ with $D_c \approx 0.85$, the rate of increase of ξ increases. These laboratory data thus support the computer predictions from Figure 6.26 (a). These results indicate that the failure and resulting motion occur when the entire soil mass has reached the critical condition defined by stress, strain and the accumulated plastic strain.

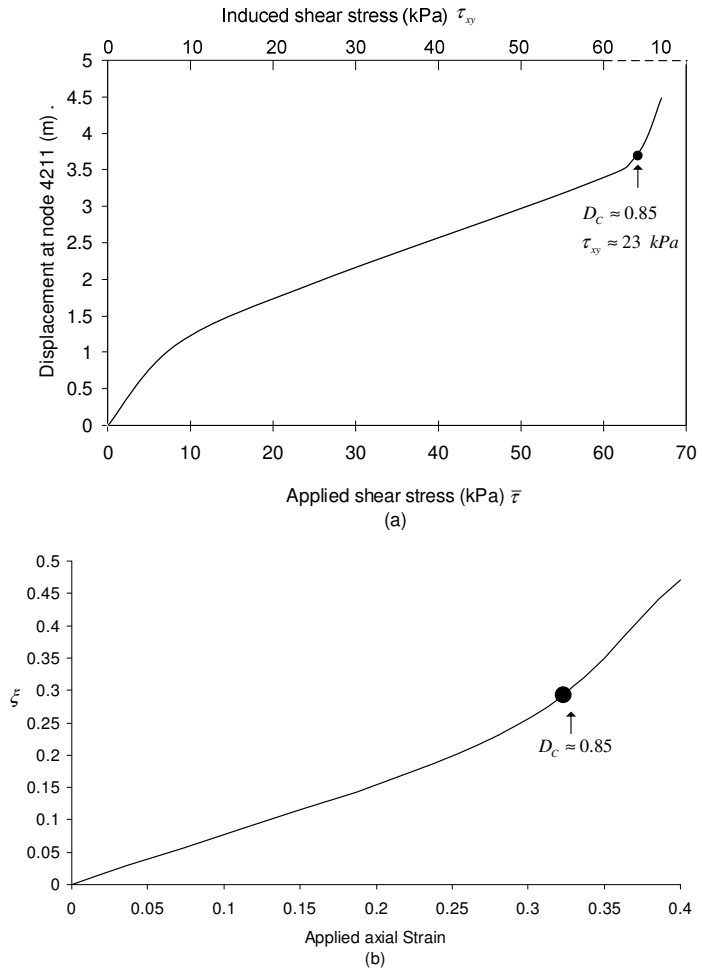

Figure 26. (a) Rate of change of displacement with applied stress predicted by FEA. (b) Rate of change of ξ with applied strain for CTC test on Tiskilwa till at σ'_3 = 100 kPa. Note: After the induced peak shear stress = 60 kPa, it reduces to about 10 kPa in the post peak region, which is indicated by the dotted line in Figure 32a.

6.13 Conclusions

Conventional plasticity models such a Mohr-Coulomb criterion may not predict the behavior of glacial tills in a realistic manner. Here a general and unified model based on the disturbed state concept (DSC) is presented which represents the behavior of tills based on combination of stress, plastic strain and an internal variable called disturbance

expressed in terms of accumulated plastic strains. This approach yields a realistic and holistic model in which the glacier motion is shown to initiate beyond the peak stress when the behavior approaches the residual state at which the critical disturbance is reached. We have identified the critical state based on comprehensive laboratory tests and computer analysis of a simulated physical system involving ice sheet and glacial till. Based on the research presented herein we believe that the DSC model provides a unified and improved model for prediction of glacial motion. Furthermore, our approach provides a framework which can be consistent with the concepts presented by Clarke (2005) and Hindmarsh (1997).

The overall behavior and motion of the ice sheets may be influenced by sliding, ploughing, and possible "sticky spot" mechanisms. We believe that the DSC is capable of accounting for such combination of behaviors, and ultimately provides the basis for a realistic global model for predicting ice sheet motion.

CHAPTER 7

CONCLUSIONS AND SIGNIFICANT NEW CONTRIBUTIONS

7.1 Conclusions of the research

In this research the DSC model has been applied to problems in electronic packaging and glacial mechanics. In both cases, the DSC has been shown to provide better understanding of the material behavior leading to successful development of a procedure for life prediction of electronic packages, and a failure and motion criterion for prediction of ice sheet motions.

A procedure for material creep modeling based on the MDSC approach is applied to the solder alloys and glacial tills. Necessity of using static yield surface for modeling creep behavior using *evp* model is identified. A new procedure to define the static yield surface based on creep tests is also proposed. A modification to current HISS model, to include the effect of strain rate on material behavior has been proposed. Validations for the proposed procedures are also presented.

7.2 Significant new contributions from this research

List of significant new contributions from this research is presented below. It is divided into two parts,

- Contributions towards electronic packaging problem.
- Contributions towards prediction of glacial motion.

- Electronic Packaging
    1. DSC has been successfully applied for modeling SAC (lead free) solder alloys.
    2. Need for using static yield function when MDSC applied for creep modeling.
    3. New method for construction of static curves based on creep tests is proposed.
    4. A rate dependent model is proposed and applied successfully to SAC lead free alloy.
    5. A numerical procedure for rate dependent stress-strain predictions is developed in MATLAB.
    6. Proposed rate dependent model with the procedure for construction of static curves is validated.
    7. The accelerated procedure developed by Whitenack (2004; Desai and Whitenack (2001)) is successfully applied for prediction of number of cycles to failure for the SAC alloy.
    8. An approximate failure criterion for BGA 225 is derived.
- Prediction of glacial motion
    1. The DSC is applied to model the mechanical behavior of glacial tills.
    2. A series of CTC and creep tests are performed on the till samples collected from the field for both tills. Rate dependent tests on Sky Pilot till are also performed.
    3. DSC parameters are obtained from test results for model calibration.
    4. Proposed rate dependent model and procedure for construction of static curve has been applied and validated for glacial tills.
    5. Comparison of the DSC to Mohr Coulomb model is performed based on the results of a numerical simulation and test data.

6. A failure and motion criterion for glacial tills is developed for prediction of motion of ice sheets and glaciers.

7.3 Conclusion

The DSC has been shown to provide much improved and realistic framework for material modeling in two significantly different areas of engineering. Thus the DSC is capable of successfully modeling a wide range of engineering materials. This generality of the model makes it arguably one of the most advanced unified material models available.

REFERENCES

Baladi, G.Y., Rohani, B., 1984, *"development of an Elastic Viscoplastic Constitutive Relationship for Earth Materials"*, Chapter 2 in "Mechanics of Engineering Materials", John Wiley and sons Ltd, Edited by Desai, C. S. and Gallagher, R.H. ,pp 23 - 43

Bell, F.G., 2002, *"Geotechnical properties of some till deposits occurring along the coastal areas of eastern England.",* Engineering Geology, 63: 49-68.

Boulton, G.S. and Jones, A.S., 1979, "*Stability of temperate ice sheets and ice caps resting on beds of deformable sediment.*", Journal of Glaciology., 24: 29-43.

Carlson, A.E., Jenson, J.W. and Clark, P.U., in press., "*Field observations from the Tiskilwa Till, IL, and Sky Pilot Till, MB of the Laurentide Ice Sheet*"., Geographie Physique et Quaternaire.

DeMaggo, F.L. and Sandler, I., 1971, "*material model for granular soils",* Journal of Engineering Mechanics, ASCE, 97 – 3, pp 935 – 950.

Desai, C.S., Somasundaram, S. and Frantziskonis, G.N., 1986, *A Hierarchical Approach for Constitutive Modelling of Geologic Materials*". International Journal of Numerical and Analytical Methods in Geomechanics., 10: 225-257.

Desai, C.S. and Toth, J., 1996, "*Disturbed State Constitutive Modelling Based on Stress-Strain and Nondestructive Behavior*", International Journal of Solids and Structures, 33: 1619-1650.

Desai, C.S., 2000, "*User Manual- DSC-SST2D, Computer code for Static, Dynamic, Creep and Thermal Analysis: Solid, Structure, and Soil- Structure Problems, Part- 1, 2 and 3*", Version 2, Tucson, Arizona, USA.

Desai, C.S., 2001, "*Mechanics of Materials and Interfaces: The Disturbed State Concept*". CRC Press, Boca Raton, Florida.

Desai C.S. and Whitenack R. D., 2001, "*Review of models and disturbed state concept for thermomechanical analysis in electronic packaging*", Journal of electronic packaging, ASME, 123, pp 19 - 33

Desai, C.S., 2002, "*Code for determinations of material parameters and backpredictions"*, University of Arizona, Dept. of Civil Engineering and Engineering Mechanics, Tucson, Arizona, USA.

Desai, C.S., Wang, Z., Whitenack, R., and Kundu, T., 2004, "*Testing and Modelling of Solders Using New Device: Part I: Models and Testing" and "Testing and Modelling of Solders Using New Device: Part II: Calibration and Validation*," , Journal of Electronic Packaging, ASME, Vol. 126, Issue 2, pp. 232-236

Dongkai, S., 2006, "*Lead Free Solder Interconnect Reliability",* ASM international.

Dredge, L.A. and Nielsen, E., 1985, "*Glacial and interglacial deposits in the Hudson Bay lowlands: a summary of sites in Manitoba*".

Engelhardt, H. and Kamb, B., 1997, "*Basal hydraulic system of a West Antarctic ice stream: constraints from borehole observations*", Journal of Glaciology, 43: 207-230.

Engelhardt, H., Humphrey N., Kamb N., and Fahnestock, M., 1990, "*Physical conditions at the base of a fast-moving Antarctic ice stream".* Science, 248: 57-59.

Hansel, A.K. and Johnson, W.H., 1996, Wedron and Mason Groups, "*Lithostratigraphic reclassification of deposits of the Wisconsin Episode, Lake Michigan area*", Illinois State Geological Survey Bulletin, 104.

Head, K.K., 1986, "*Manual of soil laboratory testing*", Pentech Press, London.

Holtz, R.D. and Kovacs, W.D., 1981, "*An Introduction to Geotechnical Engineering",* Prentice-Hall, Englewood Cliffs, New Jersey, 733 pp.

Hooke, R.L., 2005. "*Principles of Glacier Mechanics*", Cambridge University Press.

Iverson, N.E. and Iverson, R.M., 2001, "*Distributed shear of subglacial till due to Coulomb slip*", Journal of Glaciology, 47(158): 481-488.

Johnson, W.H. and Hansel, A.K., 1990, "*Multiple Wisconsinan glacigenic sequences at Wedron, Illinois*", Journal of Sedimentary Petrology, 60: 26-41.

Kachanov, L.M., 1986, "*Introduction to Continuum Damage Mechanics"*, Martinus Nijhoft publishers, Dordecht, The Netherlands.

Kamb, B., 2001, "*Basal zone of the West Antarctic ice streams and its role in lubrication of the rapid motion. The West Antarctic Ice Sheet: Behavior and Environment*", Antarctic Research Series, 77: 157-199.

Klassen, R.W., 1986, "*Surfacial geology of the north-central Manitoba*". Geological Survey of Canada Memoir, 419: 57.

Lambe, T.W. and Whitman, R.V., 1969, "*Soil Mechanics"*. John Wiley and Sons, Inc., New York, USA.

Lupini, J.F., Skinner, A.E. and Vaughan, P.R., 1981, "*The drained residual strength of cohesive soils*". Geotechnique, 31: 181-213.

Lee, K.O., Jin Yu, T. S. Park and S.B. Lee, 2004, "*Low cycle fatigue characteristics of Sn-based solder joints",*

Mickelson, D.M., Clayton, L., Fullerton, D.S. and Borns, H.W., Jr., 1983, *"The Late Wisconsin glacial record of the Laurentide Ice Sheet in the United States. In: H.E.*

Wright, Jr. (Editor), Late-Quaternary Environments of the United States", University of Minnesota Press, Minneapolis, pp. 3-37.

Nielsen, E. et al., 1986, "*Stratigraphy, paleoecology, and glacial history of the Gillam area, Manitob",* Canadian Journal of Earth Sciences, 23: 1641-1661.

Pande, D.N., Owen, D. R. J. And Zienkiewicz, O. C., 1977, "*Overlay models in Time Dependent Nonlinear Material Analysis",* Computer and Structures, 7, *pp* 435 - 443

Pandey, A., 2005, *"Disturbed state modeling for creep response of subglacial till"*, M.S. Thesis, Department of Civil Engineering and Engineering Mechanics, University of Arizona, Tucson, Arizona, USA.

Perzyna, P., 1966, "*Fundamental Problems in Viscoplasticity*", Advances in Applied Mechanics", 9: 243-277.

Rassaian, M and Lee S, 2007, private communications

Roscoe, K.H., Schofield, A. N., and Wroth, C. P., 1958, "*On the yielding of soils*", Geotechnique, 8, 22-52.

Roy, M., 1998, "*Pleistocene stratigraphy of the lower Nelson River area-implications for the evolution of the Hudson Bay lowland of Manitoba, Canada*". M.S. Thesis, University of Quebec, Montreal, 220 pp.

Samtani, N.C., Desai, C. S. And Vulliet, L., "*Contitutive Modeling and Analysis of Creeping Slopes"*, 1995, Journal of Geotechnical engineering, ASCE, 121, pp 43 – 56

Sane, S.M., Desai, C. S., Jenson, J. W., Contractor, D. N., Carlson A. E., and Clark, P.U., 2007, "*Disturbed State Constitutive Modeling of Two Pleistocene Tills"*, article in press, Quaternary Science Reviews.

Skempton, A.W., 1985, "*Residual strength of clays in landslides, folded strata, and the laboratory*". Geotechnique, 14: 75-101.

Syed, A., 2001, "*Reliability of Lead-Free Solder Connections for Area-Array Packages*", conference proceedings, IPC SMEMA council APEX.

Thorleifson, L.H., Wyatt, P.H., Shilts, W.W. and Nielsen, E. (Editors), 1992, "*Hudson Bay Lowland Quaternary stratigraphy: evidence for early Wisconsinan glaciation centered in Quebec. The Last Interglacial-Glacial Transition in North America",* Special Paper 270. Geological Society of America, 207-222 pp.

Tummala, R.R., and Rymazzewski E. J., 1989, "*Microelectronic Packaging Handbook",* Van Nostrand Reinhold, New York

Vianco, P.T., Regent, J.A. and Kilgo, A. C., 2003, "*Time - independent mechanical and physical properties of the ternary 95.5 Sn3.9Ag0.6Cu solder*", Journal of electronic materials, V32 - 3, pp 142 - 151.

Whitenack, R.D., (2004), "*Design and analysis of solder connections using accelerated approximate procedure with disturbed state concept*", Ph.D dissertation, The University of Arizona, Tucson.

Whitenack, R.D., Desai C. S. and Rassaian M., (2007), "*Parametric and optimal design in electronic packaging using DSC: computational, geometrical and material aspects*", Journal of electronic packaging, 129, pp 356.

Wickham, S.S. and Johnson, W.H., 1981, "*The Tiskilwa Till: A regional view of its origin and depositional processes*", Annals of Glaciology, 2: 176-182.

Wiese, S., Schubert, A., Walter, H., Dudek, R., Feustel, F., Meusel E., Michel, B., 2001, "*Constitutive behavior of lead free vs lead containing solders - experiments on bulk specimens and flip chip joints*" , Electronic components and Technology conference proceedings, 29 May-1 June, pp:890 - 902

Wood, D.M., 1990, "*Soil Behaviour and Critical State Soil Mechanics*", Cambridge University Press, 462 pp.

Xiao, Q. and Armstrong, W.D., 2004, "*Tensile creep and microstructural characterization of bulk Sn3.9Ag0.6Cu Lead-free solder*", Journal of electronic materials, V34 - 2, pp196 - 211.

Zeng, Q., Wang Z., Xian A., and Shang J.K., 2005, "*Cyclic softening of the Sn3.8Ag0.7Cu Lead-free solder alloy with equiaxed grain structure*", Journal of electronic materials, V34 - 1, pp 62 - 67